**REPUBLIC OF TURKEY**
**YILDIZ TECHNICAL UNIVERSITY**
**GRADUATE SCHOOL OF NATURAL AND APPLIED SCIENCES**

# MODEL FOLLOWING METHODS IN FLIGHT CONTROL SYSTEMS

**Kadir TAMKAYA**

DOCTOR OF PHILOSOPHY THESIS
Department of Control and Automation Engineering
Control and Automation Engineering Program

Advisor
Assist. Prof. Dr. İlker ÜSTOĞLU

July, 2020

**REPUBLIC OF TURKEY**
**YILDIZ TECHNICAL UNIVERSITY**
**GRADUATE SCHOOL OF NATURAL AND APPLIED SCIENCES**

# MODEL FOLLOWING METHODS IN FLIGHT CONTROL SYSTEMS

A thesis submitted by Kadir TAMKAYA in partial fulfillment of the requirements for the degree of **DOCTOR OF PHILOSOPHY** is approved by the committee on 10.07.2020 in Department of Control and Automation Engineering, Control and Automation Engineering Program.

Assist. Prof. Dr. İlker ÜSTOĞLU
İstanbul Technical University
Advisor

**Approved By the Examining Committee**

Assist. Prof. Dr. İlker ÜSTOĞLU, Advisor
İstanbul Technical University _____

Assist. Prof. Dr. Levent UCUN, Member
Yildiz Technical University _____

Prof. Dr. Tankut ACARMAN, Member
Galatasaray University _____

Prof. Dr. Şeref Naci ENGİN, Member
Yildiz Technical University _____

Assoc. Prof. Dr. Tufan KUMBASAR, Member
İstanbul Technical University _____

I hereby declare that I have obtained the required legal permissions during data collection and exploitation procedures, that I have made the in-text citations and cited the references properly, that I haven't falsified and/or fabricated research data and results of the study and that I have abided by the principles of the scientific research and ethics during my Thesis Study under the title of Model Following Methods in Flight Control Systems supervised by my supervisor, Assist. Prof. Dr. İlker ÜSTOĞLU. In the case of a discovery of false statement, I am to acknowledge any legal consequence.

Kadir TAMKAYA

Signature

*Dedicated to my wife,*
*my children*
*and my parents*

# ACKNOWLEDGEMENTS

First and foremost, I would like to express my deepest gratitude to my advisor Assist. Prof. Dr. İlker ÜSTOĞLU for the continuous support of my Ph.D. study and research, for his patience, motivation, enthusiasm, and immense knowledge. I believe that I am tremendously fortunate to have worked with an outstanding scholar and an excellent person.

Besides my advisor, I would like to express my thanks to my Thesis Supervising Committee members, Assist. Prof. Dr. Levent UCUN and Prof. Dr. Tankut ACARMAN for their encouragement and insightful comments.

Most importantly, I wish to express my special gratitude to my loving and supportive wife, Sümeyye Elif TAMKAYA, and my wonderful son, Ömeralp TAMKAYA. They have always supported me with extraordinary patience by sacrificing the time we should spend together during my challenging Ph.D. education.

Last but not least, I would like to extend my special gratitude to my parents, Semih and Mürvet TAMKAYA, for their endless love, support, and trust. I would never have gotten to where I am today without their support, inspiration, and encouragement.

Kadir TAMKAYA

# TABLE OF CONTENTS

# LIST OF SYMBOLS

| | |
|---|---|
| $a$ | Acceleration |
| $C_{L_{\dot{\alpha}}}$ | Acceleration Derivative for Lift |
| $C_{M_{\dot{\alpha}}}$ | Acceleration Derivative for Moment |
| $a_B$ | Acceleration in Body-Fixed Frame |
| $\widetilde{X}_i, \widetilde{Y}_i, \widetilde{Z}_i,$ | |
| $\widetilde{L}_i, \widetilde{M}_i, \widetilde{N}_i$ | Aerodynamic Derivatives |
| $\delta_a$ | Aileron Deflection |
| $F_W$ | Air-Trajectory Reference Frame |
| $h$ | Aircraft Altitude |
| $l$ | Aircraft Length |
| $\lambda$ | Aircraft Offset Angle with respect to the Main Radial Line |
| $V_T$ | Aircraft True Velocity |
| $S$ | Aircraft Wing Reference Area |
| $b$ | Aircraft Wing Span |
| $\alpha$ | Angle of Attack |
| $H_B$ | Angular Momentum in Body-Fixed Frame |
| $\omega_B$ | Angular Velocity in Body-Fixed Frame |
| $\omega_V$ | Angular Velocity in Vehicle-Carried Frame |
| $F_B$ | Body-Fixed Reference Frame |
| $cg$ | Centre of Gravity |
| $C_D$ | Drag Coefficient |
| $D$ | Drag Force |
| $F_E$ | Earth-Fixed Reference Frame |

| | |
|---|---|
| $C_{M_{\delta_e}}$ | Elevator Control Power |
| $\delta_e$ | Elevator Deflection |
| $\gamma_a$ | Flight Path Angle |
| $f$ | Force |
| $f_B$ | Force in Body-Fixed Reference Frame |
| $g$ | Gravitational Acceleration |
| $x$ | Horizontal Distance |
| $W_x$ | Horizontal Induced Velocity |
| $I_B$ | Inertial Matrix in Body-Fixed Frame |
| $F_I$ | Inertial Reference Frame |
| $\widetilde{Y}$ | Lateral Force |
| $\widetilde{v}$ | Lateral Velocity Component in Body-Fixed Frame |
| $C_L$ | Lift Coefficient |
| $C_{L_O}$ | Lift Coefficient at Zero Angle of Attack |
| $L$ | Lift Force |
| $C_{L_\alpha}$ | Lift-Curve Slope |
| $V_\infty$ | Local Air Velocity |
| $\widetilde{X}$ | Longitudinal Force |
| $\widetilde{u}$ | Longitudinal Velocity Component in Body-Fixed Frame |
| $m$ | Mass |
| $\bar{\sigma}$ | Maximum Singular Value |
| $\bar{c}$ | Mean Aerodynamic Chord |
| $\underline{\sigma}$ | Minimum Singular Value |
| $G_B$ | Moment Acting on Aircraft in Body-Fixed Frame |
| $I_{xx}$ | Moment of Inertia on the x-axis |
| $I_{yy}$ | Moment of Inertia on the y-axis |
| $I_{zz}$ | Moment of Inertia on the z-axis |
| $C_{D_O}$ | Parasite Drag Coefficient |
| $\widetilde{X}_C, \widetilde{Y}_C, \widetilde{Z}_C,$ | |

| | |
|---|---|
| $\widetilde{L}_C, \widetilde{M}_C, \widetilde{N}_C$ | Pilot Controls |
| $\theta$ | Pitch Angle |
| $C_{M_q}$ | Pitch Damping Derivative |
| $q$ | Pitch Rate |
| $C_{M_\alpha}$ | Pitch Stiffness Derivative |
| $C_M$ | Pitching Coefficient |
| $\widetilde{M}$ | Pitching Moment |
| $C_{M_O}$ | Pitching Moment Coefficient at Zero Angle of Attack |
| $I_{xy}$ | Product of Inertia on the x-y axis |
| $I_{xz}$ | Product of Inertia on the x-z axis |
| $I_{yz}$ | Product of Inertia on the y-z axis |
| $\gamma_R$ | Reference Trajectory Path Angle |
| $\phi$ | Roll (Bank) Angle |
| $p$ | Roll Rate |
| $\widetilde{L}$ | Rolling Moment |
| $\widetilde{L}_{\delta_a}$ | Rolling Moment Derivative due to Aileron Deflection |
| $\widetilde{L}_p$ | Rolling Moment Derivative due to Roll Rate |
| $\widetilde{L}_{\delta_r}$ | Rolling Moment Derivative due to Rudder Deflection |
| $\widetilde{L}_\beta$ | Rolling Moment Derivative due to Sideslip |
| $\widetilde{L}_r$ | Rolling Moment Derivative due to Yaw Rate |
| $\delta_r$ | Rudder Deflection |
| $\widetilde{Y}_{\delta_a}$ | Side-force Derivative due to Aileron Deflection |
| $\widetilde{Y}_p$ | Side-force Derivative due to Roll Rate |
| $\widetilde{Y}_{\delta_r}$ | Side-force Derivative due to Rudder Deflection |
| $\widetilde{Y}_\beta$ | Side-force Derivative due to Sideslip |
| $\widetilde{Y}_r$ | Side-force Derivative due to Yaw Rate |
| $\beta$ | Sideslip Angle |
| $A_0$ | Static Thrust from Two Engines |
| $sup$ | Supremum |

| | |
|---|---|
| $\delta_t$ | Throttle Position |
| $T$ | Thrust Force |
| $A_1$ | Thrust for each $ft/s$ |
| $\tau$ | Time Constant |
| $L_{BV}$ | Transformation Matrix from Vehicle to Body-Fixed Coordinate System |
| $\sigma_v$ | Turbulence Intensity |
| $S_l$ | Turbulence Scale Length |
| $i_B$, $j_B$, $k_B$ | Unit Vectors in Body-Fixed Frame |
| $F_V$ | Vehicle-Carried Reference Frame |
| $\widetilde{Z}$ | Vertical Force |
| $W_h$ | Vertical Induced Velocity |
| $\widetilde{w}$ | Vertical Velocity Component in Body-Fixed Frame |
| $x_i$ | x-axis in the Reference Frame i |
| $y_i$ | y-axis in the Reference Frame i |
| $\psi$ | Yaw (Heading) Angle |
| $\psi_{ref}$ | Yaw (Heading) Angle of Beam |
| $r$ | Yaw Rate |
| $\widetilde{N}$ | Yawing Moment |
| $\widetilde{N}_{\delta_a}$ | Yawing Moment Derivative due to Aileron Deflection |
| $\widetilde{N}_p$ | Yawing Moment Derivative due to Roll Rate |
| $\widetilde{N}_{\delta_r}$ | Yawing Moment Derivative due to Rudder Deflection |
| $\widetilde{N}_\beta$ | Yawing Moment Derivative due to Sideslip |
| $\widetilde{N}_r$ | Yawing Moment Derivative due to Yaw Rate |
| $z_i$ | z-axis in the Reference Frame i |

# LIST OF ABBREVIATIONS

| | |
|---|---|
| ALS | Automatic Landing System |
| DME | Distance Measuring Equipment |
| GPS | Global Positioning System |
| ILS | Instrumental Landing System |
| LMI | Linear Matrix Inequality |
| LQR | Linear Quadratic Regulator |
| PD | Proportional–Derivative |
| PID | Proportional–Integral–Derivative |
| RVR | Runway Visual Range |
| UAV | Unmanned Aerial Vehicle |
| VOR | Very High-Frequency Omni-Directional Range |

# LIST OF FIGURES

# LIST OF TABLES

# ABSTRACT

## Model Following Methods in Flight Control Systems

Kadir TAMKAYA

Department of Control and Automation Engineering
Doctor of Philosophy Thesis

Advisor: Assist. Prof. Dr. İlker ÜSTOĞLU

Probably the most important part during a flight is the landing phase because most of the accidents occur in this phase. Automatic Landing System (ALS) takes over control during this phase to avoid potential pilot-induced risks. However, some external disturbances, such as the windshear and turbulence, can jeopardize the safe landing. In this study, the final approach phase and flare phase are handled differently. A combination of some useful design methods is brought together to improve the performance of the conventional ALS even under severe weather conditions. The model following method is merged with the $H_\infty$ synthesis method to find out the optimal solution for a given cost function. The resultant $H_\infty$ optimal control problem is solved using Linear Matrix Inequalities (LMIs), and then a dynamic controller is constructed. The overall system is transformed into a P-K configuration, which is a highly compact control system structure. Thus, any disturbance or uncertainties can be included in the system explicitly. While the model following method continuously corrects the error, the $H_\infty$ controller attenuates any disturbance in the system. In addition to that, the robustness takes a vital role in the flight systems and needs to be handled correctly. Therefore, the windshear and turbulence models are considered as the disturbance, and their effects are minimized, such a way that the tracking performance remains unaffected. Thus, highly significant results are obtained using the proposed method even under severe weather conditions.

**Keywords:** Aircraft landing, ALS, $H_\infty$ synthesis, model following control, linear matrix inequlity

**YILDIZ TECHNICAL UNIVERSITY**
**GRADUATE SCHOOL OF NATURAL AND APPLIED SCIENCES**

# ÖZET

## Uçuş Kontrol Sistemlerinde Model İzleme Yöntemleri

Kadir TAMKAYA

Kontrol ve Otomasyon Mühendisliği Anabilim Dalı
Doktora Tezi

Danışman: Dr. Öğr. Üyesi İlker ÜSTOĞLU

Hava taşıtlarının uçuşu esnasındaki geçtiği muhtemelen en önemli safha iniş aşamasıdır, çünkü kazaların çoğu bu aşamada meydana gelir. Otomatik iniş sistemleri (OİS), potansiyel pilot kaynaklı riskleri önlemek için bu aşamada uçuşun kontrolünü devralır. Ancak, ani rüzgar değişimleri ve türbülans gibi dış kaynaklı bozucular güvenli iniş için tehlike oluşturabilirler. Bu çalışmada uçuşun iniş safhasında yer alan son yaklaşma ve palye aşamaları ele alınmıştır. Geleneksel otomatik iniş sistemlerinin performansını ağır hava şartlarında dahi arttırmak için bazı faydalı tasarım yöntemleri bir araya getirilir. Belirli bir maliyet fonksiyonunda en uygun çözümü bulmak için $H_\infty$ kontrolcü tasarım yöntemi ile model izleme yönteminin birlikte kullanımından ortaya çıkan $H_\infty$ optimal kontrol problemi doğrusal matris eşitsizlikleri kullanılarak çözülerek dinamik bir kontrolcü oluşturulur. Öte yandan, tüm sistem P-K yapısı şeklinde oluşturularak bozucu ve gürültü ekleme ve çıkarma gibi daha sonra sistemde ihtiyaç duyulan değişiklikler kolayca yapılabilmektedir. Model izleme yöntemi hatayı devamlı olarak düzeltirken tasarlanan $H_\infty$ kontrolcü sistemdeki bozucuları bastırır. Buna ek olarak, dayanıklılık uçuş sistemlerinde çok önemli bir rol oynar ve doğru bir şekilde ele alınması gerekir. Bu nedenle çalışmamızda ani rüzgar değişimleri ve türbülanslar dikkatle ele alınarak uçağın tanımlanan modeli takip ederken ki performansına etkileri olabildiğince küçük tutulur. Böylece, önerilen yöntem sayesinde ağır hava şartlarında dahi dikkate değer sonuçlar elde edilmektedir.

**Anahtar Kelimeler:** Otomatik iniş sistemi, OİS, $H_\infty$ sentezi, model izleme yöntemi, doğrusal matris eşitsizlikleri

**YILDIZ TEKNİK ÜNİVERSİTESİ**
**FEN BİLİMLERİ ENSTİTÜSÜ**

# 1
# INTRODUCTION

## 1.1 Literature Review

An aircraft must be such controlled that its wheels touch the desired point on the runway smoothly. The landing procedure consists of five different phases [1]: alignment, glideslope, flare, touchdown, and taxiing. The aircraft must be aligned to the center of the runway before starting the glideslope phase. Then the aircraft starts descending at a constant speed and constant flight angle around $-2.5^\circ$ during the glideslope phase. When the altitude reaches around 50 *ft*, the flare phase is initiated, and the aircraft descends exponentially for a smooth touchdown. In the touchdown point, the descent rate goes down to -2 *ft/s*.

The pilot has to decide whether to land at some point during the landing maneuver. This point is called *decision-height*. The pilot checks all the necessary values related to the flight status at that point. The typical values at the decision-height point for the F-16 aircraft are given in Table 1.1 [2]. Figure 1.1 illustrates the landing maneuver. If the flight status values are beyond the typical values or there is no satisfactory visual clearance, the pilot is required to execute a missed approach and go around to re-attempt the landing or direct to another airport.

**Table 1.1** Typical set of values at decision-height point

| Decision-height point | $\simeq$ 10 *sec.* before touch-down |
|---|---|
| Angle of attack ($\alpha$) | $10-15^\circ$ |
| Vertical deviation | $\leq 5$ *ft* |
| Horizontal deviation | $\leq 15$ *ft* |
| Roll error angle ($\phi_e$) | $\leq 5^\circ$ |
| Pitch error angle ($\theta_e$) | $\leq 5^\circ$ |
| Yaw error angle ($\psi_e$) | $\leq 5^\circ$ |
| Sink Rate | 250-1000 *ft/min* |

Another critical definition for the landing is the *runway visual range (RVR)*, which is instrumentally derived value and located at the airports. RVR is a distance measure

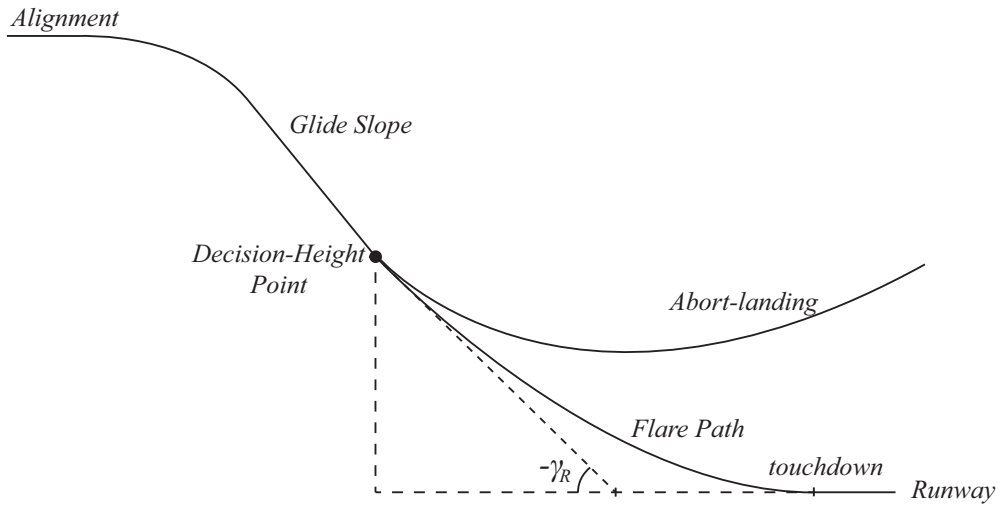


**Figure 1.1** Landing maneuver

in which the pilot can see the markings on the center-line of the runway. Thus, the RVR informs the pilot about the visibility. National licensing authorities specify the minimum values of both the decision-height and runway visual range, which differ according to the types of the aircraft and the airport [3].

Landings are separated into various categories according to the visibility conditions. Figure 1.2 represents these categories [4]. According to Figure 1.2, the autopilot systems for the general aviation aircraft that are decoupled at 60m are typically certified to Category I and II, and the landings are performed manually [5]. The commercial aircraft are typically certified to Category III, which is divided into three parts. Category IIIa allows the automatic landing during the flare phase, but the pilot takes over the control at the point of the touchdown. In addition to the automatic flare, roll-out is performed automatically for some distance along the runway in Category IIIb. Category IIIc is a fully automatic landing, which includes taxi-ing.

Most of the aircraft accidents occur during the landing maneuver due to pilotage errors, technical issues, or severe weather conditions. The landing maneuver is the most critical part of the flight. The accidents become more likely to happen as the aircraft approach the ground level because the disturbances and uncertainties, such as windshear, gust, and measurement noises, become more critical while the speed and altitude of the aircraft are decreasing during the landing [6]. At these low speed and low altitude, the pilots may become incapable of maintaining the control of the aircraft. According to the accident statistics, 45% of the accidents occur during the approach and landing phases of the flight, and over 90% of those accidents are pilot related [7, 8]. 520 of the 524 people were killed on the accident of Boeing 747 of Japan Airlines in 1985, and 110 of the 285 people were killed on the accident of DC-10 of United Airlines in 1989. There was only the thrust control unit left for the

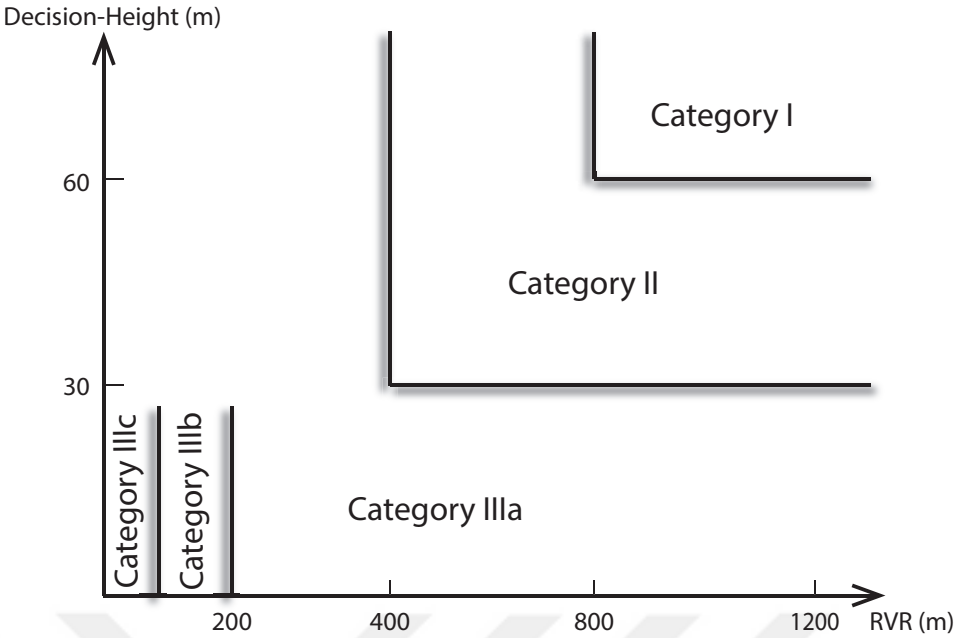


**Figure 1.2** Landing categories

pilots to land the aircraft, but they failed [9]. Another accident was on August 2, 1985, at Dallas/Fort Worth International Airport. Delta Airlines flight 191 crashed, and 137 people were killed, and 28 others were injured [10].

Researchers have developed the Automatic Landing System (ALS) to increase the safety and reliability of the flight, which was firstly developed by British Aerospace (BAE) in 1965 for the commercial aircraft [5]. It has become popular since then and is used in most of the aircraft today. ALS not only provides a comfortable, smooth, and safe landing, but it also avoids tire and landing gear wear. It is suitable for use in rainy and foggy weather conditions but deactivated in the strong winds; thus, the pilot handles the landing procedure manually. Another research was carried out on the automatic thrust control by NASA Dryden Flight Research Center (FRC).

The ALS works in harmony with the Instrumental Landing System (ILS) that is located at the airport [11]. The aircraft is guided by the ILS to prepare for the landing. The ILS consists of two different beam transmitters. One of them is for the glideslope, and the other one is for the localizer. The aircraft aligns and localizes itself to a suitable altitude level, and an approach angle owing to these transmitters and starts decreasing its altitude [12]. Another equipment is differential GPS, which is used with the ALS [13]. The microwave landing system (MLS) is also one of the instruments that facilitate the landing [14].

Classical control methods are generally preferred in the ALS because of their simplicity and reliability. However, these methods mostly do not satisfy the desired robustness

and performance requirements. The classical control yields the multiple feedback loops and requires to close the loops one by one. That brings some performance and optimization difficulties. On the other hand, in recent years, the difficulties in the implementation of the modern control systems have been reduced inversely to the significant developments in the hardware of the digital flight computers [15]. Therefore, the studies related to the modern control systems in the flight systems made this area mature. There are many different methodologies applied by researchers such as PID [16], $H_2$, $H_\infty$ and $H_2/H_\infty$ synthesis [6, 10, 17–23], fuzzy-logic [24–32], neural network [33–39], backstepping control[40–42], dynamic inversion [21, 43, 44], sliding mode control (SMC) [45–49], energy-based control [50, 51], quantitative feedback theory [52], feedback linearization technique [53], genetic algorithm [54, 55], vision-based navigation [1, 13, 56–60], etc. Some of these studies are discussed below.

Stevens and Lewis uses the model following method in their study [61]. They mathematically define an exponential decay function as a reference model for the flare phase of the landing system. The study aims to show how close the actual state of the aircraft tracks the reference model. Linear quadratic regulator (LQR) is chosen as a controller type. Although satisfactory results are obtained from this study, there is no consideration of any disturbance such as gust, windshear, measurement noise, etc.

Juang and Chio [25] studied on the implementation of the fuzzy controllers combined with a linearized inverse aircraft model on the automatic landing systems. In this study, the complete landing phase is divided into several stages, and the changes in the weight for the controller are computed at each state. Thus, a multilayered fuzzy neural network is used as the controller to provide the control signals at each stage of the landing phase. The combination of the fuzzy logic and neural network systems increases the adaptation of the flight controller to different environments. Even though the simulations results look decent under some turbulence conditions, calculating the controller coefficients each time when the weight changes brings workload and complicates the design.

Edward and Chang [32] worked on the unsteady aerodynamic effects in the landing maneuvers to show the capability of the fuzzy-logic dynamic inversion technique. According to this study, the disturbances and dynamic ground effects change the aerodynamics of the aircraft. These undesired conditions cause hard landings and rolling oscillations before the touchdown and runway veer-off event. Fuzzy logic aerodynamic models are used to show the local unstable roll damping and the loss of control due to varying crosswind. To avoid all these undesired conditions, the

fuzzy-logic model (FLM) dynamic inversion technique is employed. Considering the unsteady aerodynamic effect and adverse weather conditions are the advantages of this method.

Another approach to the automatic landing system is the sliding mode control (SMC) technique. Rao and Hiong [46] study on the sliding mode control technique to design a nonlinear aircraft controller by converting the landing maneuver into a trajectory tracking problem. They specify a reference trajectory to be tracked, which consists of a straight and exponential curved profile. A control law is derived by forcing the sliding function to reach a solution using the Lyapunov stability criteria. Linearization of the six degrees of freedom nonlinear aircraft model is not necessary to solve this problem owing to the usage of the SMC technique. However, the external disturbance and aerodynamic model uncertainties are ignored in this paper.

SMC was also used by Juang and Yu [47] by making use of the cerebellar model articulation controller (CMAC). This study focuses on the sliding mode control applications of the ALS and deals with the wind disturbances by taking advantage of the independence of the SMC from the parametric uncertainties and external disturbances. Genetic algorithm (GA), particle swarm optimization (PSO), and chaotic particle swarm optimization (CPSO) are used to adjust the parameters of the sliding mode control. The Lyapunov stability criteria are also used to derive the adaptive learning rules for the control system. The real-time performance of the controller is tested on a DSP board under different wind turbulence and windshear environment.

Recurrent neural networks (RNN) with the genetic algorithms (GA) were used by the researchers in [55] to improve the performance of the conventional automatic landing control systems. This study aims to investigate the neural network applications of the ALS by proposing a hybrid RNN-GA control scheme to guide an aircraft to a safe landing under turbulence conditions. Weights of the neural networks are updated by the RNN with the real-time recurrent learning techniques. The simulation results are compared to the conventional PID controller technique. According to the study, while the wind turbulence limit is 30 $ft/s$ for the PID system, the proposed method in this paper increases the limit up to 60 $ft/s$.

Another interesting approach to the ALS is to use a camera as a navigation sensor to detect and track some specific points in an image. Optical flow and 2-D image features from the image of a runway are used as feedback. The researchers in [1] develops a nonlinear image-based servo (IBSV) controller, which is divided into two components. The first component guarantees the horizontal alignment, and the second component takes advantage of the optical flow feedback to ensure a smooth touchdown in the

presence of a wind disturbance. The disturbance is assumed to be a constant wind, unlike a real wind representation such as turbulence or windshear.

Singh and Padhi [43] proposed a nonlinear control design approach by using the dynamic inversion along with the path planning for the automatic landing of the unmanned aerial vehicles (UAV). This technique relies on the feedback linearization, which cancels the nonlinearities in the plant. Thus, the closed-loop system behaves as a stable linear system. The advantage of this system is its simplicity and ease of implementation. However, the dynamic inversion technique requires precise knowledge of the nonlinear system dynamics to achieve a perfect cancellation. Thus, this precision is almost impossible due to the model simplifications, parametric uncertainties, etc. [62]. Some improvements in the robustness of the system may be needed to use this method.

The mixed $H_2/H_\infty$ control technique is another approach used for the automatic landing control systems. Shue and Agarwal [20] adapted this technique to control the landing maneuver of an aircraft. They used the $H_2$ method to obtain an optimal control gain for the trajectory optimization by minimizing the cost function, and $H_\infty$ to minimize the effect of disturbance inputs on the performance output. A convex theory algorithm was derived to obtain the mixed $H_2/H_\infty$ control gain to satisfy the robust and optimal requirement.

The mixed $H_2/H_\infty$ control technique was also used together with the dynamic inversion technique by adding an optimal observer, the geometry of the landing, and two reference models by Romulus and Mihai Lungu in [21]. The paper is also taking into consideration the sensor errors and other disturbances in the system. The control law is divided into two components. The first component is the guidance component, which is calculated by the dynamic inversion approach, and the other one is the optimal component designed by the Mixed $H_2/H_\infty$ control technique, which cancels the sensor errors and other disturbances in the system.

Xin and Shi [42] studied on a robust adaptive backstepping control method that was synthesized with the adaptive PID control for the glideslope and flare phases on the aircraft landing process. Antiwindup compensators for the saturation errors and virtual command filters for easy calculation of the virtual command derivatives were constructed during the implementation of the proposed method. In this paper, the researchers experimented with a constant and linear augmentation of the glideslope angle for a safe landing, and they came across that the aircraft can achieve short landing performance by properly increasing the glideslope angle. They also inserted a nonlinear disturbance observer in the closed-loop system to estimate and compensate

the compound uncertainties to ensure the robustness.

The backstepping control method was also used by the researchers in [40]. The paper suggests using the adaptive integrated guidance and control (IGC) logic with the adaptive output feedback inversion and backstepping techniques. The objective of this study is to compensate for the error between the relative state of the aircraft and the moving reference point on a landing trajectory regardless of its initial position. The position of a virtual moving reference point is calculated by the guidance command generator until the runway touchdown point. Thus the various landing patterns can be used without changing the IGC structure.

The conventional controller and fuzzy controller are compared by the researchers in [28]. The paper focuses on two automatic landing systems, which consist of a subsystem based on dynamic inversion theory to control the longitudinal velocity. The first ALS is the instrumental landing system (ILS); the second ALS is the altitude control using the state vector. The PD controller is used for the glideslope phase, and the PID controller is used for the flare phase. The classical and fuzzy-logic approaches are considered for both the controllers. According to the simulation results, the windshear insignificantly affects the transient regime of the two phases for both the first and second ALS's. The ALS, based on the dynamic inversion technique, has a better response than the ALS with the ILS and conventional controllers. However, if the fuzzy-logic controller is used instead of the conventional controller, much better performance is obtained. On the other hand, the sensor errors of the measurement system do not affect the two landing phases with this method.

To make a system robust in the presence of the parametric uncertainties, external disturbances, and input constraints is a highly desired goal for an automatic landing system. The researchers in [19] propose two different methods to achieve this goal. The first method uses an $H_\infty$ state feedback method to minimize the impact of the windshear effect and the pole placement technique to obtain satisfactory transient response under the input constraints. The Lyapunov approach is also used to design the corresponding controller. The second method is a robust pole placement technique subject to the Lyapunov based input constraints. Thus, the linear matrix inequalities (LMIs) are used to convert the multi-objective ALS problem into a convex optimization problem.

Akmeliawati and Mareels [50] studied on a nonlinear energy-based control method (NEM). The idea behind the NEM is to modify the energy of the system to achieve some specific control objectives such as automatic pitch stabilization and trajectory tracking for the landing phase. This study proposes to describe aircraft dynamics as

energy-functions. Thus the stabilization and tracking can be achieved by modifying these functions such that the operating points are at the lowest point of the energy function manifolds. Lyapunov functions are used when designing the controller. The gains of the control structure are tuned such that the closed-loop responses provide the design criteria. Monte Carlo simulations are conducted to test the disturbance rejection and robustness of the closed-loop system in this paper.

During a flight, the aircraft must cope with many natural disturbances and uncertainties such as wind gust, windshear, noise at low altitude due to the density of air, sensor noise, parametric uncertainties, and so on. Most of the papers mentioned above do not include analyses on the robustness and performance requirements in the presence of disturbances and uncertainties. Although a few of them take account of some of the disturbances and uncertainties in their analysis, it is hard and time-consuming to reconfigure the system for new conditions and calculate the controller again. On the other hand, none of those mentioned above papers use the model following method and P-K configuration principle as part of their solution in the studies. In addition to that, all of the papers are interested in the glideslope and flare phases. However, ALS can be extended to the final approach phase.

## 1.2 Objective of the Thesis

The objective of this thesis is to demonstrate an effective and safe landing procedure even under severe weather conditions while proposing a method that can quickly reconfigure the overall system for variable inputs such as disturbance, noise, and uncertainties. In this method, a reference model is defined for the flare and final approach phases, and it is intended that the aircraft follows this model as closely as possible. The model following method is preferred for tracking the state/s of the reference model. The entire system is converted into the generalized plant P matrix. Then the problem is transformed into an $H_\infty$ optimal control problem by partitioning the P matrix appropriately. For optimal performance, a dynamic controller K is constructed by solving the Linear Matrix Inequalities (LMIs) while minimizing the $\gamma$.

P-K configuration is feasible for rearranging the system without too much effort. There are mainly two kinds of disturbance considered throughout the thesis, which are windshear and turbulence. The proposed method is applied to the flare and final approach phases. The model following method works in harmony with the optimal $H_\infty$ controller to correct, and attenuate the errors. Thus, the simulation results demonstrate the effectiveness of the proposed method.

## 1.3 Hypothesis

It is common to define a mathematical model for the landing phase of the flight system. If the model following method is combined with the $H_\infty$ synthesis method to construct an optimal controller, and the overall system transformed into a P-K configuration before finding the LMI solution, the aircraft has a smoother and safer landing even under external disturbances and the system can be reconfigured easily against structural, and external changes.

# 2
# AIRCRAFT MODELLING

## 2.1 Reference Frames

### 2.1.1 Inertial Reference Frame ($F_I$)

The inertial reference frame is a fixed frame with respect to the distant stars [63]. According to Newton's second low, $f = ma$ is valid if the reference frame is not rotating or accelerating. The reference frame here is the inertial reference frame, and "$a$" is the acceleration of a particle with respect to this frame.

### 2.1.2 Body-Fixed Reference Frame ($F_B$)

In the body-fixed reference frame, the axes on *cg* are fixed to the rigid body; thus, they move and rotate with the aircraft. The orientation of the body-fixed frame relative to the rigid body is selected such that all the products of inertia, $I_{xy}, I_{xz}, I_{yz}$, become zero. [64]. That is possible by choosing a plane that makes both sides of the aircraft symmetrical along the z-axis. Then, the center of the body-fixed axes is placed over the center of gravity point (*cg*) of the aircraft. The symmetrical plane passes through the center of gravity of the aircraft. Figure 2.1 illustrates the body-fixed reference frame. $x_B$ points towards the nose of the aircraft, $y_B$ points towards the starboard, and $z_B$ points towards downwards. $z_B$ is also the symmetry axis of the aircraft. Subscript $B$ represents the body-fixed reference frame.

### 2.1.3 Vehicle-Carried Reference Frame ($F_V$)

In the vehicle-carried reference frame, the origin is fixed to the center of the gravity point of the aircraft as the body-fixed reference frame. However, the axes change relative to the rigid body when aircraft moves and rotates. $x_V$ points towards the north, $y_V$ points towards the east, and $z_V$ points toward the gravity vector. If the aircraft rotates, $x_V$, $y_V$, and $z_V$ still point toward the north, east, and the gravity vector, respectively.

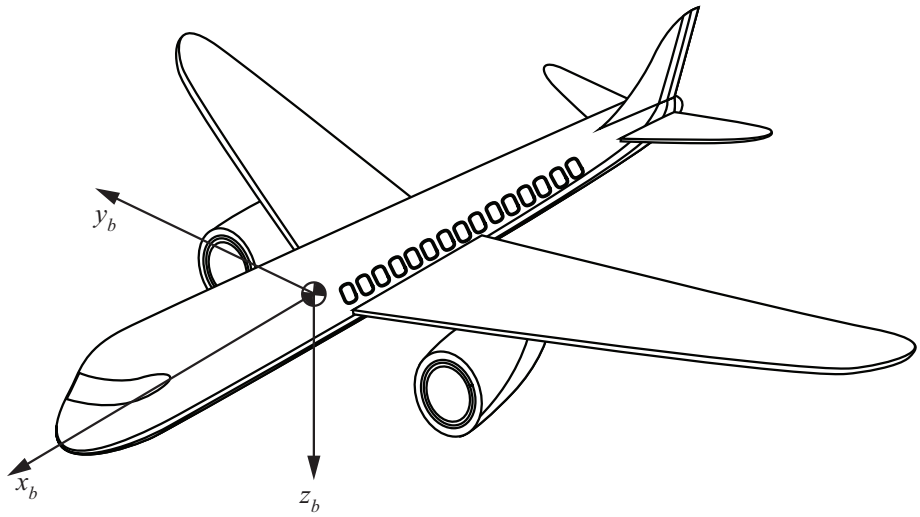


**Figure 2.1** Coordinate orientation of body-fixed reference frame

### 2.1.4 Earth-Fixed Reference Frame ($F_E$)

The earth-fixed reference frame is used as the inertial reference frame for most of the cases. Any point, preferably close point where the aircraft is analyzed, can be chosen on the Earth and placed the origin of the earth-fixed coordinate axes over. $x_E$ points towards the north, $y_E$ points towards the east, and $z_E$ points toward the gravity vector, which is the center of the Earth. The vehicle-carried and Earth-fixed coordinate systems are parallel if the Earth is assumed flat.

### 2.1.5 Air-Trajectory Reference Frame ($F_W$)

The Air-Trajectory Reference Frame is also called the Wind-Fixed Coordinate System, which is illustrated in Figure 2.2. The center of the coordinate axes is placed over the *cg* point of the aircraft. $x_w$ points toward the local air velocity vector $\vec{V}_\infty$, which has the same magnitude but opposite direction with the aircraft velocity vector $\vec{V}_T$. $y_w$ forms a right-handed coordinate system and $z_w$ points toward the symmetry plane of the aircraft.

## 2.2 The Forces and Moments on Aircraft

All the forces and moments written in the body-fixed reference frame are illustrated in Figure 2.3. The notations used for the forces and moments are also given in Table 2.1. $X$, $Y$, and $Z$ are also called "Aero-Propulsive Forces" because they include the lift, drag ("Aero" part), and thrust ("propulsive" part). The lift and drag are a function of other variables such as the angle of attack, side-slip, velocity, etc. The rotations and directions given in Figure 2.3 are positive and come from the right-hand rule.

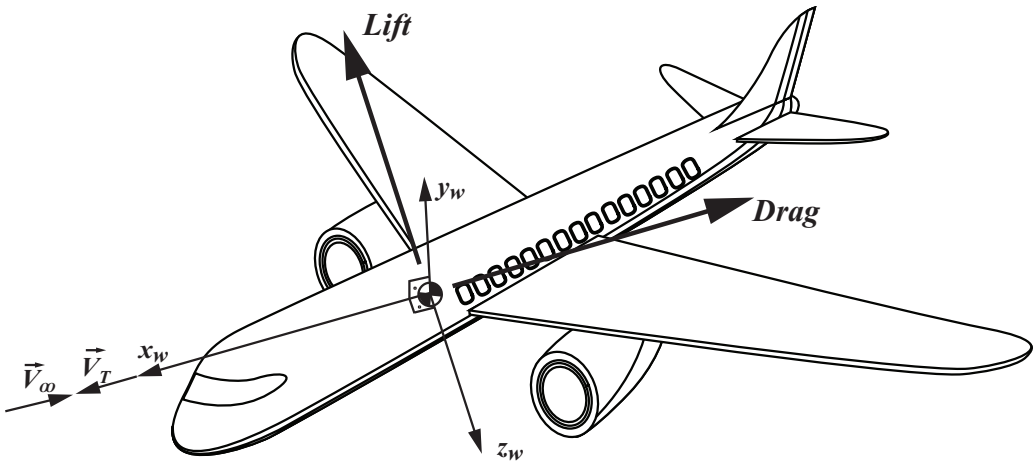


**Figure 2.2** Coordinate orientation of air-trajectory reference frame

The forces and moments can be described in the vector form written in the body-fixed reference frame as follows:

$$\vec{f}_b = \begin{bmatrix} \widetilde{X} \\ \widetilde{Y} \\ \widetilde{Z} \end{bmatrix} \qquad \vec{G}_b = \begin{bmatrix} \widetilde{L} \\ \widetilde{M} \\ \widetilde{N} \end{bmatrix} \tag{2.1}$$

**Table 2.1** Notations for forces and moments

| Notation | Description |
|---|---|
| $\widetilde{X}$ | Longitudinal Force |
| $\widetilde{Y}$ | Lateral Force |
| $\widetilde{Z}$ | Vertical Force |
| $\widetilde{L}$ | Rolling Moment |
| $\widetilde{M}$ | Pitching Moment |
| $\widetilde{N}$ | Yawing Moment |

## 2.3 Aircraft Angles and Rates

### 2.3.1 The Euler Angles and Angular Rates

$\phi$, $\theta$ and $\psi$, which are written in the body-fixed reference frame and shown in Figure 2.3, are called the Euler angles that help to describe the angular position of an aircraft in the space with respect to the vehicle-carried reference frame. In other words, the Euler angles define the rotation from the vehicle-carried reference frame to mostly either the body-fixed reference frame or air-trajectory reference frame.

$p$, $q$, and $r$ are the angular rates shown in Figure 2.3. All the angles and rates are described in Table 2.2.

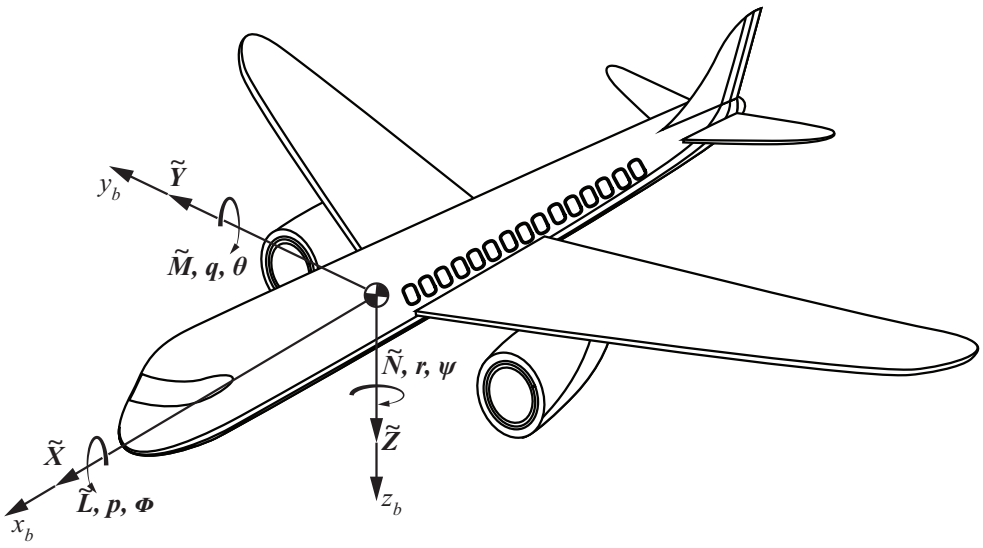


**Figure 2.3** Forces and moments acting on the aircraft

**Table 2.2** Notations for angles and rates

| Notation | Description |
|---|---|
| $\phi$ | Roll Angle |
| $\theta$ | Pitch Angle |
| $\psi$ | Yaw Angle |
| $p$ | Roll Rate |
| $q$ | Pitch Rate |
| $r$ | Yaw Rate |

### 2.3.2 The Aerodynamic Angles

The relationship between the true velocity and aerodynamic angles ($\alpha$ and $\beta$) written in the body-fixed reference frame is shown in Figure 2.4. The true velocity can be expressed using its components $\widetilde{u}$, $\widetilde{v}$ and $\widetilde{w}$ as given by

$$\vec{V_T} = \begin{bmatrix} \widetilde{u} \\ \widetilde{v} \\ \widetilde{w} \end{bmatrix} \tag{2.2}$$

These velocity components can be written using the aerodynamic angles as follows:

$$\widetilde{u} = V_T \cos\beta \cos\alpha \tag{2.3}$$

$$\widetilde{v} = V_T \sin\beta \tag{2.4}$$

$$\widetilde{w} = V_T \cos\beta \sin\alpha \tag{2.5}$$

The angle of attack and sideslip angle can be expressed as

$$\alpha = \arctan \frac{\widetilde{w}}{\widetilde{u}} \tag{2.6}$$

$$\beta = \arcsin \frac{\widetilde{v}}{V_T} \tag{2.7}$$

Note that the aerodynamic angles strictly related to the local air velocity vector $V_\infty$.

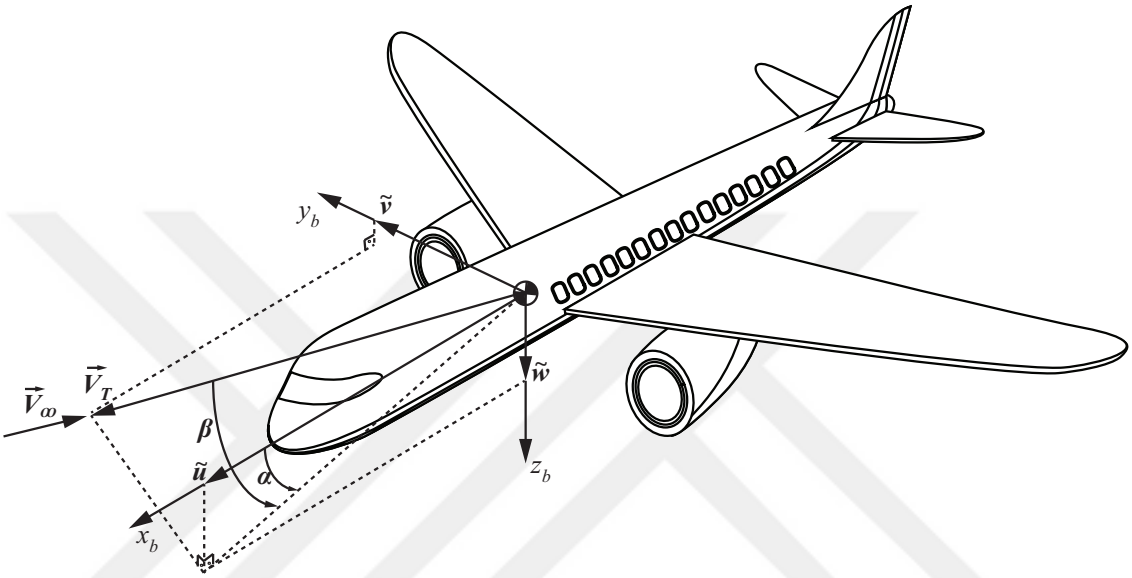


**Figure 2.4** Aerodynamic angles

## 2.4 Vector Transformation

A vector described in one of the reference frames as in Figure 2.5 frequently needs to be transformed into another reference frame, because the orientation of the fuselage during a flight often changes. For example, a coordinate system, usually the Earth-fixed reference frame, is chosen as a reference frame, and a vector described in this reference frame is transformed into the body-fixed reference frame. This transformation is done by rotating the reference coordinate system one-by-one around each axis.

Let us take a vector $\vec{V}$ in the vehicle coordinate system and transform it into the body-fixed coordinate system. The vector is given by

$$\vec{V} = \begin{bmatrix} V_x \\ V_y \\ V_z \end{bmatrix} \tag{2.8}$$

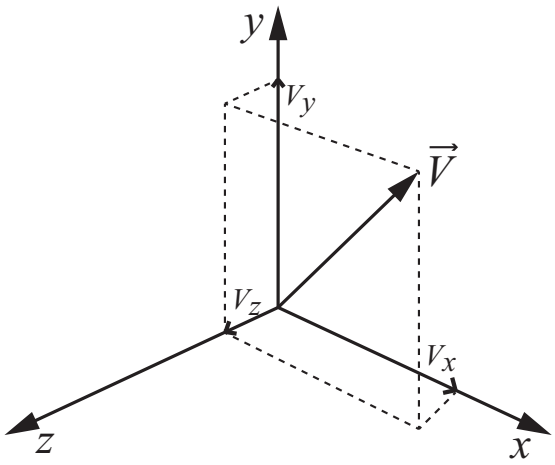


**Figure 2.5** A vector representation in a coordinate system

The sequence of rotation can be in any order, but in flight mechanics, the sequence is chosen as to be $\psi$, $\theta$, and $\phi$, respectively. In other words, the reference coordinate system is rotated around its $z$-axis by $\psi$, then around its $y$-axis by $\theta$ and finally around its $z$-axis by $\phi$.

If the reference coordinate system is rotated around the $z$-axis by $\psi$, the vector $\vec{V}$ can be rewritten as follows:

$$\begin{bmatrix} V_{x_1} \\ V_{y_1} \\ V_{z_1} \end{bmatrix} = \begin{bmatrix} \cos\psi & \sin\psi & 0 \\ -\sin\psi & \cos\psi & 0 \\ 0 & 0 & 1 \end{bmatrix} \begin{bmatrix} V_x \\ V_y \\ V_z \end{bmatrix} = T_1(\psi) \begin{bmatrix} V_x \\ V_y \\ V_z \end{bmatrix} \tag{2.9}$$

Now, the new coordinate system is rotated around $y_1$-axis by $\theta$.

$$\begin{bmatrix} V_{x_2} \\ V_{y_2} \\ V_{z_2} \end{bmatrix} = \begin{bmatrix} \cos\theta & 0 & -\sin\theta \\ 0 & 1 & 0 \\ \sin\theta & 0 & \cos\theta \end{bmatrix} \begin{bmatrix} V_{x_1} \\ V_{y_1} \\ V_{z_1} \end{bmatrix} = T_2(\theta) \begin{bmatrix} V_{x_1} \\ V_{y_1} \\ V_{z_1} \end{bmatrix} \tag{2.10}$$

Finally, the last coordinate system is rotated around $x_2$-axis by $\phi$.

$$\begin{bmatrix} V_{x_3} \\ V_{y_3} \\ V_{z_3} \end{bmatrix} = \begin{bmatrix} 1 & 0 & 0 \\ 0 & \cos\phi & \sin\phi \\ 0 & -\sin\phi & \cos\phi \end{bmatrix} \begin{bmatrix} V_{x_1} \\ V_{y_1} \\ V_{z_1} \end{bmatrix} = T_3(\phi) \begin{bmatrix} V_{x_2} \\ V_{y_2} \\ V_{z_2} \end{bmatrix} \tag{2.11}$$

Therefore, the vector $\vec{V}$ in Equation (2.8) in the vehicle coordinate system can be rewritten in the body-fixed coordinate system as follows:

$$\begin{bmatrix} V_{x_3} \\ V_{y_3} \\ V_{z_3} \end{bmatrix} = T_3(\phi)T_2(\theta)T_1(\psi) \begin{bmatrix} V_x \\ V_y \\ V_z \end{bmatrix} = T_{BV} \begin{bmatrix} V_x \\ V_y \\ V_z \end{bmatrix} \tag{2.12}$$

where

$$T_{BV} = \begin{bmatrix} \cos\theta\cos\psi & \cos\theta\sin\psi & -\sin\theta \\ \sin\phi\sin\theta\cos\psi - \cos\phi\sin\psi & \sin\phi\sin\theta\sin\psi + \cos\phi\cos\psi & \sin\phi\cos\theta \\ \cos\phi\sin\theta\cos\psi + \sin\phi\sin\psi & \cos\phi\sin\theta\sin\psi - \cos\phi\cos\psi & \cos\phi\cos\theta \end{bmatrix} \tag{2.13}$$

## 2.5 Angular Velocity

The vehicle-carried coordinate frame ($F_v$) is a fixed coordinate frame and does not rotate when the aircraft is rotating. Then, the orientation of the body-fixed coordinate frame ($F_B$) or air-trajectory reference frame ($F_W$) are given relative to the vehicle-carried coordinate frame by the Euler angles $\psi, \theta$, and $\phi$. Thus, the angular rates $p, q, r$ are not equal to the time derivative of the Euler angles.

$$\begin{bmatrix} p \\ q \\ r \end{bmatrix} \neq \begin{bmatrix} \dot{\phi} \\ \dot{\theta} \\ \dot{\psi} \end{bmatrix} \tag{2.14}$$

If $i, j, k$ represent unit vector and the subscripts $1, 2, 3$ denoting the direction of the axes, the angular velocity in frame $F_V$ is

$$\vec{\omega_V} = \vec{i_3}\dot{\phi} + \vec{j_2}\dot{\theta} + \vec{k_1}\dot{\psi} \tag{2.15}$$

The angular velocity can be written in the body-fixed coordinate frame as follows:

$$\vec{\omega_B} = p\vec{i_B} + q\vec{j_B} + r\vec{k_B} \tag{2.16}$$

where $i_B, j_B, k_B$ are the unit vectors on the body-fixed coordinate system. The procedure described in Section 2.4 is used to represent the orientation of an aircraft in the body-fixed reference frame. First, $k_1$ is rotated around the z-axis. However, it

is not necessary in this case, because if $k_1$ is rotated around the z-axis by $\psi$ in the vehicle-carried coordinate system, $k_1$ still stays in the same direction. Thus, $k_B$ can be written as below:

$$\vec{k_B} = T_{BV}\vec{k_1} = T_3(\phi)T_2(\theta)\vec{k_1} = T_{BV}\begin{bmatrix}0\\0\\1\end{bmatrix} \tag{2.17}$$

$$\vec{k_B} = -\sin\theta\vec{i_B} + \sin\phi\cos\theta\vec{j_B} + \cos\phi\cos\theta\vec{k_B} \tag{2.18}$$

The rotation around the z-axis by $\psi$ in the vehicle-carried coordinate system was executed when finding $\vec{k_B}$. Now, it is going to be rotated around the y-axis by $\theta$. However, it is not necessary in this case, because $j_2$ still stays in the same direction after the rotation. Thus, $j_B$ can be expressed as

$$\vec{j_B} = T_3(\phi)\vec{j_1} = T_3(\phi)\begin{bmatrix}0\\1\\0\end{bmatrix} \tag{2.19}$$

$$\vec{j_B} = \cos\phi\vec{j_B} - \sin\phi\vec{k_B} \tag{2.20}$$

The last rotation will be on the x-axis by $\phi$. However, it will stay on the x-axis after rotation.

$$\vec{i_B} = \vec{i_3} \tag{2.21}$$

Now, $\omega_B$ can be written as follows:

$$\vec{\omega_B} = (\dot{\phi} - \dot{\psi}\sin\theta)\vec{i_B} + (\dot{\theta}\cos\phi + \dot{\psi}\sin\phi\cos\theta)\vec{j_B} + (-\dot{\theta}\sin\phi + \dot{\psi}\cos\phi\cos\theta)\vec{k_B} \tag{2.22}$$

$$\begin{aligned} p &= \dot{\phi} - \dot{\psi}\sin\theta \\ q &= \dot{\theta}\cos\phi + \dot{\psi}\sin\phi\cos\theta \\ r &= -\dot{\theta}\sin\phi + \dot{\psi}\cos\phi\cos\theta \end{aligned} \tag{2.23}$$

Thus, the relationship between the angular rates and time derivative of the Euler angles can be written as follows:

$$\begin{bmatrix} p \\ q \\ r \end{bmatrix} = \begin{bmatrix} 1 & 0 & -\sin\theta \\ 0 & \cos\phi & \sin\phi\cos\theta \\ 0 & \sin\phi & \cos\phi\cos\theta \end{bmatrix} \begin{bmatrix} \dot{\phi} \\ \dot{\theta} \\ \dot{\psi} \end{bmatrix} = R(\theta,\phi) \begin{bmatrix} \dot{\phi} \\ \dot{\theta} \\ \dot{\psi} \end{bmatrix} \tag{2.24}$$

$$\begin{bmatrix} \dot{\phi} \\ \dot{\theta} \\ \dot{\psi} \end{bmatrix} = \begin{bmatrix} 1 & \sin\phi\tan\theta & cos\phi\tan\theta \\ 0 & \cos\phi & -\sin\phi \\ 0 & \sin\phi\sec\theta & \cos\phi\sin\theta \end{bmatrix} \begin{bmatrix} p \\ q \\ r \end{bmatrix} = R^{-1}(\theta,\phi) \begin{bmatrix} p \\ q \\ r \end{bmatrix} \tag{2.25}$$

## 2.6 Aircraft Equation of Motion

### 2.6.1 Translational Dynamics

The movement of *cg* point through $x$, $y$ and $z$ directions are given by

$$\sum \vec{f}_B = m.\vec{a}_B \tag{2.26}$$

where

$$\vec{f}_B = \begin{bmatrix} \widetilde{X} \\ \widetilde{Y} \\ \widetilde{Z} \end{bmatrix} + T_{BV} \begin{bmatrix} 0 \\ 0 \\ mg \end{bmatrix} \tag{2.27}$$

According to Coriolis Theorem,

$$\vec{a}_B = \frac{d\vec{V}_B}{dt} = \dot{\vec{V}}_B + \vec{\omega}_B x \vec{V}_B = \begin{bmatrix} \dot{\widetilde{u}} \\ \dot{\widetilde{v}} \\ \dot{\widetilde{w}} \end{bmatrix} + \begin{bmatrix} p \\ q \\ r \end{bmatrix} x \begin{bmatrix} \widetilde{u} \\ \widetilde{v} \\ \widetilde{w} \end{bmatrix} \tag{2.28}$$

Thus, Equation (2.26) can be written as follows:

$$\begin{bmatrix} \widetilde{X} \\ \widetilde{Y} \\ \widetilde{Z} \end{bmatrix} + T_{BV} \begin{bmatrix} 0 \\ 0 \\ mg \end{bmatrix} = m \left[ \begin{bmatrix} \dot{\widetilde{u}} \\ \dot{\widetilde{v}} \\ \dot{\widetilde{w}} \end{bmatrix} + \begin{bmatrix} p \\ q \\ r \end{bmatrix} x \begin{bmatrix} \widetilde{u} \\ \widetilde{v} \\ \widetilde{w} \end{bmatrix} \right] \tag{2.29}$$

The rigid body equations are

$$\begin{aligned}
\dot{\widetilde{u}} &= r\widetilde{v} - q\widetilde{w} + \frac{\widetilde{X}}{m} - g\sin\theta \\
\dot{\widetilde{v}} &= p\widetilde{w} - r\widetilde{u} + \frac{\widetilde{Y}}{m} + g\cos\theta\sin\phi \\
\dot{\widetilde{w}} &= q\widetilde{u} - p\widetilde{v} + \frac{\widetilde{Z}}{m} + g\cos\theta\cos\phi
\end{aligned} \tag{2.30}$$

$\widetilde{u}, \widetilde{v}, \widetilde{w}$ = velocity components on x,y,z coordinates

$p, q, r$ = angular velocity components on x,y,z coordinates

$\widetilde{X}, \widetilde{Y}, \widetilde{Z}$ = aero-propulsive forces

$\theta, \phi$ = Euler angles

### 2.6.2 Rotational Dynamics

Total moment, which is written in the body-fixed coordinate system but respect to an observer in the inertial frame, can be expressed as

$$\sum \vec{G}_B = \left.\frac{d\vec{H}_B}{dt}\right|_I \tag{2.31}$$

where $\vec{G}_B$ is the total external moment acting on the aircraft written in the body-fixed coordinate system and can be written as

$$\vec{G}_B = \begin{bmatrix} \widetilde{L} \\ \widetilde{M} \\ \widetilde{N} \end{bmatrix} \tag{2.32}$$

$\vec{H}_B$ is the angular momentum written in the body-fixed coordinate system and can be written as follows:

$$\vec{H}_B = I_B.\vec{\omega}_B^I \tag{2.33}$$

where $\vec{\omega}_B^I$ is the angular velocity of the aircraft written in the body-fixed coordinate system but respect to the observer in the inertial space. $\vec{\omega}_B^I$ can be expressed as

$$\vec{\omega}_B^I = \begin{bmatrix} p \\ q \\ r \end{bmatrix} \tag{2.34}$$

$I_B$ is the inertia matrix and can be written as follows:

$$I_B = \begin{bmatrix} I_{xx} & -I_{xy} & -I_{xz} \\ -I_{xy} & I_{yy} & -I_{yz} \\ -I_{xz} & -I_{yz} & I_{zz} \end{bmatrix} \tag{2.35}$$

where $I_{xx}$, $I_{yy}$ and $I_{zz}$ are called as "Moments of Inertia"; and $I_{xy}$, $I_{xz}$ and $I_{yz}$ are called as "Products of Inertia".

The moment of inertia gives us a piece of information about the difficulty of rotating the aircraft around its axes. In other words, $I_{xx}$ is a measure of how hard it is to rotate the aircraft around the $x$-axis, $I_{yy}$ is a measure of how hard it is to rotate the aircraft around the $y$-axis, and $I_{zz}$ is a measure of how hard it is to rotate the aircraft around the $z$-axis. The moment of inertia is directly proportional to the weight and size of the aircraft.

The product of inertia gives us a piece of information about how the mass is distributed. In other words, $I_{xy}$, $I_{xz}$, and $I_{yz}$ give us information about the symmetry. In symmetric aircraft, $I_{xy} = I_{yz} = 0$ and $I_{xz} \simeq 0$. For most of the aircraft, $I_{xz}$ is nonzero because of the asymmetry, but it can be taken as zero for simplicity because it has mostly a small value.

In Equation (2.31), it is taken the derivative of a vector ($\vec{H}_B$), which is written in the rotating body-fixed coordinate system. However, the change we are looking at is with respect to the fixed coordinate system, which is the inertial coordinate system. So, Coriolis Theorem is written as

$$\left.\frac{d\vec{H}_B}{dt}\right|_I = \dot{\vec{H}}_B + \vec{\omega}_B x \vec{H}_B \tag{2.36}$$

where

$$\vec{H}_B = \dot{I}_B.\vec{\omega}_B + I_B.\vec{\omega}_B \tag{2.37}$$

The change of the inertia matrix is negligible and its derivative can be taken as zero. So, Equation (2.37) can be simplified as

$$\vec{H}_B = I_B.\vec{\omega}_B \tag{2.38}$$

Thus, Equation (2.31) can be rewritten as follow:

$$\begin{bmatrix} \widetilde{L} \\ \widetilde{M} \\ \widetilde{N} \end{bmatrix} = I_B . \begin{bmatrix} \dot{p} \\ \dot{q} \\ \dot{r} \end{bmatrix} + \begin{bmatrix} p \\ q \\ r \end{bmatrix} \times \begin{bmatrix} I_B . \begin{bmatrix} p \\ q \\ r \end{bmatrix} \end{bmatrix} \tag{2.39}$$

$$\begin{aligned} \widetilde{L} &= I_{xx}.\dot{p} - I_{xz}(\dot{r} + p.q) - (I_{yy} - I_{zz})q.r - I_{yz}(q^2 - r^2) - I_{xy}(\dot{q} - r.p) \\ \widetilde{M} &= I_{yy}.\dot{q} - I_{xz}(r^2 - p^2) - (I_{zz} - I_{xx})r.p - I_{xy}(\dot{p} + q.r) - I_{yz}(\dot{r} - p.q) \\ \widetilde{N} &= I_{zz}.\dot{r} - I_{xz}(\dot{p} - q.r) - (I_{xx} - I_{yy})p.q - I_{xy}(p^2 - q^2) - I_{yz}(\dot{q} + r.p) \end{aligned} \tag{2.40}$$

If it is assumed that $I_{xy} = I_{yz} = I_{xz} = 0$ for simplification, then the rotational dynamic equations can be expressed as

$$\begin{aligned} \dot{p} &= \frac{\widetilde{L}}{I_{xx}} + (I_{yy} - I_{zz})\frac{q.r}{I_{xx}} \\ \dot{q} &= \frac{\widetilde{M}}{I_{yy}} + (I_{zz} - I_{xx})\frac{r.p}{I_{yy}} \\ \dot{r} &= \frac{\widetilde{N}}{I_{zz}} + (I_{xx} - I_{yy})\frac{p.q}{I_{zz}} \end{aligned} \tag{2.41}$$

Note that the translational dynamic equations given in (2.30) need $p, q$, and $r$ to be solved, and they are coming from the rotational dynamic equations given in (2.41). So, the translational and rotational dynamic equations can not be solved independently. That is the reason they are called "6 Degree of Freedom Rigid Body Equations". These are also called "Newton - Euler Dynamic Equations".

## 2.7 Trim Point of an Aircraft

A trim point of an aircraft is the state where all the resultant forces and moments are equal to zero. It is also called "Equilibrium Point". A trim point of an aircraft is the steady level flight condition. If all the forces and moments are zero, the accelerations become zero, and the velocities become constant. Therefore, in steady level flight, the states becomes

$$\begin{aligned} &\dot{p} = \dot{q} = \dot{r} = \dot{\widetilde{u}} = \dot{\widetilde{v}} = \dot{\widetilde{w}} = 0 \\ &p = q = r = 0 \\ &\phi = 0, \quad \theta = \theta_0 \\ &\widetilde{u} = 0, \quad \widetilde{v} = 0, \quad \widetilde{w} = \widetilde{w}_0 \end{aligned} \tag{2.42}$$

Therefore, in the steady level flight condition, the forces and moments in Equation (2.30) becomes as follows:

$$\begin{aligned}
\widetilde{X}_0 &= mg\sin\theta_0 \\
\widetilde{Y}_0 &= 0 \\
\widetilde{Z}_0 &= -mg\cos\theta_0 \\
\widetilde{L}_0 &= \widetilde{M}_0 = \widetilde{N}_0 = 0
\end{aligned} \tag{2.43}$$

## 2.8 Linearization around Equilibrium Point

Linearization of an equation around an equilibrium point also means writing down a perturbation equation. According to the small perturbation theory, every variable in the equation is a perturbation or disturbance from the equilibrium point. If the perturbations go back to zero, that means there is no perturbation around the equilibrium point; therefore, everything is back to its trim point. The idea is to check the stability of the perturbations to see if they are going back to zero. If they are, then it is in trim.

The linearization process is shown for one of the translational dynamics as follows:

$$\dot{\widetilde{u}} = r\widetilde{v} - q\widetilde{w} + \frac{\widetilde{X}}{m} - g\sin\theta$$

The variables are perturbed as

$$\begin{aligned}
\Delta\widetilde{u} = \widetilde{u} - \widetilde{u}_0 \quad &\Rightarrow \quad \Delta\dot{\widetilde{u}} = \dot{\widetilde{u}} \\
\Delta r = r - r_0 \quad &\Rightarrow \quad r = \Delta r + r_0 \\
\Delta\widetilde{v} = \widetilde{v} - \widetilde{v}_0 \quad &\Rightarrow \quad v = \Delta\widetilde{v} + \widetilde{v}_0 \\
\Delta q = q - q_0 \quad &\Rightarrow \quad q = \Delta q + q_0 \\
\Delta\widetilde{w} = \widetilde{w} - \widetilde{w}_0 \quad &\Rightarrow \quad \widetilde{w} = \Delta\widetilde{w} + \widetilde{w}_0 \\
\Delta\widetilde{X} = \widetilde{X} - \widetilde{X}_0 \quad &\Rightarrow \quad \widetilde{X} = \Delta\widetilde{X} + \widetilde{X}_0 \\
\Delta\theta = \theta - \theta_0 \quad &\Rightarrow \quad \theta = \Delta\theta + \theta_0
\end{aligned}$$

Then we obtain

$$\Delta\dot{\widetilde{u}} = (\Delta r + r_0)(\Delta\widetilde{v} + \widetilde{v}_0) - (\Delta q + q_0)(\Delta\widetilde{w} + \widetilde{w}_0) + \frac{(\Delta\widetilde{X} + \widetilde{X}_0)}{m} - g\sin(\Delta\theta + \theta_0)$$

In trim level, $r_0 = \widetilde{v}_0 = q_0 = 0$, and the angle of attack in steady level flight is small, $\widetilde{w}_0 \simeq 0$. Therefore

$$\Delta\dot{\widetilde{u}} = \Delta r\Delta\widetilde{v} - \Delta q\Delta\widetilde{w} + \frac{(\Delta\widetilde{X} + mg\sin\theta_0)}{m} - g\sin(\Delta\theta + \theta_0)$$

Taylor series of $\sin(\theta_0 + \Delta\theta)$ can be written as

$$\sin(\theta_0 + \Delta\theta) = \sin\theta_0 + \Delta\theta\cos(\theta_0)$$

Then the equation becomes as follows:

$$\Delta\dot{\widetilde{u}} = \frac{\Delta\widetilde{X}}{m} - g\Delta\theta\cos(\theta_0)$$

If same procedure is applied for all the translational and rotational dynamics, we get the linearized translational and rotational dynamics as follows:

$$\begin{aligned}
\Delta\dot{\widetilde{u}} &= \frac{\Delta\widetilde{X}}{m} - g\Delta\theta\cos(\theta_0) \\
\Delta\dot{\widetilde{v}} &= \frac{\Delta\widetilde{Y}}{m} - g\phi\cos(\theta_0) - \widetilde{u}_0 r \\
\Delta\dot{\widetilde{w}} &= \frac{\Delta\widetilde{Z}}{m} - g\Delta\theta\sin(\theta_0) + \widetilde{u}_0 q
\end{aligned} \tag{2.44}$$

$$\begin{aligned}
\dot{p} &= (I_x I_z - I_{xz}^2)^{-1}(I_z\Delta\widetilde{L} + I_{xz}\Delta\widetilde{N}) \\
\dot{q} &= \frac{\Delta\widetilde{M}}{I_y} \\
\dot{r} &= (I_x I_z - I_{zx}^2)^{-1}(I_{zx}\Delta\widetilde{L} + I_x\Delta\widetilde{N})
\end{aligned} \tag{2.45}$$

If we perturb the Equation (2.25), the linearized equations can be written as follows:

$$\begin{aligned}
\Delta\dot{\theta} &= \Delta q \\
\Delta\dot{\phi} &= p + q\tan\theta_0 \\
\Delta\dot{\psi} &= r\sec\theta_0
\end{aligned} \tag{2.46}$$

The equations so far are not specific to an aircraft. They can be used for every aircraft. Aerodynamic forces $(\Delta\widetilde{X}, \Delta\widetilde{Y}, \Delta\widetilde{Z})$ and moments $(\Delta\widetilde{L}, \Delta\widetilde{M}, \Delta\widetilde{N})$ make the equations specific to an aircraft. These forces and moments are functions of many other variables. The engineers can decide these variables according to their importance.

Let us assume that the variables of $\Delta\widetilde{X}$,

$$\Delta\widetilde{X} = f(\widetilde{u}, \widetilde{w}, \delta_T) \tag{2.47}$$

If this equation is perturbed, we get

$$\Delta\widetilde{X} = \frac{\partial\widetilde{X}}{\partial\widetilde{u}}(\widetilde{u}-\widetilde{u}_0) + \frac{\partial\widetilde{X}}{\partial\widetilde{w}}(\widetilde{w}-\widetilde{w}_0) + \frac{\partial\widetilde{X}}{\partial\delta_t}(\delta_t-\delta_{t_0}) \tag{2.48}$$

$$\widetilde{X}_u = \frac{\partial\widetilde{X}}{\partial\widetilde{u}}, \qquad \widetilde{X}_w = \frac{\partial\widetilde{X}}{\partial\widetilde{w}}, \qquad \widetilde{X}_{\delta_t} = \frac{\partial\widetilde{X}}{\partial\delta_t} \tag{2.49}$$

$\widetilde{X}_u$,$\widetilde{X}_w$, and $\widetilde{X}_{\delta_t}$ have a special meaning. These derivatives are called "Aerodynamic Derivatives", and they are specific to the aircraft. These derivatives are related to aerodynamics. There are different methods to estimate them, such as wind tunnel or CFD (Computational Fluid Dynamics).

Thus, if all of the force and moments can be written as Equation (2.48), the forces and moments become

$$\begin{aligned}
\Delta\widetilde{X} &= \widetilde{X}_u\Delta\widetilde{u} + \widetilde{X}_w\widetilde{w} + \Delta\widetilde{X}_C \\
\Delta\widetilde{Y} &= \widetilde{Y}_v\widetilde{v} + \widetilde{Y}_p p + \widetilde{Y}_r r + \Delta\widetilde{Y}_C \\
\Delta\widetilde{Z} &= \widetilde{Z}_u\Delta\widetilde{u} + \widetilde{Z}_w\widetilde{w} + \widetilde{Z}_{\dot{w}}\dot{\widetilde{w}} + \widetilde{Z}_q q + \Delta\widetilde{Z}_C \\
\Delta\widetilde{L} &= \widetilde{L}_v\widetilde{v} + \widetilde{L}_p p + \widetilde{L}_r r + \Delta\widetilde{L}_C \\
\Delta\widetilde{M} &= \widetilde{M}_u\Delta\widetilde{u} + \widetilde{M}_w\widetilde{w} + \widetilde{M}_{\dot{w}}\dot{\widetilde{w}} + \widetilde{M}_q q + \Delta\widetilde{M}_C \\
\Delta\widetilde{N} &= \widetilde{N}_v\widetilde{v} + \widetilde{N}_p p + \widetilde{N}_r r + \Delta\widetilde{N}_C
\end{aligned} \tag{2.50}$$

If these force and moments are substituted into Equations (2.44) and (2.45), the following equations are obtained. The motion of a fixed-wing aircraft can be separated into "Longitudinal" and "Lateral". That means the effects of the longitudinal and lateral motions on each other are negligible. Equation (2.51) represents the linearized longitudinal motion and Equation (2.52) represents the linearized lateral motion.

$$\begin{bmatrix} \Delta\dot{\widetilde{u}} \\ \dot{\widetilde{w}} \\ \dot{q} \\ \Delta\dot{\theta} \end{bmatrix} = \begin{bmatrix} \\ A_{long} \\ \\ \end{bmatrix} \begin{bmatrix} \Delta\widetilde{u} \\ \widetilde{w} \\ q \\ \Delta\theta \end{bmatrix} + \begin{bmatrix} \frac{\Delta\widetilde{X}_c}{m} \\ \frac{\Delta\widetilde{Z}_c}{m-\widetilde{Z}_{\dot{w}}} \\ \frac{\Delta\widetilde{M}_c}{I_y} + \frac{\widetilde{M}_{\dot{w}}}{I_y}\frac{\Delta\widetilde{Z}_C}{m-\widetilde{Z}_{\dot{w}}} \\ 0 \end{bmatrix} \tag{2.51}$$

$$A_{long} = \begin{bmatrix} \frac{\widetilde{X}_u}{m} & \frac{\widetilde{X}_w}{m} & 0 & -g\cos\theta_0 \\ \frac{\widetilde{Z}_u}{m-\widetilde{Z}_{\dot{w}}} & \frac{\widetilde{Z}_w}{m-\widetilde{Z}_{\dot{w}}} & \frac{\widetilde{Z}_q+m\widetilde{u}_0}{m-\widetilde{Z}_{\dot{w}}} & \frac{-mg\sin\theta_0}{m-\widetilde{Z}_{\dot{w}}} \\ \frac{1}{I_y}\left[\widetilde{M}_u + \frac{\widetilde{M}_{\dot{w}}\widetilde{Z}_u}{m-\widetilde{Z}_{\dot{w}}}\right] & \frac{1}{I_y}\left[\widetilde{M}_w + \frac{\widetilde{M}_{\dot{w}}\widetilde{Z}_w}{m-\widetilde{Z}_{\dot{w}}}\right] & \frac{1}{I_y}\left[\widetilde{M}_q + \frac{\widetilde{M}_{\dot{w}}(\widetilde{Z}_q+m\widetilde{u}_0)}{m-\widetilde{Z}_{\dot{w}}}\right] & \frac{-\widetilde{M}_{\dot{w}}mg\sin\theta_0}{I_y(m-\widetilde{Z}_{\dot{w}})} \\ 0 & 0 & 1 & 0 \end{bmatrix}$$

$$\begin{bmatrix} \dot{\widetilde{v}} \\ \dot{p} \\ \dot{r} \\ \dot{\phi} \end{bmatrix} = \begin{bmatrix} \\ A_{lat} \\ \\ \end{bmatrix} \begin{bmatrix} \widetilde{v} \\ p \\ r \\ \phi \end{bmatrix} + \begin{bmatrix} \frac{\Delta\widetilde{Y}_c}{m} \\ \frac{\Delta\widetilde{L}_c}{I'_x} + I'_{zx}\widetilde{N}_c \\ I'_{zx}\Delta\widetilde{L}_c + \frac{\Delta\widetilde{N}_c}{I'_z} \\ 0 \end{bmatrix} \tag{2.52}$$

$$A_{lat} = \begin{bmatrix} \frac{\widetilde{Y}_v}{m} & \frac{\widetilde{Y}_p}{m} & \left(\frac{\widetilde{Y}_r}{m} - \widetilde{u}_0\right) & g\cos\theta_0 \\ \left(\frac{\widetilde{L}_v}{I'_x} + I'_{zx}\widetilde{N}_v\right) & \left(\frac{\widetilde{L}_p}{I'_x} + I'_{zx}\widetilde{N}_p\right) & \left(\frac{\widetilde{L}_r}{I'_x} + I'_{zx}\widetilde{N}_r\right) & 0 \\ \left(I'_{zx}\widetilde{L}_v + \frac{\widetilde{N}_v}{I'_z}\right) & \left(I'_{zx}\widetilde{L}_p + \frac{\widetilde{N}_p}{I'_z}\right) & \left(I'_{zx}\widetilde{L}_r + \frac{\widetilde{N}_r}{I'_z}\right) & 0 \\ 0 & 0 & \tan\theta_0 & 0 \end{bmatrix}$$

# 3
# $\mathscr{H}_\infty$ SYNTHESIS

## 3.1 Introduction

The term $H_\infty$ comes from the Hardy space, which is the name of the mathematical space where the optimization is performed. The $H_\infty$ norm is the maximum singular value of a function in that space. The $H_\infty$ method is used in the control theory to design the stabilized controllers with the desired performance. A control problem turns into a mathematical optimization problem owing to the $H_\infty$ method, and the solution to this problem also means finding the desired controller. The most important advantage of the $H_\infty$ method over the conventional controllers is that it can be used in the multivariable system problems [65]. Besides, it is necessary to deal with very complex mathematical formulas and to know the mathematical model of the system that is desired to be controlled sufficiently. Also, the nonlinear expressions such as the saturation are often not used. The implementation of this method does not mean that the best controller is found in terms of the performance criteria. The found controller is only optimal based on the cost functions specified.

G. Zames firstly described $H_\infty$ problem in 1981 [66]. Actually, Small Gain Theory, which is also introduced by G.Zames in the 1960s, can be accepted as the origin of the $H_\infty$ method [67, 68]. In 1989, Doyle, Glover, Khargonekar, and Francis showed that a controller as the solution of $H_\infty$ problem exists if and only if unique stabilizing solutions to two Algebraic Riccati Equations are positive definite and the spectral radius of their product is less than $\gamma^2$ [69]. In 1994, P. Gahinet and P. Apkarian solved LMI based $H_\infty$ problem by using Algebraic Riccati Inequalities instead of Algebraic Riccati Equations [70]. In 2006, the new algorithms that minimize the $H_\infty$ norm by adding structural constraints to controller dynamics were introduced by P. Apkarian and D. Noll [71].

$H_\infty$ problem can be expressed as

$$\begin{array}{ll} \text{minimize} & \|T_{w\to z}(P,K)\|_\infty \\ \text{subject to} & K \; stabilizes \; P \\ & K \in \mathscr{K} \end{array} \tag{3.1}$$

where $K \in \mathscr{K}$ represents a structural constraint on the controller, and P and K represent the system and controller matrices, respectively. $T_{w\to z}(P,K)$ represents the closed-loop transfer function containing the effect of the exogenous input $w$ to performance output $z$.

## 3.2 $\mathscr{H}_\infty$ Norm for SISO Systems

A single input and single output system can be depicted as in Figure 3.1.

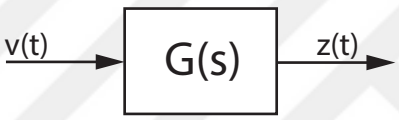


**Figure 3.1** SISO system

$H_\infty$ norm for a stable, proper single-input and single-output (SISO) system with the transfer function $G(s)$ is

$$\|G(s)\|_\infty = \sup_\omega |G(j\omega)| \tag{3.2}$$

$|G(j\omega)|$ is a magnification factor of a system. An input signal having $\omega$ angular frequency is magnified by $|G(j\omega)|$. Therefore, $H_\infty$ is a measure of the maximum magnification factor [72].

Let $v(t)$ be a signal with Laplace transform $\hat{v}(s)$ such that its $L_2$ norm given in Equation (3.3) is bounded.

$$\|\hat{v}\|_2 = \left( \frac{1}{2\pi} \int_{-\infty}^{\infty} |\hat{v}(j\omega)|^2 d\omega \right)^{1/2} \tag{3.3}$$

Thus, the system output $\hat{z}(s) = G(s)\hat{v}(s)$ has the $L_2$ norm which is bounded above by $\|G\|_\infty \|\hat{v}\|_2$, because

$$
\begin{aligned}
\|G\hat{v}\|_2 &= \left( \frac{1}{2\pi} \int_{-\infty}^{\infty} |G(j\omega)\hat{v}(j\omega)|^2 d\omega \right)^{1/2} \\
&= \left( \frac{1}{2\pi} \int_{-\infty}^{\infty} |G(j\omega)|^2 |\hat{v}(j\omega)|^2 d\omega \right)^{1/2} \\
&\leq \sup_{\omega} |G(j\omega)| \left( \frac{1}{2\pi} \int_{-\infty}^{\infty} |\hat{v}(j\omega)|^2 d\omega \right)^{1/2} \\
&= \|G(s)\|_\infty \|\hat{v}\|_2
\end{aligned}
\tag{3.4}
$$

Therefore

$$
\begin{aligned}
\|G\hat{v}\|_2 &\leq \|G(s)\|_\infty \|\hat{v}\|_2 \\
\|G(s)\|_\infty &\geq \frac{\|G\hat{v}\|_2}{\|\hat{v}\|_2} \qquad \forall \hat{v} \neq 0
\end{aligned}
\tag{3.5}
$$

The $H_\infty$ norm can be expressed as

$$
\|G(s)\|_\infty = \sup \left\{ \frac{\|G\hat{v}\|_2}{\|\hat{v}\|_2} : \quad \hat{v} \neq 0 \right\} \tag{3.6}
$$

The $L_2$ norm of an input is magnified by the gain of the system ($\|G(s)\|_\infty$) which is the maximum multiplier. The $H_\infty$ norm of $\|G(s)\|_\infty$ gives the maximum factor. This is illustrated in Figure 3.2 [73].

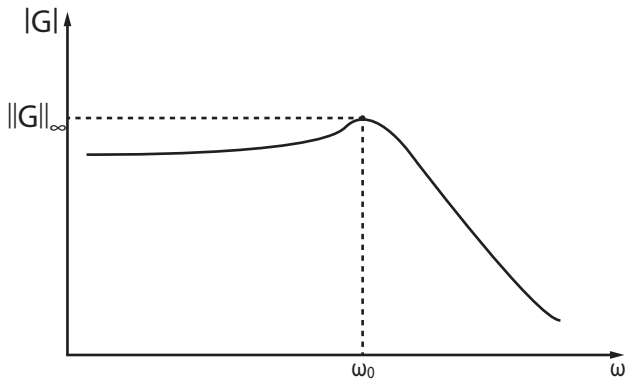


**Figure 3.2** $H_\infty$ norm as peak value in the frequency response

## 3.3 $\mathscr{H}_\infty$ Norm for MIMO Systems

The gain obtained for the SISO system in the previous section can be generalized for the multiple-input and multiple-output (MIMO) systems. Let the transfer function be $nxm$ dimensional matrix. The Euclidean norm $\|v\|$ of a complex-valued vector $v = [v_1, ..., v_m]^T \in \mathbb{C}^m$ is

$$\|v\| = (|v_1|^2 + \cdots + |v_m|^2)^{1/2} \tag{3.7}$$

The maximum gain of $G$ at the frequency $\omega$ can be expressed as

$$\begin{aligned} \|G(j\omega)\| &= \max_v \left\{ \frac{\|G(j\omega)v\|}{\|v\|} : \quad v \neq 0, \quad v \in \mathbb{C}^m \right\} \\ &= \max_v \{ \|G(j\omega)v\| : \quad \|v\| = 1, \quad v \in \mathbb{C}^m \} \end{aligned} \tag{3.8}$$

The $H_\infty$ norm of the transfer function $G(s)$ is given as

$$\|G\|_\infty = \sup_\omega \|G(j\omega)\| \tag{3.9}$$

As the matrix norm $\|G(j\omega)\|$ is equal to the maximum singular value $\bar{\sigma}(G(j\omega))$ of the matrix $G(j\omega)$, the $H_\infty$ norm can be expressed as follows:

$$\|G\|_\infty = \sup_\omega \bar{\sigma}(G(j\omega)) \tag{3.10}$$

The $H_\infty$ norm is represented in Figure 3.3 [73]. $\bar{\sigma}(G)$ and $\underline{\sigma}(G)$ are the notation of the maximum and minimum singular values of the matrix $G(j\omega)$, respectively. Figure 3.3 shows the peak value of the maximum singular value over frequency.

Suppose that $v$ is a signal with the bounded $L_2$ norm, and $\hat{v}(s)$ is its Laplace transform. Then the $L_2$ norm of the system output $\hat{z}(s) = G(s)\hat{v}(s)$ becomes bounded. [1]

[1] Unlike the SISO system, for a vector-valued signal $v(t) = [v_1(t), ..., v_m(t)]^T$, $L_2$ norm can be expressed as follows,

$$\|v\|_2 = \left( \sum_{i=1}^{m} \|v_i\|_2^2 \right)^{1/2} = \left( \int_0^\infty \sum_{i=1}^{m} v_i^2 dt \right)^{1/2} = \left( \int_0^\infty v^T(t)v(t)dt \right)^{1/2}$$

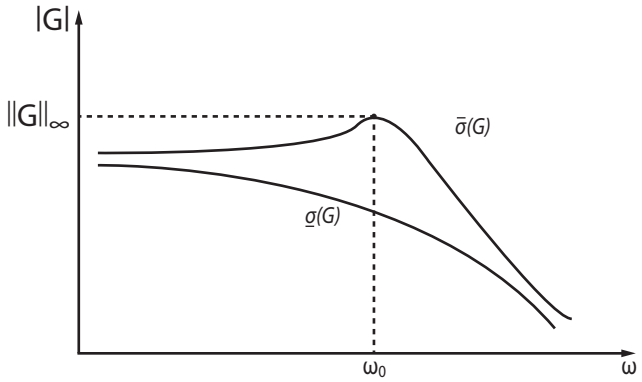


**Figure 3.3** $H_\infty$ norm as peak value over frequency

$$
\begin{aligned}
\|G\hat{v}\|_2 &= \left( \frac{1}{2\pi} \int_{-\infty}^{\infty} \hat{v}(-j\omega)^T G(-j\omega)^T G(j\omega)\hat{v}(j\omega) d\omega \right)^{1/2} \\
&= \left( \frac{1}{2\pi} \int_{-\infty}^{\infty} \|G(j\omega)\hat{v}(j\omega)\|^2 d\omega \right)^{1/2} \\
&\leq \left( \frac{1}{2\pi} \int_{-\infty}^{\infty} \|G(j\omega)\| \|\hat{v}(j\omega)\|^2 d\omega \right)^{1/2} \\
&\leq \sup_{\omega} \|G(j\omega)\| \left( \frac{1}{2\pi} \int_{-\infty}^{\infty} \|\hat{v}(j\omega)\|^2 d\omega \right)^{1/2} \\
&= \|G\|_\infty \|\hat{v}\|_2
\end{aligned}
\tag{3.11}
$$

---

Similarly, for the Laplace-domain signal $\hat{v}(s) = [\hat{v}_1(s), \cdots, \hat{v}_m(s)]^T$,

$$
\begin{aligned}
\|\hat{v}\|_2 &= \left( \sum_{i=1}^{m} \|\hat{v}_i\|_2^2 \right)^{1/2} \\
&= \left( \frac{1}{2\pi} \int_{-\infty}^{\infty} \sum_{i=1}^{m} |\hat{v}_i(j\omega)|^2 d\omega \right)^{1/2} \\
&= \left( \frac{1}{2\pi} \int_{-\infty}^{\infty} \sum_{i=1}^{m} \hat{v}_i(-j\omega)\hat{v}_i(j\omega) d\omega \right)^{1/2} \\
&= \left( \frac{1}{2\pi} \int_{-\infty}^{\infty} \hat{v}_i(-j\omega)^T \hat{v}_i(j\omega) d\omega \right)^{1/2}
\end{aligned}
$$

Thus

$$\|G(s)\|_\infty = \sup\left\{\frac{\|G\hat{v}\|_2}{\|\hat{v}\|_2} : \quad \hat{v} \neq 0\right\} \tag{3.12}$$

## 3.4 $\mathscr{H}_\infty$ Synthesis

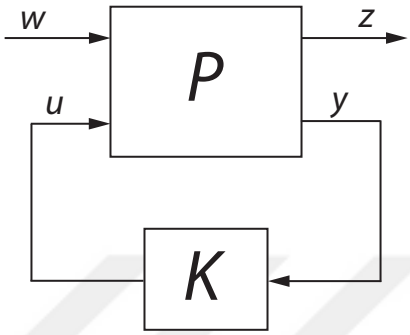


**Figure 3.4** General P-K form

The purpose here is to minimize the $H_\infty$ norm of the transfer function from $w$ to $z$. More precisely, it is aimed to obtain $K$ controller generating a control signal $u$ that resists the effect of $w$ on $z$ according to the information coming from $y$ [74]. The system equation belongs to $P$ is given by

$$\begin{aligned} \dot{x}(t) &= Ax(t) + B_1 w(t) + B_2 u(t) \\ z(t) &= C_1 x(t) + D_{11} w(t) + D_{12} u(t) \\ y(t) &= C_2 x(t) + D_{21} w(t) + D_{22} u(t) \end{aligned} \tag{3.13}$$

P can be written in a matrix form as follows:

$$P(s) = \left[\begin{array}{c|cc} A & B_1 & B_2 \\ \hline C_1 & D_{11} & D_{12} \\ C_2 & D_{21} & D_{22} \end{array}\right] \tag{3.14}$$

The dynamic controller is represented as

$$\begin{aligned} \dot{x}_k(t) &= A_k x_k(t) + B_k y(t) \\ u(t) &= C_k x_k(t) + D_k y(t) \end{aligned} \tag{3.15}$$

$$K(s) = \begin{bmatrix} A_k & B_k \\ C_k & D_k \end{bmatrix} \tag{3.16}$$

If $u(t)$ in (3.15) is substituted into (3.13) and $y(t)$ in (3.13) is substituted into (3.15), then the closed loop system can be written as follows:

$$\begin{bmatrix} \dot{x}(t) \\ \dot{x}_k(t) \\ \hline z(t) \end{bmatrix} = \underbrace{\left[\begin{array}{cc|c} A+B_2D_kQC_2 & B_2(I+D_kQD_{22})C_k & B_1+B_2D_kQD_{21} \\ B_kQC_2 & A_k+B_kQD_{22}C_k & B_kQD_{21} \\ \hline C_1+D_{12}D_kQC_2 & D_{12}(I+D_kQD_{22})C_k & D_{11}+D_{12}D_kQD_{21} \end{array}\right]}_{\underline{S}(G,K)} \begin{bmatrix} x(t) \\ x_k(t) \\ \hline w(t) \end{bmatrix} \tag{3.17}$$

where $Q=(I-D_{22}D_k)^{-1}$. If Equation (3.17) is simplified by creating new variables as

$$\begin{aligned} A_{k2} &= A_k + B_kQD_{22}C_k \\ B_{k2} &= B_kQ \\ C_{k2} &= (I+D_kQD_{22})C_k \\ D_{k2} &= D_kQ \end{aligned} \tag{3.18}$$

Therefore, Equation (3.17) can be rewritten as follows [75]:

$$\begin{bmatrix} \dot{x}(t) \\ \dot{x}_k(t) \\ \hline z(t) \end{bmatrix} = \left[\begin{array}{cc|c} A+B_2D_{k2}C_2 & B_2C_{k2} & B_1+B_2D_{k2}D_{21} \\ B_{k2}C_2 & A_{k2} & B_{k2}D_{21} \\ \hline C_1+D_{12}D_{k2}C_2 & D_{12}C_{k2} & D_{11}+D_{12}D_{k2}D_{21} \end{array}\right] \tag{3.19}$$

The original variables can be recovered as

$$\begin{aligned} D_k &= (I+D_{k2}D_{22})^{-1}D_{k2} \\ B_k &= B_{k2}(I-D_{22}D_k) \\ C_k &= (I-D_kD_{22})C_{k2} \\ A_k &= A_{k2}-B_k(I-D_{22}D_k)^{-1}D_{22}C_k \end{aligned} \tag{3.20}$$

$\underline{S}(G,K)$ in Equation (3.17) represents the closed loop system and the simplified notations become

$$\underline{S}(G,K) = \begin{bmatrix} A_{cl} & B_{cl} \\ C_{cl} & D_{cl} \end{bmatrix} \tag{3.21}$$

The closed-loop relation can be parametrized in terms of the controller realization as follows [76]:

$$\begin{aligned} A_{cl} &= \bar{A} + \underline{B}K\underline{C} & B_{cl} &= \bar{B} + \underline{B}K\underline{D}_{12} \\ C_{cl} &= \bar{C} + \underline{D}_{12}K\underline{C} & D_{cl} &= D_{11} + \underline{D}_{12}K\underline{D}_{21} \end{aligned} \tag{3.22}$$

where

$$\begin{aligned} \bar{A} &= \begin{bmatrix} A & 0 \\ 0 & 0 \end{bmatrix} & \bar{B} &= \begin{bmatrix} B_1 \\ 0 \end{bmatrix} & \bar{C} &= \begin{bmatrix} C_1 & 0 \end{bmatrix} & \underline{C} &= \begin{bmatrix} 0 & I \\ C_2 & 0 \end{bmatrix} \\ \underline{B} &= \begin{bmatrix} 0 & B_2 \\ I & 0 \end{bmatrix} & \underline{D}_{12} &= \begin{bmatrix} 0 & D_{12} \end{bmatrix} & \bar{D}_{21} &= \begin{bmatrix} 0 \\ D_{21} \end{bmatrix} \end{aligned} \tag{3.23}$$

$\underline{S}(G,K)$ can be rewritten as

$$\begin{aligned} A_{cl} &= \begin{bmatrix} A & 0 \\ 0 & 0 \end{bmatrix} + \begin{bmatrix} 0 & B_2 \\ I & 0 \end{bmatrix} \begin{bmatrix} A_{k2} & B_{k2} \\ C_{k2} & D_{k2} \end{bmatrix} \begin{bmatrix} 0 & I \\ C_2 & 0 \end{bmatrix} \\ B_{cl} &= \begin{bmatrix} B_1 \\ 0 \end{bmatrix} + \begin{bmatrix} 0 & B_2 \\ I & 0 \end{bmatrix} \begin{bmatrix} A_{k2} & B_{k2} \\ C_{k2} & D_{k2} \end{bmatrix} \begin{bmatrix} 0 \\ D_{21} \end{bmatrix} \\ C_{cl} &= \begin{bmatrix} C_1 & 0 \end{bmatrix} + \begin{bmatrix} 0 & D_{12} \end{bmatrix} \begin{bmatrix} A_{k2} & B_{k2} \\ C_{k2} & D_{k2} \end{bmatrix} \begin{bmatrix} 0 & I \\ C_2 & 0 \end{bmatrix} \\ D_{cl} &= \begin{bmatrix} D_{11} \end{bmatrix} + \begin{bmatrix} 0 & D_{12} \end{bmatrix} \begin{bmatrix} A_{k2} & B_{k2} \\ C_{k2} & D_{k2} \end{bmatrix} \begin{bmatrix} 0 \\ D_{21} \end{bmatrix} \end{aligned} \tag{3.24}$$

$$\underline{S}(G,K) = \begin{bmatrix} A_{cl} & B_{cl} \\ C_{cl} & D_{cl} \end{bmatrix} = \begin{bmatrix} A & 0 & B_1 \\ 0 & 0 & 0 \\ C_1 & 0 & D_{11} \end{bmatrix} + \begin{bmatrix} 0 & B_2 \\ I & 0 \\ 0 & D_{12} \end{bmatrix} \begin{bmatrix} A_{k2} & B_{k2} \\ C_{k2} & D_{k2} \end{bmatrix} \begin{bmatrix} 0 & I & 0 \\ C_2 & 0 & D_{21} \end{bmatrix} \tag{3.25}$$

The performance criterion which is desired to be minimized can be taken as the $H_\infty$ norm of the closed-loop transfer function. Thus, the cost function takes the following form [77, 78].

$$J_\infty(K) = \|\underline{S}(G,K)\|_\infty \tag{3.26}$$

It is tough to minimize the $J_\infty(K)$ cost function directly. Instead, it is easier to investigate if there is a stabilizing controller that provides the $H_\infty$ norm constraints

as follows:

$$J_\infty(K) < \gamma \qquad \gamma > 0 \tag{3.27}$$

These constraints can be used to check if the inequalities in (3.27) are assured for the different $\gamma$ values. This is called "$\gamma - iteration$" method [72].

Now it is going to be looked for if there exists any controller which achieves the boundary conditions given in Equation (3.27) by taking advantage of Equation (3.12).

$$J_\infty(K) = \sup\left\{\frac{\|z\|_2}{\|w\|_2}, \quad w \neq 0\right\} \tag{3.28}$$

Thus, the relation between the cost function and boundary condition can be written as follow:

$$\frac{\|z\|_2}{\|w\|_2} < \gamma, \quad \forall\ \gamma \neq 0 \tag{3.29}$$

or

$$L(w,u) = \|z\|_2^2 - \gamma^2\|w\|_2^2 < 0, \quad \forall\ w \neq 0 \tag{3.30}$$

If Equation (3.30) is rewritten by considering Parseval's theorem, the time domain expression of the $L_2$ norm [2] becomes

$$L(w,u) = \int_0^\infty [z(t)^T z(t) - \gamma^2 w(t)^T w(t)]dt < 0, \quad \forall\ w \neq 0 \tag{3.31}$$

$$L(w,u) = \|z\|^2 - \gamma^2\|w\|^2 = z^T z - \gamma^2 w^T w \tag{3.32}$$

**Theorem 3.1.** *A strict upper bound V for the performance criterion $J_w$, such that $J_w(x) < V(x)$ for all w, can be established if there exists a continuously differentiable, positive definite Lyapunov or storage function, V , that makes the Hamiltonian, H, negative for all x and w:*

$$H = g(x,w) + V_x(x)f(x,w) < 0 \quad \forall\ x,w \tag{3.33}$$

*where $V_x = \frac{\partial}{\partial x}V$ denotes the partial derivative of V with respect to x.*

[2] Unlike the SISO system, for a vector-valued signal $v(t) = [v_1(t), ..., v_m(t)]^T$, $L_2$ norm can be generalized as follows,

$$\|v\|_2 = \left(\sum_{i=1}^m \|v_i\|_2^2\right)^{1/2} = \left(\int_0^\infty \sum_{i=1}^m v_i^2 dt\right)^{1/2} = \left(\int_0^\infty v^T(t)v(t)dt\right)^{1/2}$$

Therefore, let us choose a quadratic Lyapunov function as

$$V(x) = x^T P x \tag{3.34}$$

where the Lyapunov matrix $P$ is symmetric and positive definite ($P \succ 0$), that is $x^T P x > 0, \forall\, x \neq 0$. In case of $x(0) = 0$, the $L_2$-induced norm from w to z is less than one if the Hamiltonian is negative for all x:

$$\begin{aligned} H &= \dot{V} + g(x,w) \\ &= \dot{x}^T P x + x^T P \dot{x} + z^T z - \gamma^2 w^T w \\ &= x^T P(A_{cl}x + B_{cl}w) + (A_{cl}x + B_{cl}w)^T P x + (C_{cl}x + D_{cl}w)^T (C_{cl}x + D_{cl}w) - \gamma^2 w^T w \end{aligned} \tag{3.35}$$

$H < 0$ must hold for all $x$ and $w$ to meet the condition $\|z\|_2 < \gamma \|w\|_2$.

The Hamiltonian given in (3.35) can be written in matrix form as follows:

$$H = \begin{bmatrix} x \\ w \end{bmatrix}^T \begin{bmatrix} PA_{cl} + A_{cl}^T P + C_{cl}^T C_{cl} & PB_{cl} + C_{cl}^T D_{cl} \\ B_{cl}^T P + D_{cl}^T C_{cl} & D_{cl}^T D_{cl} - \gamma^2 I \end{bmatrix} \begin{bmatrix} x \\ w \end{bmatrix} < 0, \qquad \forall\, x, w \neq 0 \tag{3.36}$$

In order to meet the condition above, the following condition must be met.

$$\begin{bmatrix} PA_{cl} + A_{cl}^T P + C_{cl}^T C_{cl} & PB_{cl} + C_{cl}^T D_{cl} \\ B_{cl}^T P + D_{cl}^T C_{cl} & D_{cl}^T D_{cl} - \gamma^2 I \end{bmatrix} < 0 \tag{3.37}$$

**Definition 3.1** (**Congruence Transformation**)**.** Suppose that A and B are Hermitian [3]. A and B are said to be "Congruence" to each other if there exists an invertible matrix $T \in \mathbb{C}^{nxn}$ such that

$$A = T^* B T$$

According to this definition, the number of positive and negative eigenvalues of $B$ are same with $A$. Therefore, if $B$ is positive definite, $A$ is also positive definite or vice versa.

[3] **Hermitian Matrices :** $A \in \mathbb{C}^{nxn}$ is Hermitian if $A^* = A$.

**Lemma 3.2** (**Schur Complement**). *Suppose that R and S are Hermitian, then the following conditions are equivalent:*

- $R < 0, \qquad S - G^T R^{-1} G < 0$
- $\begin{bmatrix} S & G^T \\ G & R \end{bmatrix} < 0$

Therefore, the inequality (3.37) can be rewritten as

$$\underbrace{\begin{bmatrix} PA_{cl} + A_{cl}^T P & PB_{cl} \\ B_{cl}^T P & -\gamma^2 I \end{bmatrix}}_{\mathrm{S}} + \underbrace{\begin{bmatrix} C_{cl}^T \\ D_{cl}^T \end{bmatrix}}_{G^T} \underbrace{I}_{-R^{-1}} \underbrace{\begin{bmatrix} C_{cl} & D_{cl} \end{bmatrix}}_{\mathrm{G}} < 0 \tag{3.38}$$

which yields

$$\begin{bmatrix} PA_{cl} + A_{cl}^T P & PB_{cl} & C_{cl}^T \\ B_{cl}^T P & -\gamma^2 I & D_{cl}^T \\ C_{cl} & D & -I \end{bmatrix} < 0 \tag{3.39}$$

If P is scaled, then

$$\begin{bmatrix} PA_{cl} + A_{cl}^T P & PB_{cl} & C_{cl}^T \\ B_{cl}^T P & -\gamma I & D_{cl}^T \\ C_{cl} & D & -\gamma I \end{bmatrix} < 0 \tag{3.40}$$

**Lemma 3.3.** *Suppose* $\underline{S}(G,K) = \begin{bmatrix} A_{cl} & B_{cl} \\ C_{cl} & D_{cl} \end{bmatrix}$, *then the followings are equivalent:*

- *The matrix* $A_{cl}$ *is Hurwitz and*

$$\|\underline{S}(G,K)\|_\infty < \gamma$$

- *There exists a solution* $X_{cl} > 0$ *to the LMI*

$$\begin{bmatrix} X_{cl}A_{cl} + A_{cl}^T X_{cl} & X_{cl}B_{cl} & C_{cl}^T \\ B_{cl}^T X_{cl} & -\gamma I & D_{cl}^T \\ C_{cl} & D & -\gamma I \end{bmatrix} < 0$$

**Lemma 3.4** (**Transformation Lemma**). *Suppose that*

$$\begin{bmatrix} Y_1 & I \\ I & X_1 \end{bmatrix} > 0$$

*Then, there exist* $X_2, X_3, Y_2, Y_3$ *such that*

$$X = \begin{bmatrix} X_1 & X_2 \\ X_2^T & X_3 \end{bmatrix} = \begin{bmatrix} Y_1 & Y_2 \\ Y_2^T & Y_3 \end{bmatrix}^{-1} = Y^{-1} > 0$$

*where* $Y_{cl} = \begin{bmatrix} Y_1 & I \\ Y_2^T & 0 \end{bmatrix}$ *has full rank.*

**Lemma 3.5** (**Converse Transformation Lemma**). *Given* $X = \begin{bmatrix} X_1 & X_2 \\ X_2^T & X_3 \end{bmatrix} > 0$ *where* $X_2$ *has full column rank. Let*

$$X^{-1} = Y = \begin{bmatrix} Y_1 & Y_2 \\ Y_2^T & Y_3 \end{bmatrix}$$

*then*

$$\begin{bmatrix} Y_1 & I \\ I & X_1 \end{bmatrix} > 0$$

*and* $Y_{cl} = \begin{bmatrix} Y_1 & I \\ Y_2^T & 0 \end{bmatrix}$ *has full rank.*

Let's suppose that there exist $X_1, Y_1, A_n, B_n, C_n$, and $D_n$ such that the LMI is feasible. We can define the variables as follows:

$$\begin{bmatrix} A_n & B_n \\ C_n & D_n \end{bmatrix} = \begin{bmatrix} X_2 & X_1 B_2 \\ 0 & I \end{bmatrix} \begin{bmatrix} A_{k2} & B_{k2} \\ C_{k2} & D_{k2} \end{bmatrix} \begin{bmatrix} Y_2^T & 0 \\ C_2 Y_1 & I \end{bmatrix} + \begin{bmatrix} X_1 A Y_1 & 0 \\ 0 & 0 \end{bmatrix} \tag{3.41}$$

where $A_{k2}, B_{k2}, C_{k2}$, and $D_{k2}$ are given in Equation (3.18). Thus, Equation (3.25) can be rewritten as

$$\begin{bmatrix} A_{cl} & B_{cl} \\ C_{cl} & D_{cl} \end{bmatrix} = \begin{bmatrix} A & 0 & B_1 \\ 0 & 0 & 0 \\ C_1 & 0 & D_{11} \end{bmatrix} + \begin{bmatrix} 0 & B_2 \\ I & 0 \\ 0 & D_{12} \end{bmatrix} \begin{bmatrix} X_2 & X_1 B_2 \\ 0 & I \end{bmatrix}^{-1} \left( \begin{bmatrix} A_n & B_n \\ C_n & D_n \end{bmatrix} - \begin{bmatrix} X_1 A Y_1 & 0 \\ 0 & 0 \end{bmatrix} \right)$$

$$\begin{bmatrix} Y_2^T & 0 \\ C_2 Y_1 & I \end{bmatrix}^{-1} \begin{bmatrix} 0 & I & 0 \\ C_2 & 0 & D_{21} \end{bmatrix} \tag{3.42}$$

Therefore, if the LMI in Lemma 2 is expanded out, we obtain

$$\begin{bmatrix} AY_1 + Y_1A^T + B_2C_n + C_n^TB_2^T & *^T & *^T & *^T \\ A^T + A_n + [B_2D_nC_2]^T & X_1A + A^TX_1 + B_nC_2 + C_2^TB_n^T & *^T & *^T \\ [B_1 + B_2D_nD_{21}]^T & [XB_1 + B_nD_{21}]^T & -\gamma I & *^T \\ C_1Y_1 + D_{12}C_n & C_1 + D_{12}D_nC_2 & D_{11} + D_{12}D_nD_{21} & -\gamma I \end{bmatrix}$$

$$= \begin{bmatrix} Y_{cl}^T & 0 & 0 \\ 0 & I & 0 \\ 0 & 0 & I \end{bmatrix} \begin{bmatrix} X_{cl}A_{cl} + A_{cl}^TX_{cl} & X_{cl}B_{cl} & C_{cl}^T \\ B_{cl}^TX_{cl} & -\gamma I & D_{cl}^T \\ C_{cl} & D & -\gamma I \end{bmatrix} \begin{bmatrix} Y_{cl} & 0 & 0 \\ 0 & I & 0 \\ 0 & 0 & I \end{bmatrix} < 0 \tag{3.43}$$

Now, we can write the theorem [79].

**Theorem 3.6.** *The followings are equivalent.*

- *There exists a* $K(s) = \begin{bmatrix} A_k & B_k \\ C_k & D_k \end{bmatrix}$ *such that* $\|\underline{S}(G,K)\|_\infty < \gamma$.
- *There exist* $X_1, Y_1, A_n, B_n, C_n$, *and* $D_n$ *such that*

$$\begin{bmatrix} Y_1 & I \\ I & X_1 \end{bmatrix} > 0 \tag{3.44}$$

$$\begin{bmatrix} AY_1 + Y_1A^T + B_2C_n + C_n^TB_2^T & *^T & *^T & *^T \\ A^T + A_n + [B_2D_nC_2]^T & X_1A + A^TX_1 + B_nC_2 + C_2^TB_n^T & *^T & *^T \\ [B_1 + B_2D_nD_{21}]^T & [XB_1 + B_nD_{21}]^T & -\gamma I & *^T \\ C_1Y_1 + D_{12}C_n & C_1 + D_{12}D_nC_2 & D_{11} + D_{12}D_nD_{21} & -\gamma I \end{bmatrix} < 0 \tag{3.45}$$

*Moreover,*

$$\begin{bmatrix} A_{k2} & B_{k2} \\ C_{k2} & D_{k2} \end{bmatrix} = \begin{bmatrix} X_2 & X_1B_2 \\ 0 & I \end{bmatrix}^{-1} \left[ \begin{bmatrix} A_n & B_n \\ C_n & D_n \end{bmatrix} - \begin{bmatrix} X_1AY_1 & 0 \\ 0 & 0 \end{bmatrix} \right] \begin{bmatrix} Y_2^T & 0 \\ C_2Y_1 & I \end{bmatrix}^{-1} \tag{3.46}$$

*for any full rank* $X_2$ *and* $Y_2$ *such that*

$$\begin{bmatrix} X_1 & X_2 \\ X_2^T & X_3 \end{bmatrix} = \begin{bmatrix} Y_1 & Y_2 \\ Y_2^T & Y_3 \end{bmatrix}^{-1}$$

To construct a dynamic controller K as shown in Equation (3.20), the LMIs in Equation (3.44) and (3.45) have to be solved. In this thesis, the LMIs are solved by using YALMIP and SEDUMI, which is a semidefinite programming solver. $\gamma$ is initialized to a value, and the LMIs are solved. $\gamma$ is iterated downward until an optimal solution is found. Once this iteration process is done, we have everything to construct the controller, as described in Equation (3.20). The code for the $H_\infty$ synthesis is given in Appendix A.

# 4
# MATHEMATICAL MODELS

## 4.1 Model Following Method

The purpose of the model following method is to force the state or states of a real system to behave like the state or states of a reference system by finding a control input for the real system [80]. The reference system has a known mathematical model. More precisely, the model following method is to force $x_p$ states of a linear system given by

$$\dot{x}_p = A_p x_p + B_p u_p, \qquad x_p \in \mathbb{R}^n \quad and \quad u_p \in \mathbb{R}^m \tag{4.1}$$

to behave like $x_m$ states of a reference model given by

$$\dot{x}_m = A_m x_m + B_m u_m, \qquad x_m \in \mathbb{R}^n \quad and \quad u_m \in \mathbb{R}^m \tag{4.2}$$

The model following method is widely used in aircraft control systems. The ideal model having the desired performance is obtained with the help of the flying qualities specifications, and then the aircraft is expected to act as this ideal model [61]. By adjusting the structure of the control system and gains properly, it is possible to achieve a response close to the ideal model.

The model following method is divided into two groups according to the application type. One of them is the "Implicit", and the other one is the "Explicit" model following method.

### 4.1.1 Implicit Model Following Method

In this method, the reference model equations are only used when determining the control gains during the design process. The equations are not needed later [81]. As seen in Figure 4.1, the control inputs of the real system consist of the system states and the external inputs. There is no relation between the ideal model states and the closed-loop system. The model states $x_m$ are only seen in the performance index [80]. Therefore, this method is also called as "Model in the Performance Index".

The implicit model following method allows for continuous error correction and is effective on disturbances [80]. Since this method is not be used in our thesis, this much information is sufficient for now.

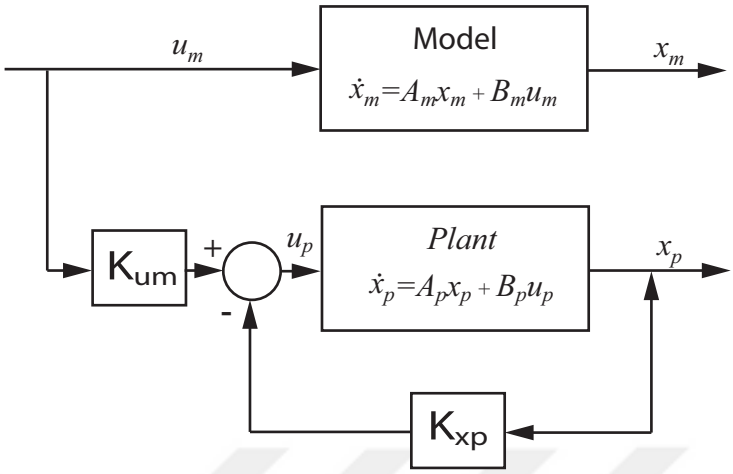


**Figure 4.1** Implicit model following

### 4.1.2 Explicit Model Following Method

This method is also called "Real Model Following" or "Model in the System". Unlike the implicit model following method, the control inputs of the real system consist of the state of the ideal model in addition to the real system states and the external state. The explicit model following method is more clearly expressed in the block diagram in Figure 4.2.

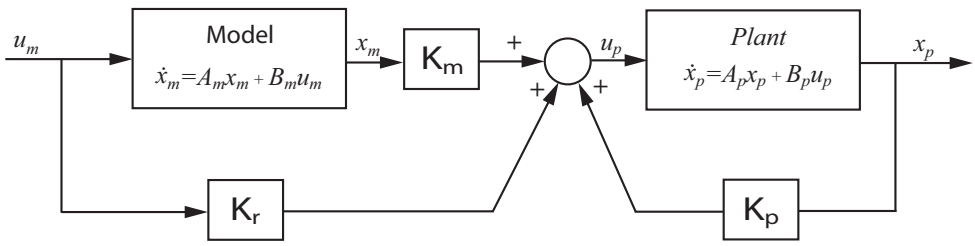


**Figure 4.2** Explicit model following

As can be seen from the figure, this method needs the state or states of the ideal model as part of the feed-forward controller. This method can be preferred when there is any uncertainty (such as disturbance or unknown parameters) in the system. Because it continuously tends to correct the error between the ideal model and real system states even in the presence of any unknown disturbances [80]. Therefore, it is stated in most of the studies that the explicit model following method reduces the sensitivity of the control system against the uncertainties [81].

The plant and model equations in Figure 4.2 were shown in Equations (4.1) and (4.2).

Let us assume that these equations are the same size. The controller input $u_p$ is

$$u_p = K_p x_p + K_m x_m + K_r u_m \tag{4.3}$$

If we add and subtract $K_m x_p$ to Equation (4.3), then we obtain

$$u_p = (K_p + K_m) x_p + K_m (x_m - x_p) + K_r u_m \tag{4.4}$$

If $e = x_m - x_p$, the last equation becomes

$$u_p = (K_p + K_m) x_p + K_m e + K_r u_m \tag{4.5}$$

It is seen that Figure 4.2 is equivalent to Figure 4.3.

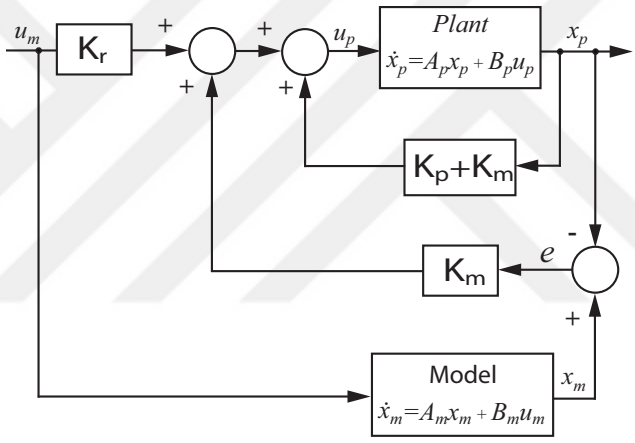


**Figure 4.3** Explicit equivalent model following

Thus, the following statements can be remarked [81]:

- The closed-loop plant dynamics can be determined by $K_p + K_m$.
- Plant state or states can follow the model state or states using only $K_p$ ($K_m = 0$) or only $K_m$ ($K_p = 0$) or any combination of $K_p$ and $K_m$ (but the sum of $K_p + K_m$ must remain same).
- The feedforward controller $K_r$ improves the tracking performance by providing rapid responses to the changes in the input of the ideal model.

## 4.2 Automatic Lateral Beam Tracking System

Radio navigation systems are commonly used to guide the aircraft to an appropriate position for landing. VOR (Very High-Frequency Omni-Directional Range) system is

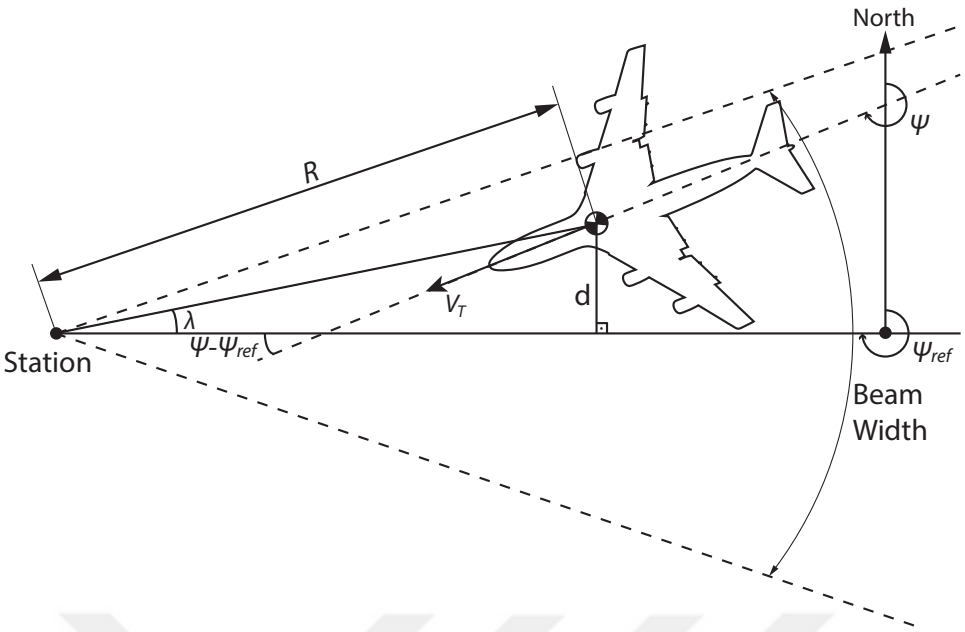


**Figure 4.4** Lateral beam guidance geometry

the most famous one among these systems, which operates in the range of 108.0 - 117.95 MHz. A VOR system consists of a ground component at the station and a receiver component in the aircraft. The ground station transmits very high frequency (VHF) radio signals, spreading all over the direction as the straight-line course (radials). These courses projected from the station are referenced to the magnetic north. The ground station emits two different signals. One of them is the omnidirectional reference signal, and the other one is the variable phase signal, which rotates clockwise in space 30 times a second and varies in phase [82]. The phase relationship between the reference and variable signal is measured by accepting the magnetic north as the baseline.

The receiver component in the aircraft is composed of a VOR antenna, a frequency selector, and an indicator. The two signals transmitted from the station are compared by the receiver component and encoded according to the phase relation between the reference and variable signal. This phase difference is measured electronically and converted to the degree of angle by the aircraft equipment; thus, the aircraft position is identified in azimuth around the beacon. An indicator on the instrument panel is used to visualize this information. Distance Measuring Equipment (DME) in the aircraft is also used to give a precise indication of the aircraft's distance from the VOR station.

Figure 4.4 represents the lateral beam tracking geometry [16]. $\lambda$ is the aircraft offset angle with respect to the main radial line and can be written as $\sin\lambda = d/R$ using the geometry. If $\lambda$ is desired to be in degree form and for the small angles, $\lambda$ becomes

$$\lambda \simeq 57.3d/R \tag{4.6}$$

Another equation from Figure 4.4 can be written as follows:

$$\dot{d} = V_T \sin(\psi - \psi_{ref}) \simeq V_T(\psi - \psi_{ref})$$

If $\psi$ and $\psi_{ref}$ are desired to be in degrees, then we get

$$\dot{d} \simeq (V_T/57.3)(\psi - \psi_{ref})$$
$$sd(s) \simeq (V_T/57.3)(\psi(s) - \psi_{ref})$$

$$\lambda(s) \simeq \frac{V_T}{R}(\frac{\psi(s) - \psi_{ref}}{s}) \tag{4.7}$$

$V_T$ is the aircraft true speed, $R$ is the shortest distance between the existing location of the aircraft and the ground station, and $\psi$ represents the aircraft heading angle with respect to the magnetic north. $\psi_{ref}$ represents the heading of the beam with respect to the magnetic north. $\psi_{ref}$ is set by the pilot, which is taken as zero for simplicity in this case. The purpose here for the automatic tracking system is to force $\lambda$ to be zero to align the aircraft at the center of the runway for landing.

## 4.3 Reference Models

### 4.3.1 Final Approach Phase:

It is assumed that the aircraft is approaching the airport at a certain angle. A reference trajectory has to be determined to align the aircraft at the center of the runway, which also means to bring down the aircraft offset angle $\lambda$ and lateral distance of the aircraft off course $d$ to zero. Figure 4.5 represents the reference trajectory. The mathematical model of the trajectory is assumed to be an exponential decay function and given by

$$\dot{d} = -\frac{1}{\tau}d + r, \qquad d(0) = d_0 \tag{4.8}$$

where $r$ is the reference model input.

If $r = 0$, then the solution becomes

$$h(t) = d_0 e^{(-t/\tau)} \tag{4.9}$$

The initial condition $d_0$ is the lateral distance of the aircraft off course and taken as 500 *ft* in this case. $\tau$ is the time constant and assumed to be 40 *sec*. Thus, the Eq. 4.9 becomes

$$h(t) = 500 e^{(-t/40)} \tag{4.10}$$

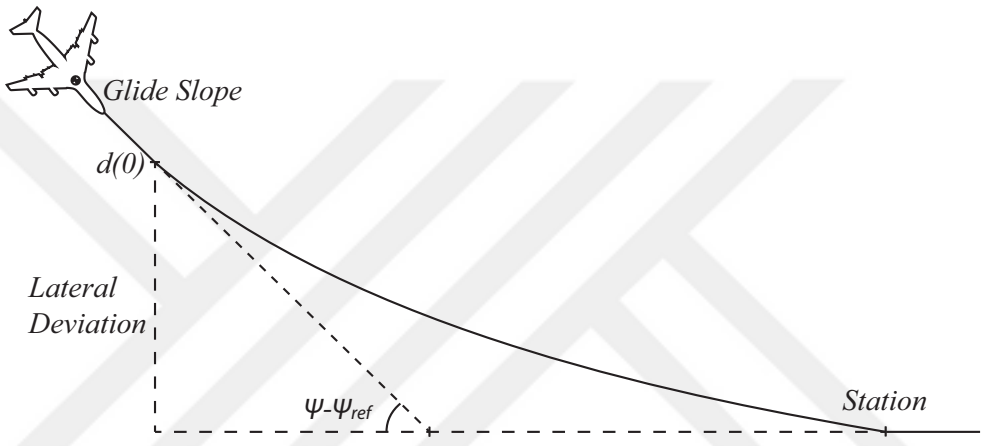


**Figure 4.5** Final approach trajectory

### 4.3.2 Flare Phase:

The flare phase of a flight approximately starts at the altitude level of 50 *ft*. The descent rate of the aircraft is decreased to about 2 *ft/s* or even less, the pitching angle is adjusted for the landing, and the velocity is decreased. A trajectory is predefined for the flare phase to have a smooth and comfortable touchdown to the runway [47]. This landing trajectory is defined as a reference model which is usually an exponential decay function given as follows [61]:

$$\dot{h} = -\frac{1}{\tau} h + r, \qquad h(0) = h_0 \tag{4.11}$$

where $r$ is the reference model input, and $h$ is the altitude. If $r = 0$, then the solution becomes

$$h(t) = h_0 e^{(-t/\tau)} \tag{4.12}$$

The initial condition $h_0$ is the last altitude level of the glideslope phase. $\gamma_R$ is the reference trajectory that is provided by a transmitter to guide the aircraft for the glideslope, $\tau$ is the time constant for the flare phase and can be found through $D$ which is shown in Figure 4.6 [61].

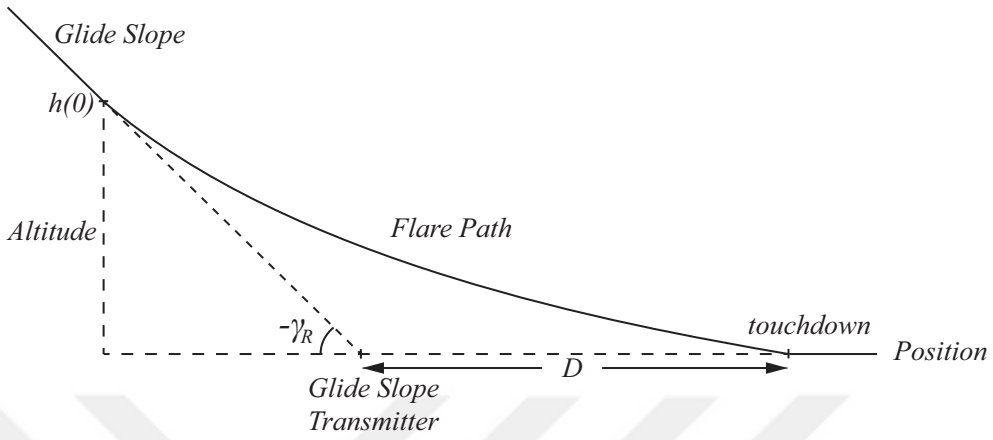


**Figure 4.6** Flare path

## 4.4 Windshear Model

Windshear is a rapid variation in wind speed and direction over a short period or distance. This variation can be described as either vertical (change in wind speed or direction with change in altitude) or horizontal (change in wind speed with change in lateral position for a certain altitude). The windshear is a meteorological phenomenon that may be caused by several reasons, such as the temperature difference between the ground and sky, thunderstorm, wind turbines, etc. The downburst, which is a type of the windshear, was firstly identified by Fujita [83] after a catastrophic accident at JFK Airport in 1975. During his research, he realized that the strong local downdrafts occur and hit the ground and spread out horizontally. Fujita named these downbursts according to the horizontal range they effect. If the diameter of a downburst is less than 4 $km$, it is called a microburst, otherwise macroburst. The microburst may last a few minutes, but its effects such as extreme speed and variation can be hazardous for the aircraft. The crash of Delta Flight 191 (DAL 191) at Dallas/Ft. Worth, on August 2, 1985, demonstrated how dangerous a microburst could be.

The windshear occurring at low altitudes creates severe risks for the aircraft during takeoff and landing. Figure 4.7 illustrates the windshear effect on the trajectory of the aircraft if there is no intervention by the pilot. When an aircraft encounters the downburst, it usually passes through three regions, each with a different effect on the aircraft. The aircraft firstly encounters an increasing headwind, which causes an increase in airspeed and pitching up. Thus, the aircraft flies above the glideslope. As

the aircraft approaches the middle of the downburst, the headwind loses its effect, and the downdraft starts being active. The angle of attack decreases during this transition. The angle of attack also decreases as the speed of the downdraft increases at this stage. As the angle of attack decreases, the aircraft pitches down and flies back to or even below the glideslope. When the downdraft loses its influence, the aircraft encounters an increasing tailwind, which causes a decrease in airspeed and pitching down. Thus, the aircraft flies below the glideslope and may even crash. All these events the aircraft is exposed to can take place in less than a minute. Therefore, it is obvious how hard it is for pilots to handle this complicated situation.

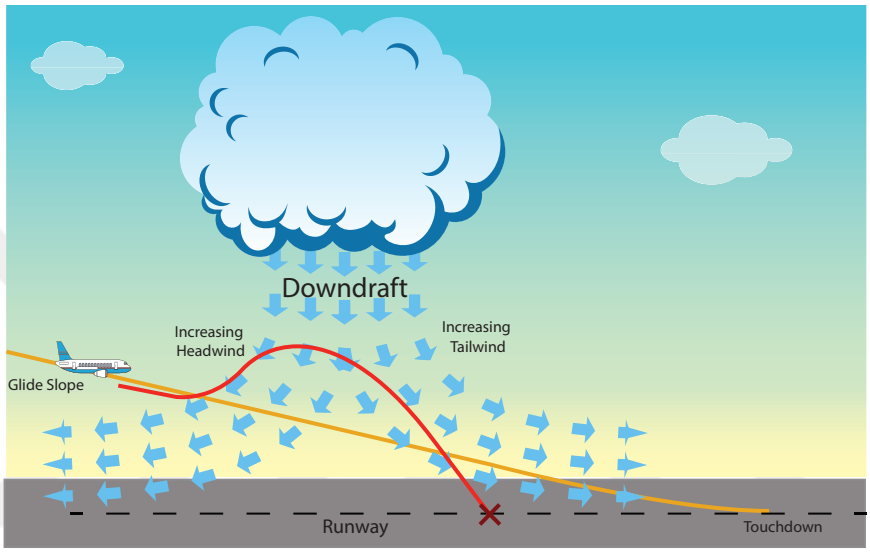


**Figure 4.7** Windshear effect

Pilots use actuators for the thrust and elevator to compensate for the windshear effect. The elevator controls the pitch attitude (in other words, the angle of attack), and the thrust controls the speed of the aircraft. The pilot can apply the recovery techniques using these controls. For example, when an aircraft encounters an increasing headwind, pilots decreases the airspeed and use the elevator to keep the aircraft on track. It should be noted that early recognition of the windshear is essential for the success of these techniques. A. Miele made a significant contribution to this field. He calculated optimal trajectories which the aircraft can track, and also developed guidance laws to control the aircraft when it encounters the downburst [84–87]. Bryson is another well-known contributor to this topic. He worked on dynamic optimization, optimal strategies, and feedback control techniques in the presence of the windshear during landing and takeoff [88–91].

Researchers have developed many different models to simulate the microburst. One approach is the vortex-ring model, which is firstly presented by Woodfield and Wood [92]. The vortex-ring induces velocity wind, and two symmetrical rings are used to

represent the microburst to satisfy boundary conditions. One of them is above the ground and called the primary vortex-ring. The other one is below the ground with the same strength and called the imaginary vortex-ring. The center of the vortex-ring is called the vortex filament. The vortex-ring model is illustrated in Figure 4.8. Multiple pairs of the vortex-rings are preferred for accuracy in practice. Simplified vortex-ring downburst model [93] is used for the flare phase simulations in this thesis. $R, r_C$, and $\Gamma$ represent the radius of the vortex-ring, the radius of the finite core, and vortex-ring model circulation, respectively. $\underline{X}, \underline{Y}$, and $H$ are the coordinates of the primary ring center.

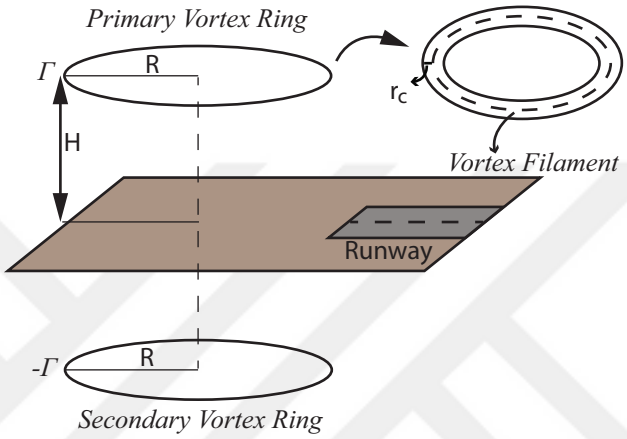


**Figure 4.8** Vortex-ring model

We can take $\underline{Y} = 0$ because the lateral movement is ignored in our study. If $x$ and $h$ horizontal and vertical point of interest, respectively, then the induced velocities are computed as follows [90]:

$$\begin{aligned} x_1 &= x - \underline{X} - R & x_2 &= x - \underline{X} + R \\ h_p &= h - H & h_m &= h + H \\ r_{1p} &= x_1^2 + h_p^2 & r_{2p} &= x_2^2 + h_p^2 \\ r_{1m} &= x_1^2 + h_m^2 & r_{2m} &= x_2^2 + h_m^2 \\ r_0 &= \min\{r_{1p}, r_{2p}\} & \zeta &= 1 - e^{-(r_0/r_c^2)} \end{aligned} \tag{4.13}$$

$$\begin{aligned} r_{xp} &= \sqrt{(x-\underline{X})^2 + h_p^2 + R^2} \\ r_{xm} &= \sqrt{(x-\underline{X})^2 + h_m^2 + R^2} \\ r_{hp} &= \left[(x-\underline{X})^2/4 + h_p^2 + R^2\right]^{3/4} \\ r_{hm} &= \left[(x-\underline{X})^2/4 + h_m^2 + R^2\right]^{3/4} \end{aligned}$$

If $r_0 < \varepsilon$ where $\varepsilon$ is a small number representing a point close to the ring filament,

then

$$W_x = 0 \qquad W_h = 0$$

Otherwise,

$$\begin{aligned} W_x &= \frac{1.182\Gamma\zeta}{2\pi}\left[\frac{R}{r_{xp}}\left(\frac{h_p}{r_{2p}}-\frac{h_p}{r_{1p}}\right)-\frac{R}{r_{xm}}\left(\frac{h_m}{r_{2m}}-\frac{h_m}{r_{1m}}\right)\right] \\ W_h &= \frac{1.576\Gamma\zeta}{2\pi}\left[\frac{R}{r_{hp}}\left(\frac{x_1}{r_{1p}^{3/4}}-\frac{x_2}{r_{2p}^{3/4}}\right)-\frac{R}{r_{hm}}\left(\frac{x_1}{r_{1m}^{3/4}}-\frac{x_2}{r_{2m}^{3/4}}\right)\right] \end{aligned} \tag{4.14}$$

$W_x$ and $W_h$ are the horizontal and vertical induced velocities, respectively. Two sets of the downburst parameters, which are shown in Table 4.1 [90], are used to calculate $W_x$ and $W_h$ for further simulations. The first set represents a moderate downburst, and the other one represents a severe downburst.

**Table 4.1** Downburst parameters

| Parameter | Moderate | Severe | Unit |
|---|---|---|---|
| $\Gamma_1$ | 200,000 | 400,000 | $ft^2/s$ |
| $R_1$ | 5,500 | 5,000 | $ft$ |
| $H_1$ | 2,000 | 2000 | $ft$ |
| $R_{c1}$ | 500 | 500 | $ft$ |
| $\Gamma_2$ | 120,000 | 280,000 | $ft^2/s$ |
| $R_2$ | 4,000 | 3,500 | $ft$ |
| $H_2$ | 2,500 | 2000 | $ft$ |
| $R_{c2}$ | 500 | 300 | $ft$ |

It is assumed that the aircraft encounters the downburst at $h = 800\,ft$. Since we have all the parameters needed, the moderate and severe downbursts can be illustrated as in Figure 4.9a and Figure 4.9b.

The windshear effect, which is mathematically represented above, has to be taken into consideration to approximate a flight simulation to a real flight. Thus, it has to be embedded into the aircraft dynamics. The equations of motion can be written as follows:

$$\begin{aligned} \dot{x} &= V_T\cos\gamma_a + W_x \\ \dot{h} &= V_T\sin\gamma_a + W_h \\ \dot{V}_T &= \frac{1}{m}\left[T\cos(\alpha+i) - D - mg\sin\gamma_a - m\dot{W}_x\cos\gamma_a - m\dot{W}_h sin\gamma_a\right] \\ \dot{\gamma}_a &= \frac{1}{mV_T}\left[T\sin(\alpha+i) + L - mg\cos\gamma_a + m\dot{W}_x\sin\gamma_a - m\dot{W}_h\cos\gamma_a\right] \end{aligned} \tag{4.15}$$

where $V_T$ is the aircraft true airspeed; $m$ is the aircraft mass; $\gamma_a$ is the flight path angle; $\alpha$ is the angle of attack; $i$ is the thrust inclination angle; $T, D$, and $L$ are the thrust, drag, and lift, respectively.

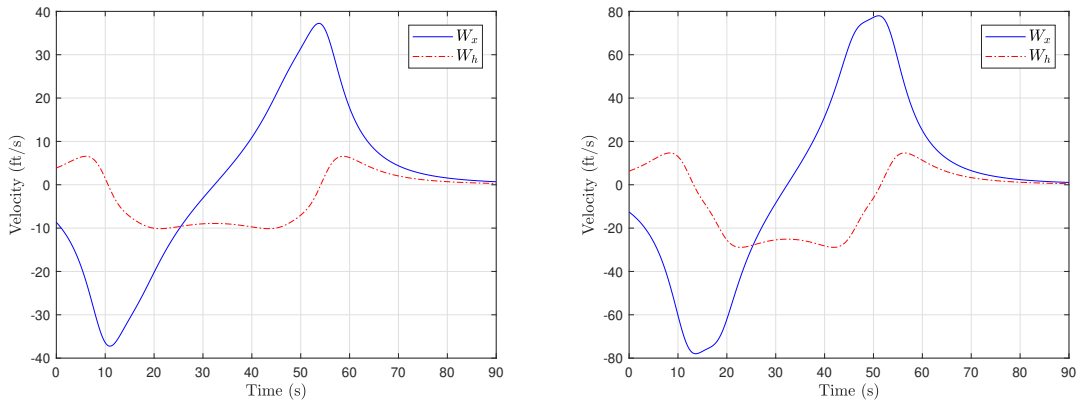


**(a)** Moderate Downburst **(b)** Severe Downburst

**Figure 4.9** Windshear effect

## 4.5 Turbulence Model

The aircraft are exposed to the environmental disturbances during their flights, such as wind or wind gusts caused by the movement of the atmospheric air masses. The velocity field within the atmosphere varies in both space and time. This field can be decoupled into a mean part and fluctuating part. The fluctuating part is called as atmospheric turbulence or wind gust [94]. Both the disturbances affect the stability of the aircraft. Scientists developed statistical models since the atmospheric turbulence is a random phenomenon.

Von Karman and Dryden developed two different spectral forms of the random continuous turbulence which are used to model atmospheric turbulence. In this thesis, the Dryden model is used for the lateral simulations. Since the lateral motion is considered, the Dryden model [94] for the lateral component is given by

$$H_v(s) = \sigma_v \sqrt{\frac{S_l}{\pi V_T}} \frac{1 + \frac{\sqrt{3}S_l}{V_T} s}{(1 + \frac{S_l}{V_T} s)^2} \tag{4.16}$$

where $\sigma_v$ represents the turbulence intensity, $S_l$ represents the turbulence scale length, $V_T$ represents the trim velocity of the aircraft.

Table 4.2 [94] shows the Dryden gust model parameters for various altitudes and turbulence conditions. For medium altitude and light turbulence according to our

trim conditions, Equation (4.16) becomes

$$H_v(s) = 1.817\left(\frac{s+0.0825}{s^2+0.286s+0.0204}\right) \tag{4.17}$$

For medium altitude and moderate turbulence according to our trim conditions, Equation (4.16) becomes

$$H_v(s) = 3.634\left(\frac{s+0.0825}{s^2+0.286s+0.0204}\right) \tag{4.18}$$

**Table 4.2** Dryden gust model parameters

| Gust Description | Altitude (ft) | $S_l(ft)$ | $\sigma_v(ft/s)$ |
|---|---|---|---|
| Low Altitude, Light Turbulence | 164 | 656 | 3.48 |
| Low Altitude, Moderate Turbulence | 164 | 656 | 6.95 |
| Medium Altitude, Light Turbulence | 1968 | 1748 | 4.92 |
| Medium Altitude, Moderate Turbulence | 1968 | 1748 | 9.84 |

The light and moderate turbulence models are illustrated in Figure 4.10.

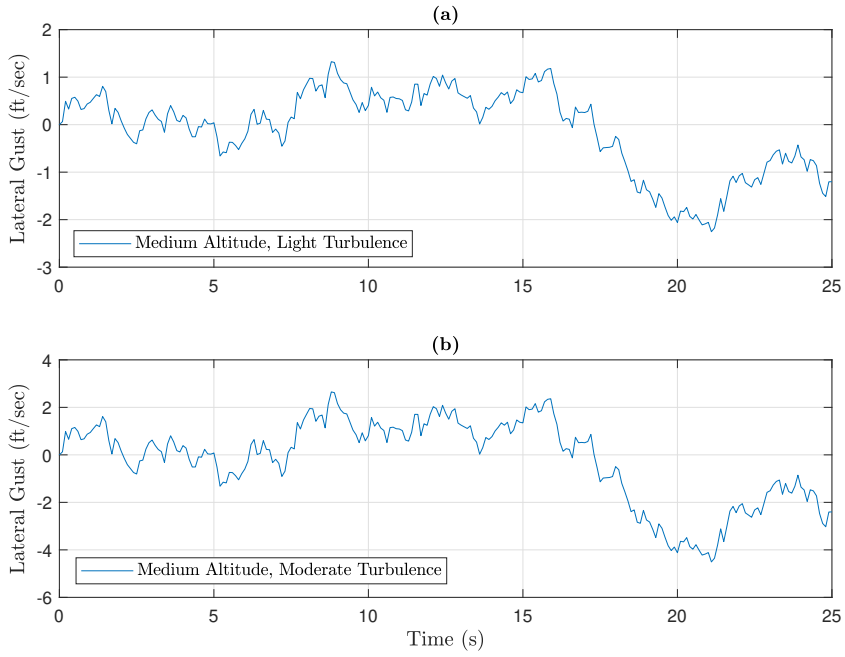


**Figure 4.10** Illustration of Dryden gust model for (a) Medium altitude and light turbulence (b) Medium altitude and moderate turbulence

# 5
# LONGITUDINAL MOTION

## 5.1 Introduction

In this section, we mainly focus on the flare phase, which is the most challenging phase during a flight. The Automatic Landing System (ALS) works in harmony with the Instrumental Landing System (ILS) that is located at the airport. The aircraft is guided by the ILS to prepare for landing. The ILS consists of two different beam transmitters. One of them is for the glideslope, and the other one is for the localizer. The aircraft aligns and localizes itself to a suitable altitude level, and approach angle owing to these transmitters and starts decreasing its altitude [12].

## 5.2 The Aircraft Longitudinal Model

The fixed-wing aircraft have 6-DOF equation of motion model. This model can be decoupled into "Longitudinal" and "Lateral" motion because they slightly affect each other as discussed in more detail in Chapter 2. In this section, only the longitudinal motion will be considered since the flare phase of a flight is mostly related to the longitudinal part. The longitudinal equations of motion are given as follows:

$$\begin{aligned}
\dot{V}_T &= \frac{1}{m}\big[T\cos(\alpha+i) - D - mg\sin\gamma_a\big] \\
\dot{\gamma}_a &= \frac{1}{mV_T}\big[T\sin(\alpha+i) + L - mg\cos\gamma_a\big] \\
\dot{q} &= \frac{\widetilde{M}}{I_{yy}} \\
\dot{\theta} &= q
\end{aligned} \tag{5.1}$$

where $V_T$ is the aircraft true airspeed; $m$ is the aircraft mass; $\gamma_a$ is the flight path angle; $q$ is the pitch rate; $\theta$ is the pitch angle; $\alpha$ is the angle of attack; $i$ is the

thrust inclination angle; $\widetilde{M}$ is the pitching moment; $I_{yy}$ is the principal moment of inertia in pitch axis; $T, D$, and $L$ are the thrust, drag and lift, respectively. Note that the longitudinal motion dynamics in Equation (5.1) are expressed in polar format for convenience. The aerodynamic forces in Equation (5.1) are given by

$$\begin{aligned} L &= \frac{1}{2}\rho V^2 S C_L \qquad & D &= \frac{1}{2}\rho V^2 S C_D \\ M &= \frac{1}{2}\rho V^2 S \bar{c} C_M \qquad & T &= (A_0 + V A_1)\delta_t \end{aligned} \tag{5.2}$$

Total aerodynamic coefficients can be expressed as

$$\begin{aligned} C_L &= C_{L_O} + C_{L_\alpha}\alpha \\ C_D &= C_{D_O} + K {C_L}^2 \\ C_M &= C_{M_O} + C_{M_\alpha}\alpha + C_{M_{\delta_e}}\delta_e + C_{M_q} q \end{aligned} \tag{5.3}$$

In this section, a medium-size transport aircraft are used for the analysis and simulations. The corresponding parameters and coefficients [61] belong to this aircraft model are given in Table 5.1. A piece of code is written to trim and linearize the nonlinear equations in (5.1) according to the described values in Table 5.1. These equations are trimmed for the conditions of $V_T = 250\, ft/s$, $h = 750\, ft$, and $\gamma_a = -2.5°$, where $V_T$ is the trim velocity, and $h$ is the aircraft altitude. Then, they are linearized by using the trim values obtained. The linearized state equations can be written as follows [61]:

$$\begin{bmatrix} \dot{V}_T \\ \dot{\alpha} \\ \dot{\theta} \\ \dot{q} \\ \dot{h} \\ \dot{x} \end{bmatrix} = \begin{bmatrix} \\ \\ \\ \mathrm{A} \\ \\ \\ \\ \end{bmatrix} \begin{bmatrix} V_T \\ \alpha \\ \theta \\ q \\ h \\ x \end{bmatrix} + \begin{bmatrix} \\ \\ \\ \mathrm{B} \\ \\ \\ \\ \end{bmatrix} \begin{bmatrix} \delta_t \\ \delta_e \end{bmatrix} \tag{5.4}$$

$$A = 10^{-3} \begin{bmatrix} -38.5 & 18984 & -32139 & 0 & .1325 & 0 \\ -1.02 & -632.53 & 5.61 & 1000 & .00376 & 0 \\ 0 & 0 & 0 & 1000 & 0 & 0 \\ .0785 & -759.05 & .793 & -518.3 & -.00031 & 0 \\ -43.6 & -249760 & 249760 & 0 & 0 & 0 \\ 999 & -10905 & 10905 & 0 & 0 & 0 \end{bmatrix}$$

$$B = \begin{bmatrix} 10.1 & 0 \\ 15.445 \times 10^{-5} & 0 \\ 0 & 0 \\ 0.024656 & -0.01077 \\ 0 & 0 \\ 0 & 0 \end{bmatrix}$$

The code for the trim and linearization of the transport aircraft is given in Appendix B. In equation (5.1), there were four states; however, the states can be expanded to include $\alpha$ - AoA, $h$ - altitude, $x$ - horizontal distance as shown in Equation (5.4).

$$\dot{\alpha} = \dot{\theta} - \dot{\gamma}_a \qquad \dot{h} = V_T \sin\gamma_a \qquad \dot{x} = V_T \cos\gamma_a$$

We will handle the two control inputs, which are $\delta_t$ and $\delta_e$. $\delta_t$ represents the throttle position changing between the limits of zero to one. $\delta_e$ represents the elevator deflection angle changing between the limits of $-25^\circ$ to $25^\circ$. We will also need an acceleration equation at the z-axis to interpret the situation when the tire of the aircraft touches the ground. Body acceleration of the aircraft center of gravity ($cg$) along the $z$-axis can be written as

$$a_z = V_T \dot{\gamma}_a = V_T(q - \dot{\alpha}) \tag{5.5}$$

## 5.3 Obtaining the Generalized Plant P

All the models and methods used in this section have been defined so far. Simulations are conducted for two different cases that use these models and methods. In the first case, a simple design without any exogenous inputs other than a reference input is handled. The simulation results are compared with the design having the same parameters but utilizing a different method, described in [61]. In the second case, the windshear effect is taken into consideration as a disturbance in order to demonstrate the disturbance rejection property and the ease of adaptation of this design methodology for new additional inputs and outputs.

**Table 5.1** Medium-size transport aircraft parameters

| Parameter | Value | Unit | Description |
|---|---|---|---|
| $m$ | 162,000 | $lb$ | Mass |
| $S$ | 2,170 | $ft^2$ | Wing Reference Area |
| $b$ | 140 | $ft$ | Wing Span |
| $l$ | 90 | $ft$ | Length |
| $\bar{c}$ | 17.5 | $ft$ | Mean Aerodynamic Chord |
| $\rho$ | 0.00232 | $slug/ft^3$ | Air Density |
| $I_{yy}$ | $41 \times 10^6$ | $slug ft^2$ | Pitch Axis Inertia |
| $g$ | 32.17 | $ft/s^2$ | Gravitational Acceleration |
| $C_{D_O}$ | 0.08 | | Parasite Drag Coefficient |
| $C_{L_O}$ | 1 | | Lift Coefficient at zero Angle of Attack |
| $C_{L_\alpha}$ | 4.87 | $1/rad$ | Lift-Curve Slope |
| $C_{M_O}$ | -0.2 | | Pitching Moment Coefficient at zero Angle of Attack |
| $C_{M_\alpha}$ | -1.26 | $1/rad$ | Pitch Stiffness Derivative |
| $C_{M_{\delta_e}}$ | -0.916 | $1/rad$ | Elevator Control Power |
| $C_{M_q}$ | -16 | $1/rad$ | Pitch Damping Derivative |
| $C_{M_{\dot{\alpha}}}$ | -6 | $1/rad$ | Acceleration Derivative for Moment |
| $C_{L_{\dot{\alpha}}}$ | 0 | $1/rad$ | Acceleration Derivative for Lift |
| $A_0$ | $60 \times 10^6$ | $lb$ | Static Thrust from Two Engines |
| $A_1$ | -38 | $lb/(ft/s)$ | Thrust for each $ft/s$ |
| $K$ | 0.042 | | Constant |

### 5.3.1 Case 1:

The basic configuration of the system is shown in Figure 5.1a. In the system, the "Ideal Model" and "Aircraft Model" are defined in Sections 4.3 and 5.2, respectively. There is only reference input r as an exogenous input. The main purpose here is to ensure that the altitude of the aircraft follows the ideal model closely. The exogenous outputs, $z_1$ and $z_2$, are used to achieve this constraint. In this case, $z_1$ is the altitude error signal to be minimized between the aircraft altitude and the desired altitude, and $z_2$ is used to decrease the amplitude of the control signal to an achievable level in terms of the elevator deflection angle. For instance, the elevator deflection angle has to be kept within its limits, which are ±25° in this case, and $W_u$ is the weighting function used for this purpose. The best $W_u$ can be found after a couple of simulation experiments and selected as a constant number ($W_u = 6$) for this simulation scenario. $M(s)$ and $L(s)$ are the dynamic controllers. Elevator-Actuator is modelled as a first-order transfer function with a time constant of $0.1s$.

The generalized plant P is obtained from Figure 5.1a. If $M(s)$ and $L(s)$ are kept outside as in Figure 3.4, the generalized plant P structure becomes as in Figure 5.1b.

After the generalized matrix P is obtained, the controller K is constructed by solving the LMIs, as described in Section 3.4. The dynamic controller matrices obtained are given as follows:

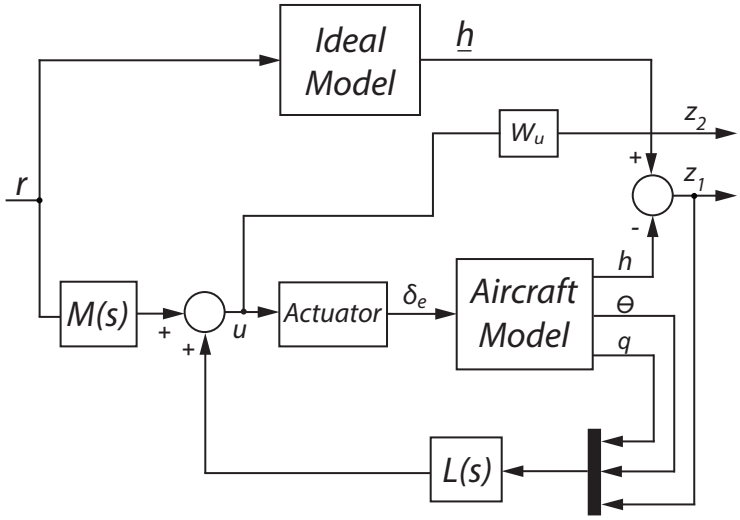


**(a)** System block diagram

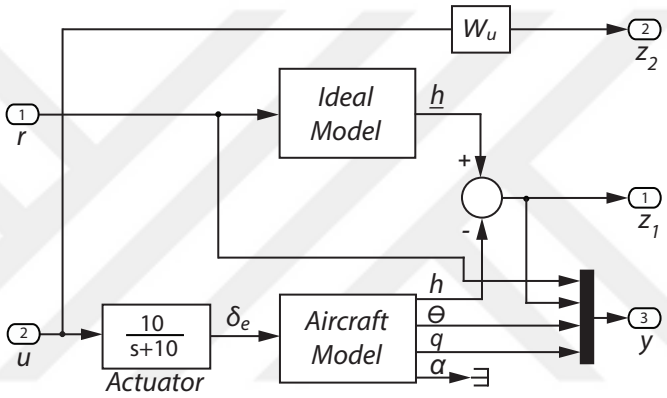


**(b)** Generalized plant P

**Figure 5.1** Case 1- Block diagrams

$$A_K = 10^8 \times \begin{bmatrix} -0.02 & 0.00 & 0.00 & 0.00 & -0.01 & -0.10 \\ -21.56 & 0.22 & 0.14 & -0.92 & -4.71 & -86.74 \\ 34.63 & -0.35 & -0.22 & 1.49 & 7.57 & 139.36 \\ 11.47 & -0.12 & -0.07 & 0.49 & 2.51 & 46.14 \\ 0.05 & 0.00 & 0.00 & 0.00 & 0.01 & 0.21 \\ -0.12 & 0.00 & 0.00 & -0.01 & -0.03 & -0.48 \end{bmatrix}$$

$$B_K = 10^6 \times \begin{bmatrix} 0.00 & 0.35 & 0.00 & 0.00 \\ -0.06 & 307.91 & -0.19 & -0.03 \\ 0.10 & -494.68 & 0.31 & 0.05 \\ 0.03 & -163.82 & 0.10 & 0.02 \\ 0.00 & -0.75 & 0.00 & 0.00 \\ 0.00 & 1.69 & 0.00 & 0.00 \end{bmatrix} \tag{5.6}$$

$$C_K = \begin{bmatrix} 0.0003 & -0.0002 & -0.0001 & 0.0014 & -0.0002 & 0.0645 \end{bmatrix}$$
$$D_K = \begin{bmatrix} -1.00 & 0.00 & 0.00 & 0.00 \end{bmatrix}$$

The dynamic controller for this case is a sixth-order controller. If the state-space representation of the controller split up as in Figure 5.1a, M(s) and L(s) are obtained as

$$\begin{aligned} M(s) &= \frac{u}{r} = \frac{M_n(s)}{D(s)} \quad L_1(s) = \frac{u}{z_1} = \frac{L_{1_n}(s)}{D(s)} \\ L_2(s) &= \frac{u}{\theta} = \frac{L_{2_n}(s)}{D(s)} \quad L_3(s) = \frac{u}{q} = \frac{L_{3_n}(s)}{D(s)} \end{aligned} \tag{5.7}$$

where

$$\begin{aligned} M_n(s) =& -s^6 - 10.38s^5 + 1.925 \times 10^4 s^4 + 2.493 \times 10^5 s^3 \\ &+ 6.61 \times 10^5 s^2 + 9.334 \times 10^5 s + 1.736 \times 10^5 \\ L_{1_n}(s) =& -4.624 \times 10^{-5} s^6 - 9.93 \times 10^4 s^5 - 1.166 \times 10^6 s^4 \\ &- 2.55 \times 10^6 s^3 - 8.744 \times 10^6 s^2 - 6.051 \times 10^6 s \\ &- 1.088 \times 10^6 \\ L_{2_n}(s) =& -1.167 \times 10^{-9} s^6 + 63.22s^5 + 821.8s^4 \\ &+ 8.279 \times 10^5 s^3 + 1.013 \times 10^7 s^2 + 1.92 \times 10^7 s \\ &+ 4.872 \times 10^6 \\ L_{3_n}(s) =& 1.791 \times 10^{-9} s^6 + 9.216s^5 + 140.5s^4 \\ &- 3.464 \times 10^4 s^3 + 4.011 \times 10^5 s^2 + 7.761 \times 10^6 s \\ &+ 2.291 \times 10^6 \\ D(s) =& s^6 + 30.53s^5 + 8.032 \times 10^4 s^4 + 1.148 \times 10^6 s^3 \\ &+ 4.601 \times 10^6 s^2 + 1.293 \times 10^7 s + 3.494 \times 10^6 \end{aligned} \tag{5.8}$$

The generalized P-K configuration of the overall system with the controller in the s-domain is shown in Figure 5.2.

### 5.3.2 Case 2:

In this case, the windshear effect is taken into consideration as a disturbance ($d$). The block diagram of the overall system is shown in Figure 5.3a. It is assumed that the windshear effect starts in the middle of the glideslope phase and continues even in the flare phase. The windshear components, which are more explicitly shown in

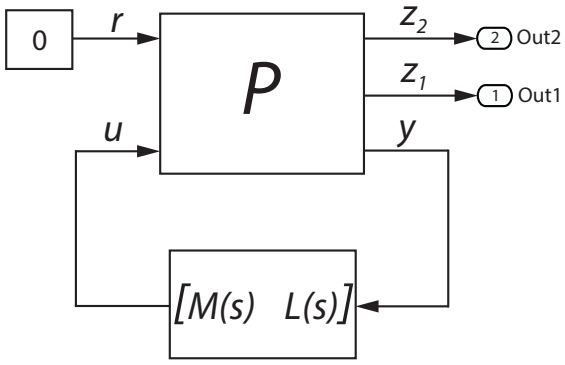


**Figure 5.2** Generalized P-K form for Case 1

Figure 5.3b, are added to the generalized plant P as disturbances ($d$). The throttle control is also added to the system to compensate for the windshear effect. Actuator of the throttle is modelled as a first-order transfer function with a time constant of 5 $s$. For keeping the elevator deflection and the throttle control within their limits, the control inputs are defined as outputs ($z_2$ and $z_4$) with some weighting elements $W_e$ and $W_t$, which are constant numbers 1 and 0.5, respectively. $z_1$ and $z_3$ are the altitude and airspeed error signals to be minimized. A new dynamic controller is obtained by solving the LMIs in (3.44) and (3.45) for the new generalized plant P. The resulting controller is an eighth-order controller. Thus the new P-K configuration, including the windshear, is formed according to the new generalized plant P, as shown in Figure 5.4.

$$A_K = 10^8 \times \begin{bmatrix} -0.02 & 0.00 & 0.00 & 0.00 & 0.00 & 0.01 & 0.00 & 0.17 \\ 0.00 & 0.00 & 0.00 & 0.00 & 0.00 & 0.00 & 0.00 & -0.04 \\ -6.82 & -0.02 & -0.06 & -0.06 & 0.83 & -4.71 & 0.07 & 73.93 \\ 10.40 & 0.04 & 0.09 & 0.10 & -1.27 & 7.19 & -0.11 & -112.76 \\ 1.93 & 0.01 & 0.02 & 0.02 & -0.24 & 1.33 & -0.02 & -20.91 \\ 0.03 & 0.00 & 0.00 & 0.00 & 0.00 & 0.02 & 0.00 & -0.28 \\ 0.01 & 0.00 & 0.00 & 0.00 & 0.00 & 0.00 & 0.00 & -0.06 \\ -0.02 & 0.00 & 0.00 & 0.00 & 0.00 & -0.01 & 0.00 & 0.20 \end{bmatrix}$$

$$B_K = 10^5 \times \begin{bmatrix} 0.00 & 0.00 & 0.56 & -0.02 & -0.02 \\ 0.00 & 0.00 & -0.13 & 0.01 & 0.01 \\ 0.30 & -0.07 & 238.37 & -10.33 & -9.66 \\ -0.45 & 0.10 & -363.57 & 15.76 & 14.74 \\ -0.08 & 0.02 & -67.40 & 2.92 & 2.73 \\ 0.00 & 0.00 & -0.90 & 0.04 & 0.04 \\ 0.00 & 0.00 & -0.20 & 0.01 & 0.01 \\ 0.00 & 0.00 & 0.63 & -0.03 & -0.03 \end{bmatrix} \tag{5.9}$$

$$C_K = \begin{bmatrix} 3.16 & -3.62 & -0.02 & -0.02 & 0.18 & 2.92 & -0.45 & 16.18 \\ 0.02 & -0.01 & -0.01 & -0.01 & 0.06 & 0.01 & -0.01 & 2.43 \end{bmatrix}$$

$$D_K = \begin{bmatrix} -1.0002 & 0.00 & 0.0003 & 0.00 & 0.00 \\ -0.0001 & -1.00 & -0.0004 & 0.00 & 0.00 \end{bmatrix}$$

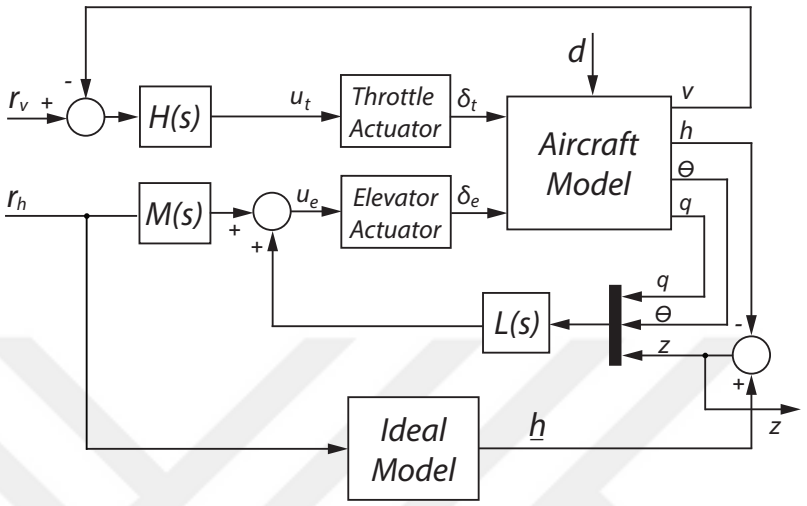


**(a)** System block diagram

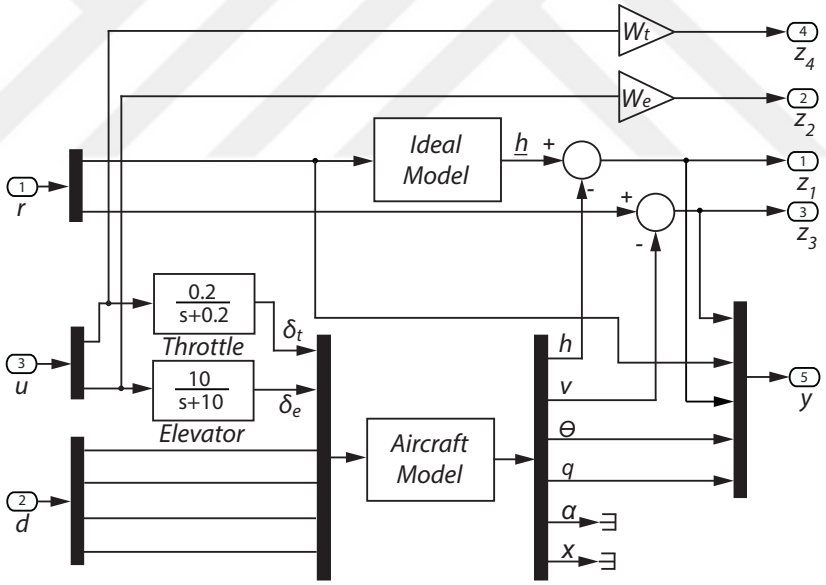


**(b)** Generalized plant P

**Figure 5.3** Case 2 - Block diagrams

We expect that the synthesized controller should improve the $H_\infty$ norm of the closed-loop system. The $H_\infty$ norm comparisons of the open-loop versus closed-loop behaviours for both the Case 1 and Case 2 are shown in Table 5.2. $H_\infty$ norms of the open-loop systems are infinity, which means that the systems are unstable. However, the synthesized $H_\infty$ controllers make the systems stable as well as generate great improvement on $H_\infty$ norm.

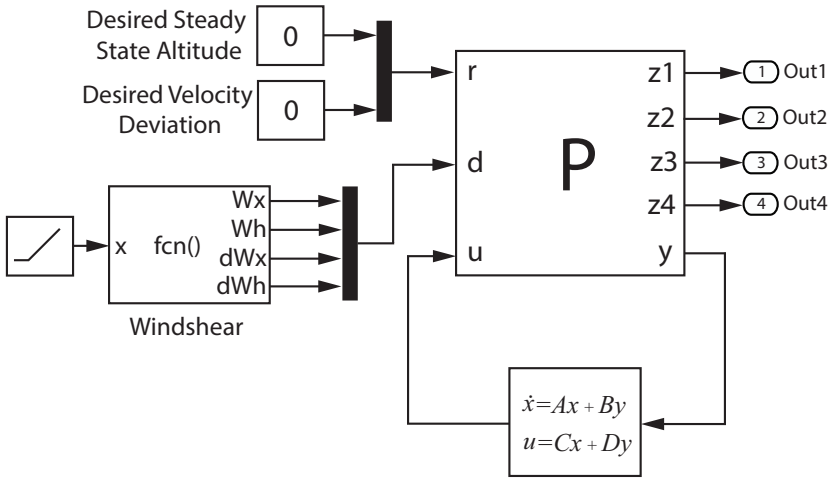


**Figure 5.4** P-K configuration with windshear

**Table 5.2** $H_\infty$ norm comparison

| | $H_\infty$ **Norm** | |
|---|---|---|
| **Type** | **Case1** | **Case 2** |
| Open-Loop | $\infty$ | $5.045 \times 10^5$ |
| Closed-Loop | 2.11 | 2.4131 |

## 5.4 Simulation Results

### 5.4.1 Case 1:

It is assumed that the glideslope phase is just ended at the altitude level of 36.37 *ft*, and the flare phase has just started at the same altitude. The P-K configuration was previously shown in Figure 5.2. K is the sixth-order controller obtained in Section 5.3 - Case 1. P is the block diagram already shown in Figure 5.1b. There is only one exogenous input of $r$, which is a steady-state altitude level. In this case, it has to be zero since the landing phase is considered.

In Figure 5.5a, the "Actual Path" and "Reference Path" are compared. For this study, we also compare our results with the study in [61], where LQR based controller design method is used. It is clearly seen that when compared with the LQR method in [61], the actual path follows the reference path more closely and smoothly using the combination of the $H_\infty$ and model following methods. Based on this result, it is also expected that the flight path angle and elevator deflection angle have to be smoother. The flight path angle $\gamma_a$ and elevator deflection angle $\delta_e$ are shown in Figure 5.5b. $\gamma_a$ starts with $-2.5°$ initial condition, which is the flight path angle of the glide slope phase and goes to zero as the aircraft approaches the touchdown point. During landing, the elevator deflection angle stays within limits. As seen from Figure 5.5b, when compared with [61], the transient behaviors of $\gamma_a$ and $\delta_e$ are smoother as expected.

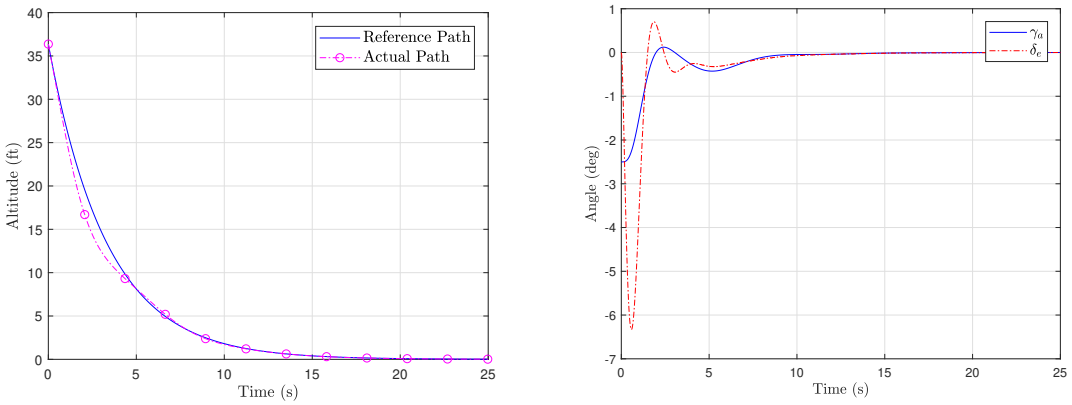


**(a)** Altitude level flare phase **(b)** Elevator deflection and gamma

**Figure 5.5** Case1 - No wind effect

### 5.4.2 Case 2:

For examination of the effect of the windshear, it is assumed that the aircraft is still on the glideslope phase, and its altitude level is 800 *ft*. The flare phase starts at the altitude level of 36.37 *ft*. The desired touch down point beyond the glideslope transmitter point ($D$) is 2,500 *ft*. In ideal conditions, the distance the aircraft should take until the glideslope transmitter point is calculated as $x = 800 \div \tan 2.5° = 18,323$ *ft*. The total distance the aircraft should take is $x = 18,323 + 2,500 = 20,823$ *ft*.

The comparison of the altitude behaviors between the ideal model and actual aircraft in the moderate downburst environment is shown in Figure 5.6a. The aircraft encounters an increasing headwind through the first ten seconds, as shown in Figure 4.9a. The horizontal component of the windshear increases the airspeed of the aircraft, and its vertical component increases the angle of attack. Therefore, an increase in gamma occurs. As a result, the altitude of the aircraft starts increasing. On the other hand, the controller starts compensating the altitude and velocity errors by manipulating the elevator and throttle controls. Even if the intervention of the controller initially reduces the altitude and angle of attack, the altitude gets back on the desired level with a little increase in the airspeed and angle of attack. After ten seconds, the headwind loses its effect, and the downdraft starts being effective. The angle of attack decreases to keep the altitude of the aircraft on the track as expected. The aircraft starts encountering an increasing tailwind after about thirty-three seconds. As the tailwind gets close to the maximum level, the angle of attack starts decreasing, but the controller retakes the control. Then, the airspeed decreases, and the angle of attack gets increased by manipulating the elevator and throttle controls. Thus, a small increase occurs at the altitude level. The flare phase starts when the tailwind starts losing its effect. As seen in Figure 5.6a, the aircraft

continues to follow the ideal model very closely during both the glideslope and flare phases. Therefore, it closely lands to the calculated touchdown point smoothly, as shown in Figure 5.6c. Figure 5.6b visualizes the altitude error between the actual and reference models. The rest of the aircraft behaviours mentioned above in the moderate downburst environment are illustrated in Figure 5.6d, 5.6e, 5.6f, 5.6g. Note that the velocity deviation from the trim velocity of 250 $ft/s$ is plotted in Figure 5.6d. It is worth noting that, during the glideslope phase, contrary to the conventional landing systems, it is not necessary to keep the flight path angle ($\gamma_a$) constant. A reference model was defined for both the glideslope and the flare phases, and it is expected from the controller that it enables the aircraft to follow (in the longitudinal direction) the reference model by utilizing throttle and elevator control surfaces. Dynamic equations, including the windshear components for the aircraft, were introduced in Equation (4.15). As seen from the equation, the altitude depends on $V_T$, $\gamma_a$, and $W_h$. $W_h$ is a disturbance input as the windshear component, and cannot be controlled. However, $\gamma_a$ and $V_T$ can be used by the controller to compensate for the windshear effects and to guide the aircraft on the desired flight path. Providing that the aircraft's velocity is constant, the AoA ($\alpha$) depends on the wind (i.e., turbulence level) if the atmosphere is not still. As seen in Equation (4.15), $\gamma_a$ also depends on the windshear components, $V_T$ and $\theta$ ($\gamma_a = \theta - \alpha$). Thus, the controller dynamically makes fine adjustments to keep the aircraft in the desired path by controlling variables $V_T$, $\theta$, and hence $\gamma_a$ by taking the windshear components into account. This dependence can be seen in Figure 5.6e. Figure 5.6f and 5.6g depict, correspondingly, the elevator and throttle actuator displacements, which remain within limits, as the aircraft follows the reference landing trajectory. Body acceleration at the Aircraft's $cg$ (along the $z$-axis) is shown in 5.6h. The acceleration on the $z$-axis looks very close to zero near the touchdown point, which means that the aircraft's tires smoothly touch the ground.

P-K configuration is also tested for a severe downburst environment. Similar attitudes are obtained, but the magnitudes are greater, as shown in Figure 5.7a, 5.7b, 5.7c, 5.7d, 5.7e, 5.7f, 5.7g, 5.7h. The altitude returns to the reference path after the maximum headwind, but it goes a little down and stays there through downdraft. On the other hand, although the tailwind is being slightly effective during the flare phase, the aircraft follows the ideal model very closely. The elevator deflection angle and the throttle position do not exceed the limits.

The proposed method is also compared with the study in [61] for the windshear effect. For this comparison, the system in [61] is modified to have the windshear components. It is assumed that the aircraft is under the severe downburst effect, as shown in Figure 4.9b. A feedback loop is also added to the system for the throttle control. Thus, the system is as similar to ours as possible. In Figure 5.8a, the "Actual Path" and

"Reference Path" are compared. At first glance, the "Actual Path" always fluctuates around the "Reference Path". It seems that the controller has a hard time keeping the state around the "Reference Path". The divergence between the "Actual Path" and "Reference Path" sometimes gets higher values when compared with Figure 5.7a. In the flare phase, the "Actual Path" does not follow the "Reference Path", and the aircraft has hard landing on the ground. This landing may be called a crush. In Figure 5.8b, it is seen that the aircraft lands little before the calculated touchdown point. As a result, it is obvious that the proposed method provides a more stabilized, more accurate, and smoother landing.

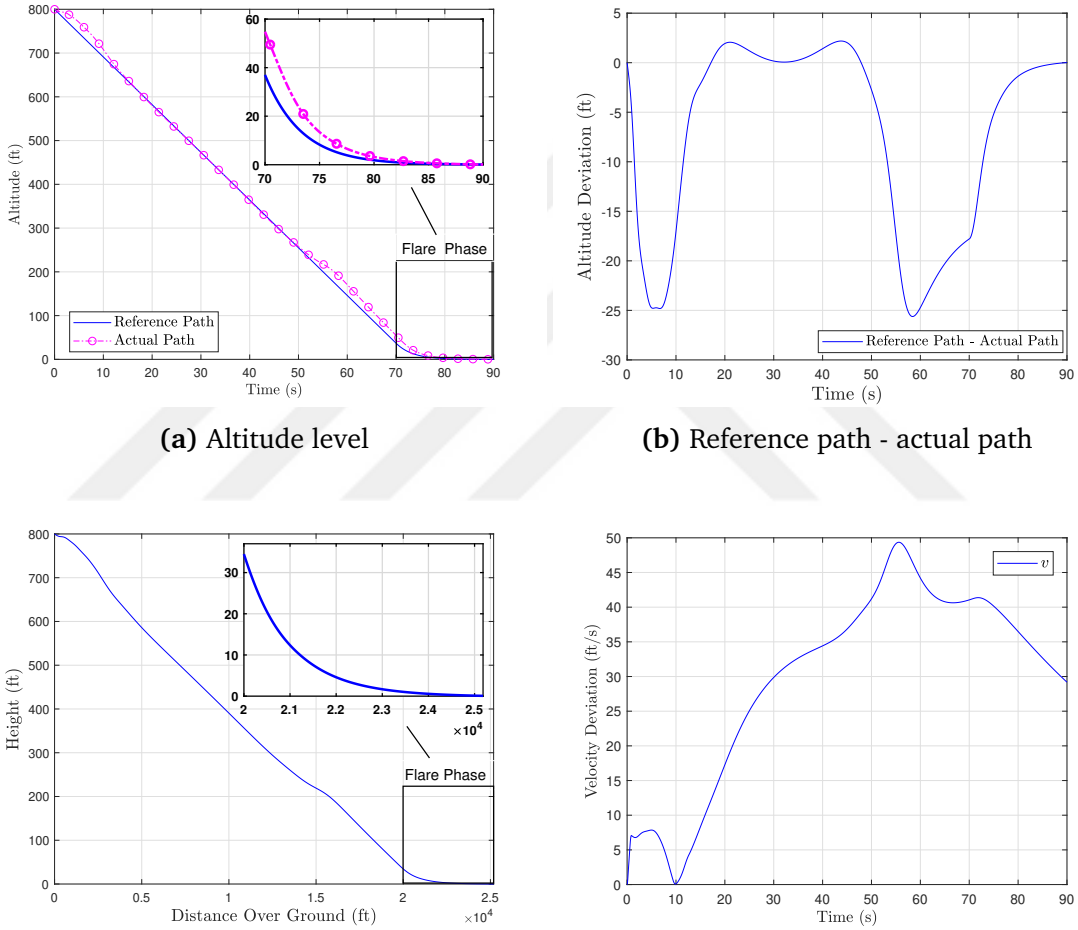


**(a)** Altitude level

**(b)** Reference path - actual path

**(c)** Height versus ground distance

**(d)** Velocity deviation from trim velocity

**Figure 5.6** Case 2 - Moderate downburst

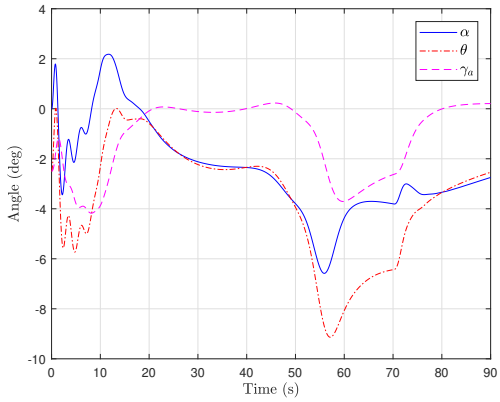


**(e)** AoA, pitch and gamma angles of aircraft

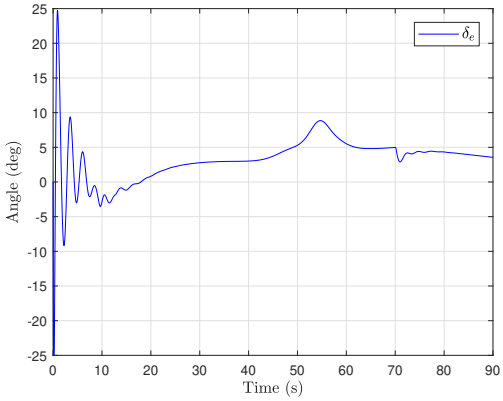


**(f)** Elevator deflection

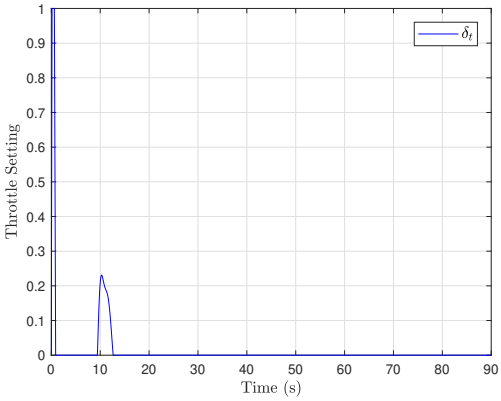


**(g)** Throttle setting

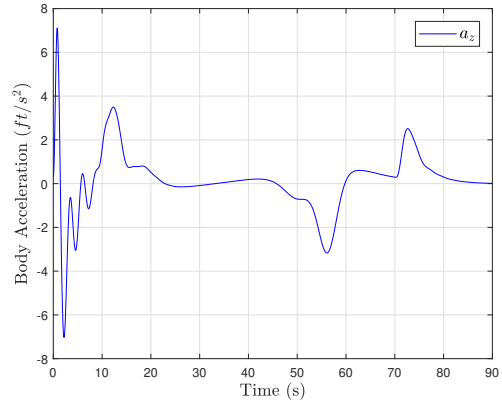


**(h)** Body acceleration

**Figure 5.6** Case 2 - Moderate downburst (Cont'd)

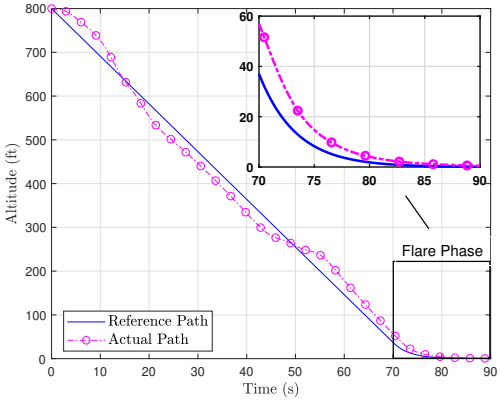


**(a)** Altitude level

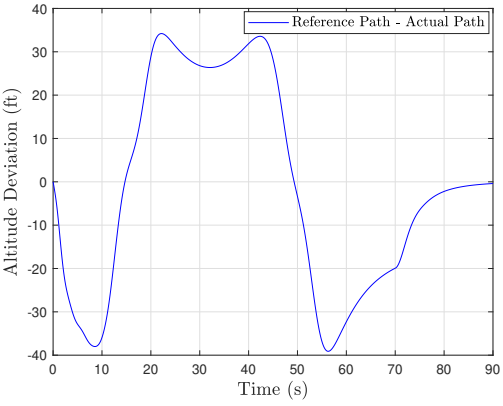


**(b)** Reference path - actual path

**Figure 5.7** Case 2 - Severe downburst

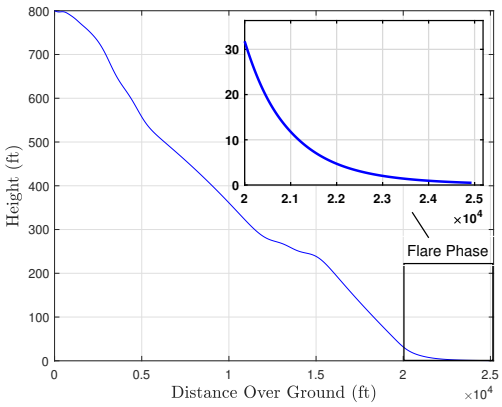


**(c)** Height versus ground distance

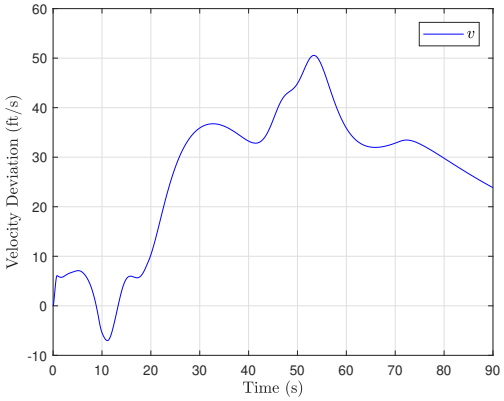


**(d)** Velocity deviation from trim velocity

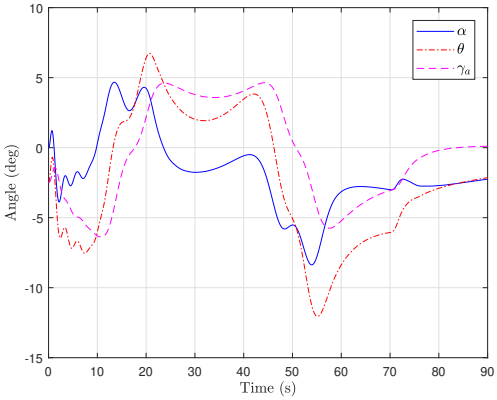


**(e)** AoA, pitch and gamma angles of aircraft

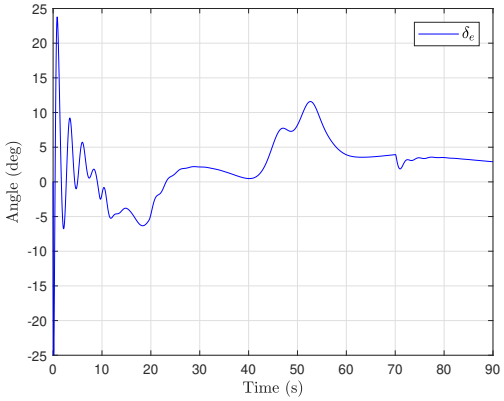


**(f)** Elevator deflection

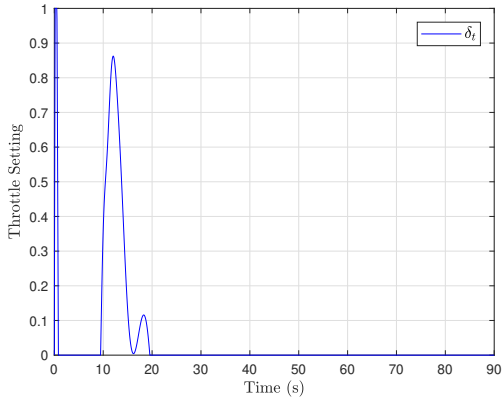


**(g)** Throttle setting

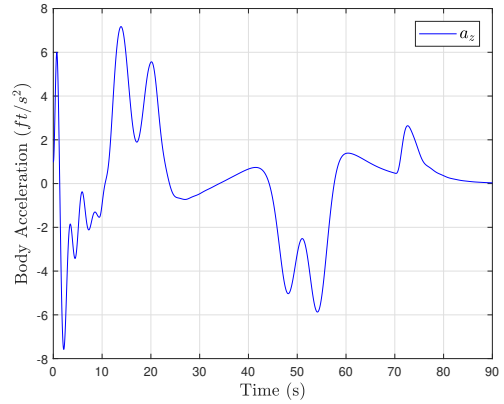


**(h)** Body acceleration

**Figure 5.7** Case 2 - Severe downburst (Cont'd)

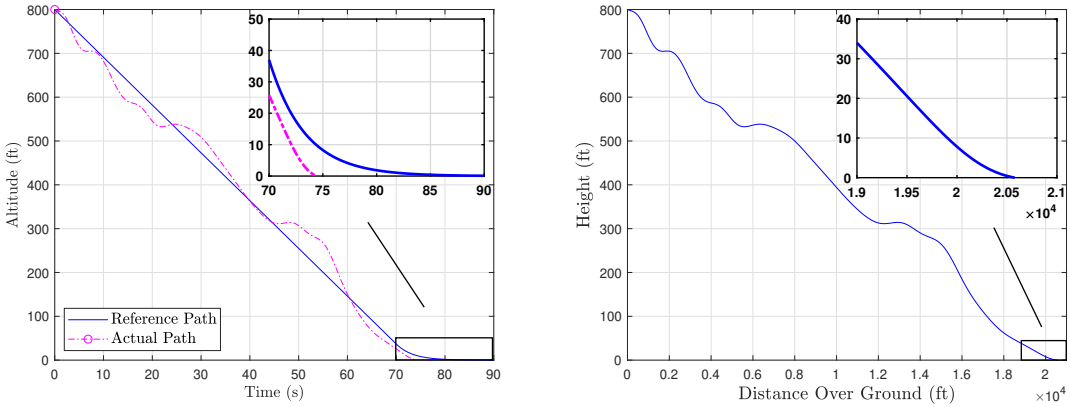


**(a)** Altitude level **(b)** Height versus ground distance

**Figure 5.8** Lqr control method under severe downburst

# 6
# LATERAL MOTION

## 6.1 Introduction

In this section, it is focused on the final approach phase. The aircraft has to be aligned to the center of the runway before starting the glideslope phase. There needs to be an automatic guidance system to position and keep the aircraft on the center-line of the runway. VOR (Very High-Frequency Omni-Directional Range) system, which is one of the most popular and effective systems, is considered and working together with DME (Distance Measuring Equipment) to guide the aircraft to the desired position laterally. The aircraft calculates both its deviation from the center of the runway and its distance from the touchdown point, thanks to the VOR and DME systems. Therefore, it keeps itself aligned throughout the landing. This deviation is called the aircraft offset angle and is the main subject of the Automatic Landing System for the final approaching phase.

## 6.2 The Aircraft Lateral Model

Lateral motion is mainly considered throughout this section, and the motion of the system is expressed in the state space form as follows:

$$\begin{bmatrix} \dot{\beta} \\ \dot{\phi} \\ \dot{p} \\ \dot{r} \\ \dot{\psi} \end{bmatrix} = \begin{bmatrix} \frac{\widetilde{Y}_\beta}{V_T} & \frac{g}{V_T}\cos\theta & \frac{\widetilde{Y}_p}{V_T} & -(1-\frac{\widetilde{Y}_r}{V_T}) & 0 \\ 0 & 0 & 1 & \tan\theta & 0 \\ \widetilde{L}_\beta & 0 & \widetilde{L}_p & \widetilde{L}_r & 0 \\ \widetilde{N}_\beta & 0 & \widetilde{N}_p & \widetilde{N}_r & 0 \\ 0 & 0 & 0 & 1/cos(\theta) & 0 \end{bmatrix} \begin{bmatrix} \beta \\ \phi \\ p \\ r \\ \psi \end{bmatrix} + \begin{bmatrix} \frac{\widetilde{Y}_{\delta_a}}{V_T} & \frac{\widetilde{Y}_{\delta_r}}{V_T} \\ 0 & 0 \\ \widetilde{L}_{\delta_a} & \widetilde{L}_{\delta_r} \\ \widetilde{N}_{\delta_a} & \widetilde{N}_{\delta_r} \\ 0 & 0 \end{bmatrix} \begin{bmatrix} \delta_a \\ \delta_r \end{bmatrix} \tag{6.1}$$

where $\beta$ is the sideslip angle, $\phi$ is the roll angle, $p$ is the roll rate, $r$ is the yaw rate, $\psi$ is the heading (yaw) angle, $V_T$ is the aircraft true speed, $g$ is the gravitational acceleration and $\theta$ is the pitch angle. In this paper, the F-16 aircraft model is handled as a plant, and the study given in [95] is used during the trim and linearization of that.

Table 6.1 shows the trim conditions to obtain the lateral derivatives given in Table 6.2. Then the linearized lateral motion of the system is expressed in the state space form as follows:

$$A = \begin{bmatrix} -0.1569 & 0.1265 & 0.2262 & -0.9666 & 0 \\ 0 & 0 & 1 & 0.1846 & 0 \\ -15.23 & 0 & -1.567 & 0.888 & 0 \\ 1.949 & 0 & -0.03652 & -0.2468 & 0 \\ 0 & 0 & 0 & 1.017 & 0 \end{bmatrix} \quad B = \begin{bmatrix} 0.0001438 & 0.0003925 \\ 0 & 0 \\ -0.166 & 0.03061 \\ -0.006115 & -0.01493 \\ 0 & 0 \end{bmatrix} \tag{6.2}$$

The lateral motion of an aircraft is controlled using $\delta_a$ and $\delta_r$. For F-16 model aircraft, the deflection limits for the aileron ($\delta_a$) is ±21.5° and for the rudder ($\delta_r$) is ±30°.

**Table 6.1** F16 - trimmed flight conditions

| Parameter | Value | Unit |
|---|---|---|
| $V_T$ | 250 | $ft/s$ |
| $h$ | 750 | $ft$ |
| $\alpha$ | 0.22617 | $rad$ |
| $\beta$ | 0 | $rad$ |
| $\phi$ | 0 | $rad$ |
| $\theta$ | 0.18253 | $rad$ |
| $P$ | 0 | $r/s$ |
| $Q$ | 0 | $r/s$ |
| $R$ | 0 | $r/s$ |
| *Throttle* | 0.10977 | $0-1$ |
| *Elevator* | 0.35711 | $deg$ |
| *Aileron* | 0 | $deg$ |
| *Rudder* | 0 | $deg$ |

## 6.3 Obtaining the Generalized Plant P

This section is divided into three parts for analyzing the proposed method much better way. In the first part, the conventional lateral control system is handled by using the P-K configuration and $H_\infty$ synthesis method. In the second part, the control structure for the lateral beam tracking system is developed by adding some new blocks on the first part. In the last part, the model following method is added to the overall system.

### 6.3.1 Aircraft Lateral Control

The block diagram for the general lateral feedback control system is illustrated in Figure 6.1. This is a two-input system. The inputs are called upper-input ($\delta_a$) and

**Table 6.2** F16 - lateral derivatives for trimmed conditions

| Parameter | Value | Unit | Description |
|---|---|---|---|
| $\widetilde{Y}_\beta$ | -39.225 | $ft/s^2$ | Side-force derivative due to sideslip |
| $\widetilde{Y}_p$ | 56.55 | $ft/s$ | Side-force derivative due to roll rate |
| $\widetilde{Y}_r$ | 8.35 | $ft/s$ | Side-force derivative due to yaw rate |
| $\widetilde{L}_\beta$ | -15.23 | $s^{-2}$ | Rolling moment derivative due to sideslip |
| $\widetilde{L}_p$ | -1.567 | $s^{-1}$ | Rolling moment derivative due to roll rate |
| $\widetilde{L}_r$ | 0.888 | $s^{-1}$ | Rolling moment derivative due to yaw rate |
| $\widetilde{N}_\beta$ | 1.949 | $s^{-2}$ | Yawing moment derivative due to sideslip |
| $\widetilde{N}_p$ | -0.03652 | $s^{-1}$ | Yawing moment derivative due to roll rate |
| $\widetilde{N}_r$ | -0.2468 | $s^{-1}$ | Yawing moment derivative due to yaw rate |
| $\widetilde{Y}_{\delta_a}$ | 0.03595 | $ft/s^2$ | Side-force derivative due to aileron deflection |
| $\widetilde{Y}_{\delta_r}$ | 0.098125 | $ft/s^2$ | Side-force derivative due to rudder deflection |
| $\widetilde{L}_{\delta_a}$ | -0.166 | $s^{-2}$ | Rolling moment derivative due to aileron deflection |
| $\widetilde{L}_{\delta_r}$ | 0.03061 | $s^{-2}$ | Rolling moment derivative due to rudder deflection |
| $\widetilde{N}_{\delta_a}$ | -0.006115 | $s^{-2}$ | Yawing moment derivative due to aileron deflection |
| $\widetilde{N}_{\delta_r}$ | -0.01493 | $s^{-2}$ | Yawing moment derivative due to rudder deflection |

lower-input ($\delta_r$). The lower input consists of two loops. The outer loop has a yaw rate control feedback. Any yaw rate generated during the dutch roll mode is not desired and needed to be eliminated. The yaw damper feedback is used to do that. This feedback prevents the aircraft from undesired yaw rates, but this also creates an undesired situation. In a coordinated steady-state turn, the aircraft has a constant and non-zero yaw rate. The yaw damper feedback will also work to take this desired non-zero yaw rate to zero. That is not the desired situation.

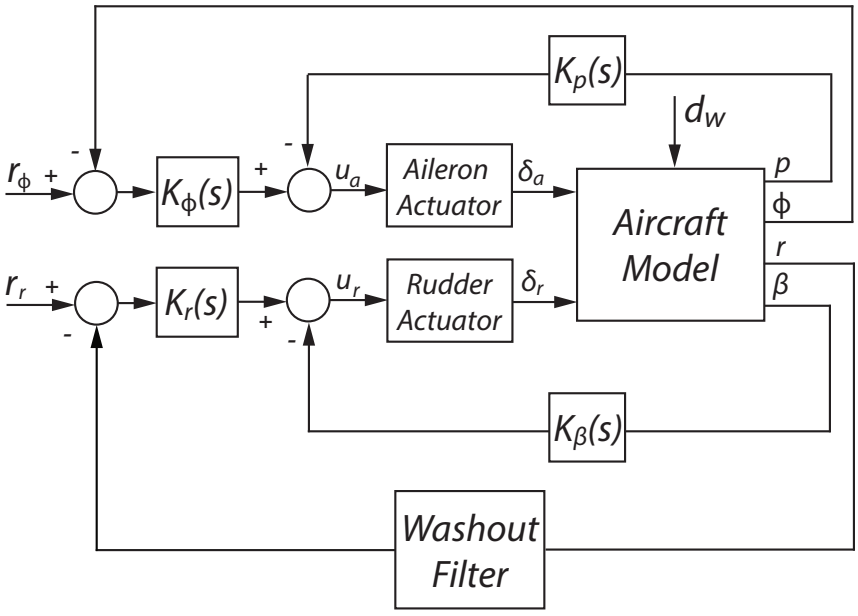


**Figure 6.1** System block diagram

A washout filter is used to overcome this problem. A simple first-order high pass filter can be used for the solution as follows:

$$Washout\ Filter = \frac{s}{s+1} \tag{6.3}$$

This filter works fine for short period inputs to eliminate the undesired yaw rates and stop filtering after $\tau = 1\ s$, which means that it does not resist the constant non-zero yaw rates after 1 $s$. Choosing the right $\tau$ value is important because if it is too small, the yaw damper will not work right. If it is too high, it will resist the desired yaw-rate during the coordinated steady-state turn by the pilot. The inner sideslip loop is used to eliminate the sideslip motion. In Figure 6.1, "Rudder Actuator" is a simple lag transfer function representing the rudder servo as follows:

$$Rudder\ Actuator = \frac{20.2}{s+20.2} \tag{6.4}$$

The upper loop is to control the roll angle $\phi$, which is generally controlled by the ailerons. The outer loop has a unity gain feedback. There needs to be an inner loop, mostly called a roll damper, which is required to augment the stability derivative and reduce the variation of the roll performance and the response time with flight conditions. "Aileron Actuator" represents an equivalent transfer function for differential actuation of the left and right ailerons which is

$$Aileron\ Actuator = \frac{20.2}{s+20.2} \tag{6.5}$$

Generalized plant P in Figure 6.2 is obtained from Figure 6.1 by simply keeping the controllers ($K_p(s)$, $K_\phi(s)$, $K_r(s)$, and $K_\beta(s)$) outside. There are two exogenous inputs as references. $W_a$ and $W_r$ are the weighting components that are used to keep the deflections of the actuators within their limits, which are ±21.5° for the ailerons and ±30° for the rudder of the F-16 aircraft model. The values of $W_a$ and $W_r$ are 0.1 and 0.5, respectively. These are defined as exogenous outputs ($z_2$ and $z_4$, respectively) in P. The other exogenous outputs are roll angle and yaw rate errors, which are needed to be minimized.

In Figure 6.2, there is one more exogenous input representing the disturbance $d_w$. It will be gone through two different scenarios. In the first one, there will be no external disturbance to the system, which will be zero in this case. In the second scenario, the wind gust, which is explained in detail in Section 4.5, is applied to the system with the white noise input, as shown in Figure 6.3.

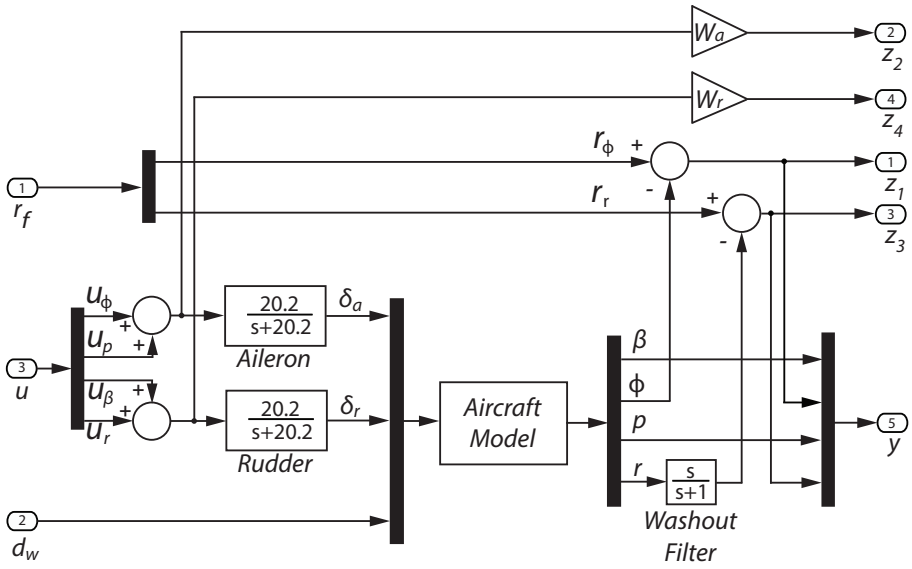


**Figure 6.2** Generalized plant P

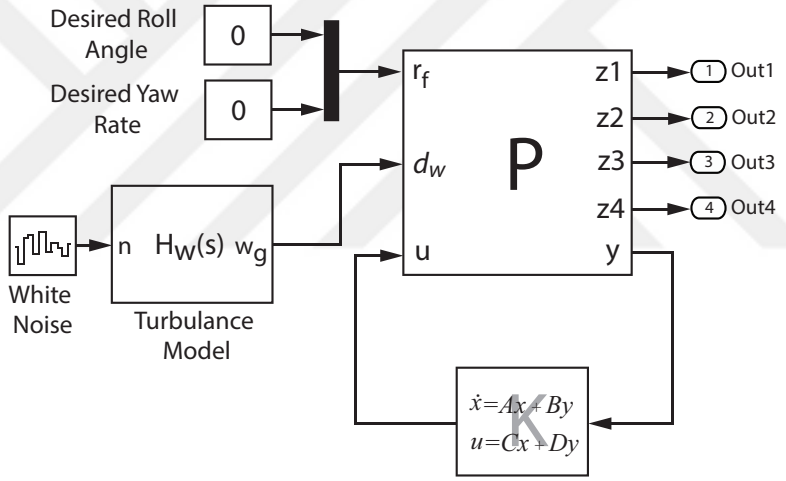


**Figure 6.3** P-K configuration with turbulence

#### 6.3.1.1 Case 1:

In this case, it is assumed that there is no disturbance added to the system. So, the same mathematical model of the plant can be used, as expressed in Section 6.2. Now, it is needed to have the generalized plant P matrix to use the rules in Section 3.4 to construct the controller. The generalized plant P matrix is obtained as follows:

$$
A_P = \begin{bmatrix}
-0.1569 & 0.1265 & 0.2262 & -0.9666 & 0 & 0.002905 & 0.007928 \\
0 & 0 & 1 & 0.1846 & 0 & 0 & 0 \\
-15.23 & 0 & -1.567 & 0.888 & 0 & -3.353 & 0.6183 \\
1.949 & 0 & -0.03652 & -0.2468 & 0 & -0.1235 & -0.3016 \\
0 & 0 & 0 & 57.3 & -1 & 0 & 0 \\
0 & 0 & 0 & 0 & 0 & -20.2 & 0 \\
0 & 0 & 0 & 0 & 0 & 0 & -20.2
\end{bmatrix}
$$

$$
B_P = \begin{bmatrix}
0 & 0 & 0 & 0 & 0 & 0 \\
0 & 0 & 0 & 0 & 0 & 0 \\
0 & 0 & 0 & 0 & 0 & 0 \\
0 & 0 & 0 & 0 & 0 & 0 \\
0 & 0 & 0 & 0 & 0 & 0 \\
0 & 0 & 0 & 1 & -1 & 0 \\
0 & 0 & -1 & 0 & 0 & 1
\end{bmatrix}
$$

$$
C_P = \begin{bmatrix}
0 & 0 & 0 & 0 & 0 & 0 & 0 \\
0 & 0 & 0 & 0 & 0 & 0 & 0 \\
0 & -57.3 & 0 & 0 & 0 & 0 & 0 \\
0 & 0 & 0 & -57.3 & 1 & 0 & 0 \\
57.3 & 0 & 0 & 0 & 0 & 0 & 0 \\
0 & -57.3 & 0 & 0 & 0 & 0 & 0 \\
0 & 0 & 57.3 & 0 & 0 & 0 & 0 \\
0 & 0 & 0 & -57.3 & 1 & 0 & 0
\end{bmatrix}
$$

$$
D_P = \begin{bmatrix}
0 & 0 & -0.5 & 0 & 0 & 0.5 \\
0 & 0 & 0 & 0.1 & -0.1 & 0 \\
1 & 0 & 0 & 0 & 0 & 0 \\
0 & 1 & 0 & 0 & 0 & 0 \\
0 & 0 & 0 & 0 & 0 & 0 \\
1 & 0 & 0 & 0 & 0 & 0 \\
0 & 0 & 0 & 0 & 0 & 0 \\
0 & 1 & 0 & 0 & 0 & 0
\end{bmatrix}
\tag{6.6}
$$

Therefore, the $H_\infty$ optimal feedback controller can be constructed by solving the LMIs as described in Section 3.4. The constructed controller is given as follows:

$$
A_K = 10^3 \times \begin{bmatrix}
-0.52 & -1.78 & 80.40 & 0.37 & -1.29 & 588.43 & -182.34 \\
0.65 & 2.20 & -101.07 & -0.49 & 1.66 & -740.91 & 228.42 \\
0.03 & 0.10 & -4.62 & -0.02 & 0.07 & -33.63 & 10.68 \\
-0.17 & -0.55 & 24.66 & -0.12 & -0.34 & 175.46 & -71.83 \\
0.02 & 0.08 & -3.51 & -0.01 & 0.05 & -25.63 & 8.26 \\
0.00 & -0.01 & 0.24 & 0.00 & 0.00 & 1.77 & -0.53 \\
0.00 & 0.01 & -0.38 & 0.00 & 0.01 & -2.71 & 0.99
\end{bmatrix}
$$

$$
B_K = 10^1 \times \begin{bmatrix}
150.89 & 1.39 & -361.71 & 53.33 \\
-196.96 & 3.90 & 469.43 & -68.46 \\
-12.34 & 0.23 & 21.35 & -5.29 \\
193.42 & 9.93 & -126.83 & 113.55 \\
-8.23 & -0.23 & 16.08 & -3.73 \\
0.37 & -0.05 & -1.09 & 0.07 \\
-2.22 & -0.09 & 1.84 & -1.32
\end{bmatrix}
$$

$$
C_K = \begin{bmatrix}
0.0072 & 0.0036 & -0.1346 & 0.0007 & 0.0809 & -0.9619 & 4.4238 \\
-0.0212 & -0.0854 & 2.9923 & 0.0261 & -0.0413 & -82.1674 & -5.6669 \\
-0.1527 & -0.5421 & 23.8266 & 0.1319 & -0.3624 & 174.8554 & -52.4321 \\
0.0001 & 0.0021 & -0.1382 & -0.0150 & 0.0150 & -1.5104 & -0.7255
\end{bmatrix}
$$

$$
D_K = \begin{bmatrix}
-1.0000 & -0.0005 & 0.0000 & -0.0005 \\
0.0000 & -1.0587 & -0.0000 & 0.0152 \\
0.0000 & 0.0000 & -1.0000 & 0.0000 \\
0.0000 & 0.0000 & 0.0000 & -1.0000
\end{bmatrix}
\tag{6.7}
$$

#### 6.3.1.2 Case 2:

There is an external input to the plant, which represents the turbulence as a disturbance in this case. The turbulence model was described in Section 4.5. So, this disturbance input changes the matrix B in Equation (6.2) as follows:

$$
B = \begin{bmatrix}
0.0001438 & 0.0003925 & -0.1569/250 \\
0 & 0 & 0 \\
-0.166 & 0.03061 & -15.23/250 \\
-0.006115 & -0.01493 & 1.949/250
\end{bmatrix}
\tag{6.8}
$$

The rest of the plant matrices stay the same. As the dynamic of the plant changes, the generalized plant P also changes. Matrices $A_P$ and $C_P$ of the generalized plant P are the same as the matrices given in Equation (6.6) in Case 1. However, the matrices $B_P$ and $D_P$ changes as follows:

$$B_P = \begin{bmatrix} 0 & 0 & 0.000627 & 0 & 0 & 0 & 0 \\ 0 & 0 & 0 & 0 & 0 & 0 & 0 \\ 0 & 0 & 0.06092 & 0 & 0 & 0 & 0 \\ 0 & 0 & -0.00779 & 0 & 0 & 0 & 0 \\ 0 & 0 & 0 & 0 & 0 & 0 & 0 \\ 0 & 0 & 0 & 0 & 1 & -1 & 0 \\ 0 & 0 & 0 & -1 & 0 & 0 & 1 \end{bmatrix} \quad D_P = \begin{bmatrix} 0 & 0 & 0 & -0.5 & 0 & 0 & 0.5 \\ 0 & 0 & 0 & 0 & 0.1 & -0.1 & 0 \\ 1 & 0 & 0 & 0 & 0 & 0 & 0 \\ 0 & 1 & 0 & 0 & 0 & 0 & 0 \\ 0 & 0 & 0 & 0 & 0 & 0 & 0 \\ 1 & 0 & 0 & 0 & 0 & 0 & 0 \\ 0 & 0 & 0 & 0 & 0 & 0 & 0 \\ 0 & 1 & 0 & 0 & 0 & 0 & 0 \end{bmatrix} \tag{6.9}$$

Now, the $H_\infty$ optimal feedback controller can be constructed by solving the LMIs, as described in Section 3.4. The constructed controller is given as follows:

$$A_K = 10^3 \times \begin{bmatrix} -0.33 & -1.07 & 50.04 & 0.23 & -0.93 & 367.05 & -113.65 \\ 0.51 & 1.69 & -78.95 & -0.35 & 1.33 & -578.60 & 180.53 \\ 0.03 & 0.11 & -4.84 & -0.02 & 0.07 & -35.26 & 11.30 \\ -0.43 & -1.47 & 65.51 & 0.08 & -0.80 & 474.71 & -162.93 \\ 0.02 & 0.06 & -2.82 & -0.01 & 0.05 & -20.61 & 6.68 \\ 0.00 & 0.00 & 0.16 & 0.00 & 0.00 & 1.15 & -0.35 \\ 0.01 & 0.02 & -0.79 & 0.00 & 0.01 & -5.78 & 1.93 \end{bmatrix}$$

$$B_K = 10^1 \times \begin{bmatrix} 243.26 & 1.01 & -243.56 & 48.45 \\ -221.25 & 3.66 & 386.86 & -91.69 \\ -8.78 & 0.26 & 23.04 & -7.72 \\ 33.52 & 7.84 & -311.32 & 158.38 \\ -10.71 & -0.20 & 13.69 & -4.07 \\ 0.51 & -0.05 & -0.76 & 0.12 \\ -0.55 & -0.07 & 3.76 & -1.86 \end{bmatrix} \tag{6.10}$$

$$C_K = \begin{bmatrix} 0.0070 & 0.0037 & -0.1375 & 0.0007 & 0.0779 & -0.9762 & 4.4311 \\ -0.0195 & -0.0787 & 2.7705 & 0.0269 & -0.0421 & -83.0233 & -5.0389 \\ -0.1505 & -0.5335 & 23.4072 & 0.1343 & -0.3648 & 172.0922 & -50.9333 \\ 0.0001 & 0.0022 & -0.1407 & -0.0149 & 0.0149 & -1.5213 & -0.7095 \end{bmatrix}$$

$$D_K = \begin{bmatrix} -1.0001 & -0.0004 & 0.0001 & -0.0005 \\ 0.0005 & -1.0513 & -0.0009 & 0.0182 \\ 0.0000 & 0.0000 & -1.0000 & 0.0000 \\ 0.0000 & 0.0000 & 0.0000 & -1.0000 \end{bmatrix}$$

### 6.3.2 Aircraft Lateral Beam Tracking Control

The block diagram for the lateral beam tracking control system is illustrated in Figure 6.4. This block diagram is constructed by using other feedbacks and controllers added on the block diagram given in Figure 6.1. All the necessary information about this additional section is provided in Section 4.2. The generalized plant P for Figure 6.4 is generated and shown in Figure 6.5 by keeping all the controllers outside. The functionality of all the components except $G_\psi$ in Figure 6.5 has described so far. $G_\psi$ is nothing but a proportional gain that may be needed, especially in a gusty environment. Figure 6.3 can illustrate the overall P-K configuration. However, the name of the upper reference input is different, which is "Desired Lambda Angle" at this time.

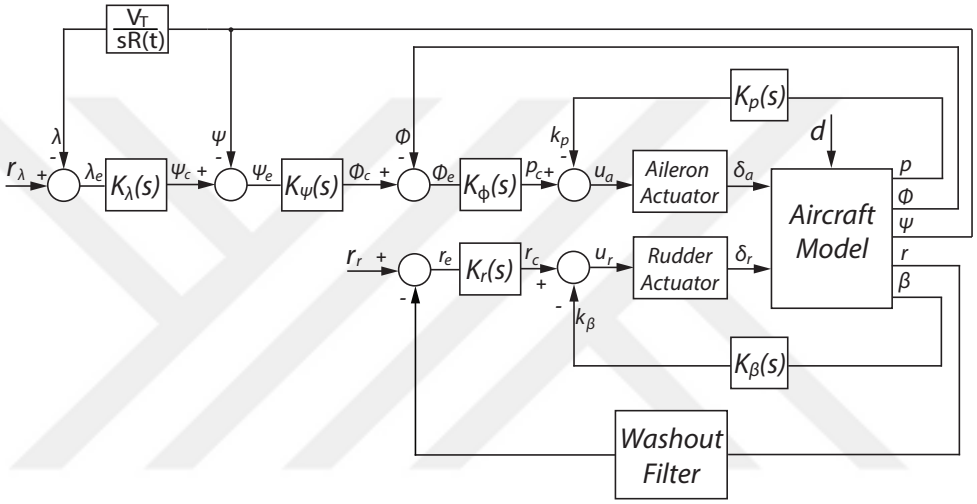


**Figure 6.4** Lateral beam guidance block diagram

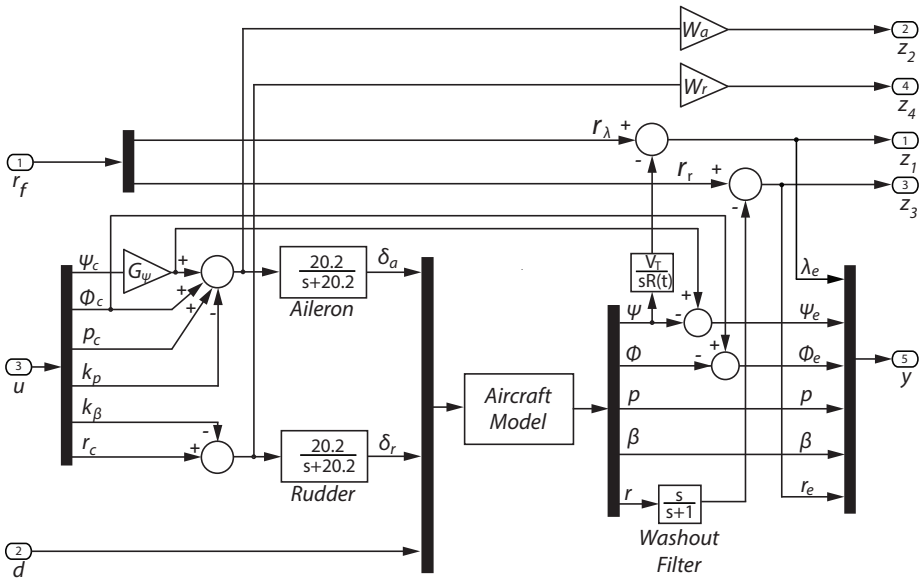


**Figure 6.5** Generalized plant P for lateral beam guidance

#### 6.3.2.1 Case 1:

In this case, it is assumed that there is no disturbance added to the system. The values of $W_a$, $W_r$, and $G_\psi$ are 5.926, 5.926 and 1, respectively. To construct the controller, the generalized plant P matrix is obtained as follows:

$$A_P = \begin{bmatrix} 0 & 0 & 0 & 0 & 0 & 0.3183 & 0 & 0 & 0 \\ 0 & -0.1569 & 0.1265 & 0.2262 & -0.9666 & 0 & 0 & 0.002905 & 0.007928 \\ 0 & 0 & 0 & 1 & 0.1846 & 0 & 0 & 0 & 0 \\ 0 & -15.23 & 0 & -1.567 & 0.888 & 0 & 0 & -3.353 & 0.6183 \\ 0 & 1.949 & 0 & -0.03652 & -0.2468 & 0 & 0 & -0.1235 & -0.3016 \\ 0 & 0 & 0 & 0 & 1.017 & 0 & 0 & 0 & 0 \\ 0 & 0 & 0 & 0 & 57.3 & 0 & -1 & 0 & 0 \\ 0 & 0 & 0 & 0 & 0 & 0 & 0 & -20.2 & 0 \\ 0 & 0 & 0 & 0 & 0 & 0 & 0 & 0 & -20.2 \end{bmatrix}$$

$$B_P = \begin{bmatrix} 0 & 0 & 0 & 0 & 0 & 0 & 0 & 0 \\ 0 & 0 & 0 & 0 & 0 & 0 & 0 & 0 \\ 0 & 0 & 0 & 0 & 0 & 0 & 0 & 0 \\ 0 & 0 & 0 & 0 & 0 & 0 & 0 & 0 \\ 0 & 0 & 0 & 0 & 0 & 0 & 0 & 0 \\ 0 & 0 & 0 & 0 & 0 & 0 & 0 & 0 \\ 0 & 0 & 0 & 0 & 0 & 0 & 0 & 0 \\ 0 & 0 & 1 & 1 & 1 & -1 & 0 & 0 \\ 0 & 0 & 0 & 0 & 0 & 0 & -1 & 1 \end{bmatrix} \quad D_P = \begin{bmatrix} 0 & 0 & 0 & 0 & 0 & 0 & -5.92 & 5.92 \\ 0 & 0 & 5.92 & 5.92 & 5.92 & -5.92 & 0 & 0 \\ 1 & 0 & 0 & 0 & 0 & 0 & 0 & 0 \\ 0 & 1 & 0 & 0 & 0 & 0 & 0 & 0 \\ 1 & 0 & 0 & 0 & 0 & 0 & 0 & 0 \\ 0 & 0 & 1 & 0 & 0 & 0 & 0 & 0 \\ 0 & 0 & 0 & 1 & 0 & 0 & 0 & 0 \\ 0 & 0 & 0 & 0 & 0 & 0 & 0 & 0 \\ 0 & 0 & 0 & 0 & 0 & 0 & 0 & 0 \\ 0 & 1 & 0 & 0 & 0 & 0 & 0 & 0 \end{bmatrix}$$

$$C_P = \begin{bmatrix} 0 & 0 & 0 & 0 & 0 & 0 & 0 & 0 & 0 \\ 0 & 0 & 0 & 0 & 0 & 0 & 0 & 0 & 0 \\ -1 & 0 & 0 & 0 & 0 & 0 & 0 & 0 & 0 \\ 0 & 0 & 0 & 0 & -57.3 & 0 & 1 & 0 & 0 \\ -1 & 0 & 0 & 0 & 0 & 0 & 0 & 0 & 0 \\ 0 & 0 & 0 & 0 & 0 & -57.3 & 0 & 0 & 0 \\ 0 & 0 & -57.3 & 0 & 0 & 0 & 0 & 0 & 0 \\ 0 & 0 & 0 & 57.3 & 0 & 0 & 0 & 0 & 0 \\ 0 & 57.3 & 0 & 0 & 0 & 0 & 0 & 0 & 0 \\ 0 & 0 & 0 & 0 & -57.3 & 0 & 1 & 0 & 0 \end{bmatrix} \tag{6.11}$$

The constructed controller obtained by solving the LMIs is given as follows:

$$
\begin{aligned}
A_K &= 10^6 \times \begin{bmatrix}
0.00 & -0.01 & -0.03 & 0.64 & 0.00 & 0.00 & 0.00 & 3.33 & -1.48 \\
0.00 & -0.38 & -1.77 & 35.22 & 0.00 & 0.00 & 0.01 & 182.29 & -81.36 \\
0.00 & -0.01 & -0.06 & 1.12 & 0.00 & 0.00 & 0.00 & 5.80 & -2.59 \\
0.00 & -0.02 & -0.08 & 1.65 & 0.00 & 0.00 & 0.00 & 8.53 & -3.81 \\
0.00 & -0.25 & -1.16 & 23.17 & 0.00 & 0.00 & 0.00 & 119.93 & -53.53 \\
0.00 & -0.03 & -0.12 & 2.38 & 0.00 & 0.00 & 0.00 & 12.32 & -5.50 \\
0.00 & 0.00 & 0.02 & -0.41 & 0.00 & 0.00 & 0.00 & -2.11 & 0.94 \\
0.00 & 0.00 & 0.02 & -0.37 & 0.00 & 0.00 & 0.00 & -1.92 & 0.86 \\
0.00 & 0.00 & 0.02 & -0.31 & 0.00 & 0.00 & 0.00 & -1.58 & 0.71
\end{bmatrix} \\
B_K &= 10^2 \times \begin{bmatrix}
11.46 & 8.55 & 3.22 & -8.02 & 2.63 & 2.67 \\
441.38 & 358.03 & 109.36 & -438.51 & -67.70 & 79.11 \\
19.86 & 14.98 & 5.51 & -14.05 & -1.70 & 3.94 \\
23.25 & 18.27 & 6.01 & -20.55 & -1.36 & 3.30 \\
387.31 & 298.62 & 106.42 & -290.98 & -116.18 & 110.00 \\
43.48 & 32.44 & 12.22 & -29.75 & 7.84 & 10.34 \\
-6.27 & -4.93 & -1.68 & 5.13 & 2.93 & -1.63 \\
-5.62 & -4.37 & -1.49 & 4.63 & 0.81 & -1.09 \\
-5.03 & -3.89 & -1.38 & 3.83 & 1.57 & -1.47
\end{bmatrix} \\
C_K &= \begin{bmatrix}
0.00 & 0.00 & 0.00 & 0.00 & 0.00 & 0.00 & 0.00 & 0.00 & 0.00 \\
0.10 & 0.00 & 0.10 & 0.00 & 0.00 & -0.10 & 0.50 & 0.00 & -0.10 \\
0.00 & -0.50 & -2.70 & 41.00 & 0.00 & 0.00 & 0.50 & 208.00 & -95.00 \\
0.00 & -8.80 & -41.00 & 814.80 & 0.00 & 0.00 & 0.60 & 4215.90 & -1882.20 \\
0.00 & 0.10 & 0.50 & -8.80 & 0.00 & 0.00 & 0.00 & -45.50 & 20.50 \\
0.00 & 0.00 & 0.00 & 0.00 & 0.00 & 0.00 & 0.00 & -0.30 & -0.70
\end{bmatrix} \\
D_K &= \begin{bmatrix}
-1.00 & 0.00 & 0.00 & 0.00 & 0.00 & 0.00 \\
-1.00 & -1.00 & 0.00 & 0.00 & 0.00 & 0.00 \\
-1.00 & -1.00 & -1.00 & 0.00 & 0.00 & 0.00 \\
0.00 & 0.00 & 0.00 & -1.00 & 0.00 & 0.00 \\
0.00 & 0.00 & 0.00 & 0.00 & -1.00 & 0.00 \\
0.00 & 0.00 & 0.00 & 0.00 & 0.00 & -1.00
\end{bmatrix}
\end{aligned}
\tag{6.12}
$$

#### 6.3.2.2 Case 2:

The moderate turbulence model is used as a disturbance in this case. The values of $W_a$, $W_r$, and $G_\psi$ are 1.8, 1.8, and 10, respectively. The disturbance input changes the matrix B in Equation (6.2) as follows:

$$
B = \begin{bmatrix}
0.0001438 & 0.0003925 & -0.1569/250 \\
0 & 0 & 0 \\
-0.166 & 0.03061 & -15.23/250 \\
-0.006115 & -0.01493 & 1.949/250 \\
0 & 0 & 0
\end{bmatrix}
\tag{6.13}
$$

As the dynamic of the plant changes, the generalized plant P also changes. The matrices $A_P$ and $C_P$ of the generalized plant P are the same as the matrices given in Equation (6.6) in Case 1. But, the matrices $B_P$ and $D_P$ changes as follows:

$$B_P = \begin{bmatrix} 0 & 0 & 0 & 0 & 0 & 0 & 0 & 0 & 0 \\ 0 & 0 & 0.000627 & 0 & 0 & 0 & 0 & 0 & 0 \\ 0 & 0 & 0 & 0 & 0 & 0 & 0 & 0 & 0 \\ 0 & 0 & 0.06092 & 0 & 0 & 0 & 0 & 0 & 0 \\ 0 & 0 & -0.00779 & 0 & 0 & 0 & 0 & 0 & 0 \\ 0 & 0 & 0 & 0 & 0 & 0 & 0 & 0 & 0 \\ 0 & 0 & 0 & 0 & 0 & 0 & 0 & 0 & 0 \\ 0 & 0 & 0 & 10 & 1 & 1 & -1 & 0 & 0 \\ 0 & 0 & 0 & 0 & 0 & 0 & 0 & -1 & 1 \end{bmatrix} \quad D_P = \begin{bmatrix} 0 & 0 & 0 & 0 & 0 & 0 & 0 & -1.8 & 1.8 \\ 0 & 0 & 0 & 18 & 1.8 & 1.8 & -1.8 & 0 & 0 \\ 1 & 0 & 0 & 0 & 0 & 0 & 0 & 0 & 0 \\ 0 & 1 & 0 & 0 & 0 & 0 & 0 & 0 & 0 \\ 1 & 0 & 0 & 0 & 0 & 0 & 0 & 0 & 0 \\ 0 & 0 & 0 & 10 & 0 & 0 & 0 & 0 & 0 \\ 0 & 0 & 0 & 0 & 1 & 0 & 0 & 0 & 0 \\ 0 & 0 & 0 & 0 & 0 & 0 & 0 & 0 & 0 \\ 0 & 0 & 0 & 0 & 0 & 0 & 0 & 0 & 0 \\ 0 & 1 & 0 & 0 & 0 & 0 & 0 & 0 & 0 \end{bmatrix} \tag{6.14}$$

The constructed controller for the new generalized plant P is obtained as follows:

$$A_K = 10^5 \times \begin{bmatrix} 0.00 & 0.00 & -0.02 & 0.38 & 0.00 & 0.00 & 0.00 & 1.94 & -0.87 \\ 0.00 & -0.22 & -1.08 & 20.01 & 0.00 & 0.00 & 0.03 & 103.11 & -45.99 \\ 0.00 & 0.00 & 0.00 & 0.06 & 0.00 & 0.00 & 0.00 & 0.32 & -0.14 \\ 0.00 & 0.00 & -0.01 & 0.17 & 0.00 & 0.00 & 0.00 & 0.89 & -0.391 \\ 0.00 & -0.19 & -0.90 & 17.06 & 0.00 & 0.00 & 0.03 & 88.03 & -39.30 \\ 0.00 & -0.01 & -0.07 & 1.27 & 0.00 & 0.00 & 0.00 & 6.54 & -2.91 \\ 0.00 & 0.00 & 0.01 & -0.23 & 0.00 & 0.00 & 0.00 & -1.21 & 0.54 \\ 0.00 & 0.00 & 0.01 & -0.10 & 0.00 & 0.00 & 0.00 & -0.53 & 0.24 \\ 0.00 & 0.00 & 0.01 & -0.25 & 0.00 & 0.00 & 0.00 & -1.29 & 0.58 \end{bmatrix}$$

$$B_K = 10^2 \times \begin{bmatrix} 11.62 & 0.87 & 0.59 & -1.12 & -1.11 & 1.25 \\ 683.84 & 47.14 & 22.45 & -58.64 & -3.40 & 50.39 \\ 7.90 & 0.32 & -0.01 & -0.17 & 0.82 & -0.66 \\ 13.48 & 0.52 & -0.05 & -0.48 & 1.58 & -1.08 \\ 552.14 & 44.40 & 25.23 & -50.63 & -26.47 & 66.44 \\ 39.98 & 2.99 & 1.99 & -3.78 & -3.59 & 4.20 \\ -8.49 & -0.64 & -0.31 & 0.69 & 0.06 & -0.80 \\ -4.61 & -0.29 & -0.11 & 0.30 & -0.12 & -0.14 \\ -7.86 & -0.64 & -0.37 & 0.74 & 0.42 & -1.00 \end{bmatrix} \tag{6.15}$$

$$C_K = \begin{bmatrix} 0.00 & 0.00 & 0.00 & 0.00 & 0.00 & 0.00 & 0.00 & 0.00 & 0.00 \\ 0.20 & 0.00 & 0.20 & 0.10 & 0.00 & -0.20 & 1.70 & 0.10 & -0.30 \\ 0.00 & -0.30 & -4.60 & 20.30 & 0.00 & 0.00 & 0.60 & 86.00 & -46.3 \\ 0.00 & -3.80 & -20.10 & 349.3 & 0.10 & 0.00 & 1.30 & 1792.80 & -802.10 \\ 0.00 & 0.00 & 0.30 & -3.80 & 0.00 & 0.00 & 0.00 & -19.00 & 9.20 \\ 0.00 & 0.00 & 0.00 & 0.10 & 0.00 & 0.00 & 0.10 & -0.80 & -1.90 \end{bmatrix}$$

$$D_K = \begin{bmatrix} -1.00 & 0.00 & 0.00 & 0.00 & 0.00 & 0.00 \\ -9.99 & -1.00 & 0.00 & 0.00 & 0.00 & 0.00 \\ -9.99 & -1.00 & -1.00 & 0.00 & 0.00 & 0.00 \\ 0.00 & 0.00 & 0.00 & -1.00 & 0.00 & 0.00 \\ 0.00 & 0.00 & 0.00 & 0.00 & -1.00 & 0.00 \\ 0.00 & 0.00 & 0.00 & 0.00 & 0.00 & -1.00 \end{bmatrix}$$

### 6.3.3 Model Following Method on Lateral Beam Tracking Control

Now, it is time to add the model following method to the aircraft lateral beam tracking system described in Section 6.3.2. However, it is preferred to control the lateral distance $d$ of the aircraft off course at this time shown in Figure 4.4. The same procedure could be done for the heading angle ($\psi$). The reference model described in Section 4.3 for the longitudinal flare phase is used in this section as the reference model. The reference model is given as follows:

$$h(t) = 500e^{(-t/40)} \tag{6.16}$$

The block diagram for the aircraft lateral beam model following method is illustrated in Figure 6.6, and the generalized plant P for this figure is generated as in Figure 6.7. $K_{ff}$ is the feedforward controller, and $r_a$ is the desired steady-state lateral distance, which is zero for this example.

#### 6.3.3.1 Case 1:

In this case, it is assumed that there is no disturbance added to the system. The values of $W_a$, $W_r$, and $W_d$ are 5, 5 and 4, respectively. To construct the controller, the generalized plant P matrix is obtained as follows:

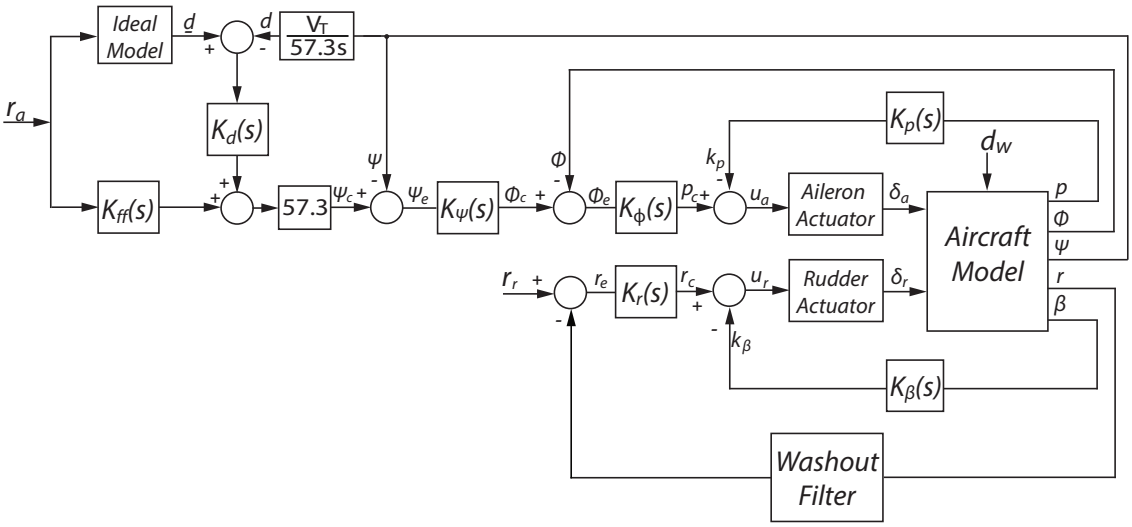


**Figure 6.6** Block diagram of lateral beam guidance with model following method

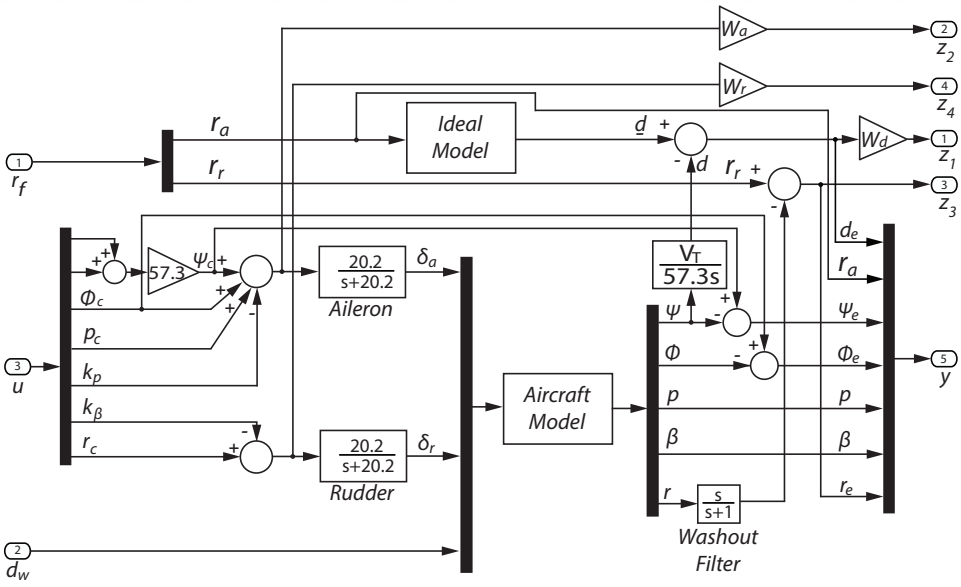


**Figure 6.7** Generalized plant P for lateral beam guidance with model following method

$$
A_P = \begin{bmatrix}
-0.15 & 0 & 0 & 0 & 0 & 0 & 0 & 0 & 0 & 0 \\
0 & 0 & 0 & 0 & 0 & 0 & 250 & 0 & 0 & 0 \\
0 & 0 & -0.1569 & 0.1265 & 0.2262 & -0.9666 & 0 & 0 & 0.0029 & 0.0079 \\
0 & 0 & 0 & 0 & 1 & 0.1846 & 0 & 0 & 0 & 0 \\
0 & 0 & -15.23 & 0 & -1.567 & 0.888 & 0 & 0 & -3.353 & 0.6183 \\
0 & 0 & 1.949 & 0 & -0.0365 & -0.2468 & 0 & 0 & -0.1235 & -0.3016 \\
0 & 0 & 0 & 0 & 0 & 1.017 & 0 & 0 & 0 & 0 \\
0 & 0 & 0 & 0 & 0 & 57.3 & 0 & -1 & 0 & 0 \\
0 & 0 & 0 & 0 & 0 & 0 & 0 & 0 & -20.2 & 0 \\
0 & 0 & 0 & 0 & 0 & 0 & 0 & 0 & 0 & -20.2
\end{bmatrix}
$$

$$
B_P = \begin{bmatrix}
1 & 0 & 0 & 0 & 0 & 0 & 0 & 0 & 0 \\
0 & 0 & 0 & 0 & 0 & 0 & 0 & 0 & 0 \\
0 & 0 & 0 & 0 & 0 & 0 & 0 & 0 & 0 \\
0 & 0 & 0 & 0 & 0 & 0 & 0 & 0 & 0 \\
0 & 0 & 0 & 0 & 0 & 0 & 0 & 0 & 0 \\
0 & 0 & 0 & 0 & 0 & 0 & 0 & 0 & 0 \\
0 & 0 & 0 & 0 & 0 & 0 & 0 & 0 & 0 \\
0 & 0 & 0 & 0 & 0 & 0 & 0 & 0 & 0 \\
0 & 0 & 57.3 & 57.3 & 1 & 1 & -1 & 0 & 0 \\
0 & 0 & 0 & 0 & 0 & 0 & 0 & -1 & 1
\end{bmatrix}
\quad
D_P = \begin{bmatrix}
0 & 0 & 0 & 0 & 0 & 0 & 0 & -5 & 5 \\
0 & 0 & 286 & 286 & 5 & 5 & -5 & 0 & 0 \\
0 & 0 & 0 & 0 & 0 & 0 & 0 & 0 & 0 \\
0 & 1 & 0 & 0 & 0 & 0 & 0 & 0 & 0 \\
0 & 0 & 0 & 0 & 0 & 0 & 0 & 0 & 0 \\
1 & 0 & 0 & 0 & 0 & 0 & 0 & 0 & 0 \\
0 & 0 & 57.3 & 57.3 & 0 & 0 & 0 & 0 & 0 \\
0 & 0 & 0 & 0 & 1 & 0 & 0 & 0 & 0 \\
0 & 0 & 0 & 0 & 0 & 0 & 0 & 0 & 0 \\
0 & 0 & 0 & 0 & 0 & 0 & 0 & 0 & 0 \\
0 & 1 & 0 & 0 & 0 & 0 & 0 & 0 & 0
\end{bmatrix}
$$

$$
C_P = \begin{bmatrix}
0 & 0 & 0 & 0 & 0 & 0 & 0 & 0 & 0 & 0 \\
0 & 0 & 0 & 0 & 0 & 0 & 0 & 0 & 0 & 0 \\
7 & -7 & 0 & 0 & 0 & 0 & 0 & 0 & 0 & 0 \\
0 & 0 & 0 & 0 & 0 & -57.3 & 0 & 1 & 0 & 0 \\
1 & -1 & 0 & 0 & 0 & 0 & 0 & 0 & 0 & 0 \\
0 & 0 & 0 & 0 & 0 & 0 & 0 & 0 & 0 & 0 \\
0 & 0 & 0 & 0 & 0 & 0 & -57.3 & 0 & 0 & 0 \\
0 & 0 & 0 & -57.3 & 0 & 0 & 0 & 0 & 0 & 0 \\
0 & 0 & 0 & 0 & 57.3 & 0 & 0 & 0 & 0 & 0 \\
0 & 0 & 57.3 & 0 & 0 & 0 & 0 & 0 & 0 & 0 \\
0 & 0 & 0 & 0 & 0 & -57.3 & 0 & 1 & 0 & 0
\end{bmatrix}
\tag{6.17}
$$

The constructed controller for the new generalized plant P is obtained as follows:

$$A_K = 10^7 \times \begin{bmatrix} 1.63 & 1.87 & 0.00 & -0.01 & -0.42 & 0.00 & 0.00 & 0.07 & -2.31 & 0.96 \\ -1.87 & -2.15 & -0.01 & 0.01 & 0.49 & 0.00 & 0.00 & -0.08 & 2.71 & -1.12 \\ -128 & -147 & -0.51 & 0.04 & 45.67 & -0.23 & 0.28 & -5.86 & 248.3 & -104 \\ -1.58 & -1.82 & -0.01 & -0.01 & 0.69 & 0.00 & 0.00 & -0.07 & 3.73 & -1.58 \\ -3.05 & -3.52 & -0.02 & -0.02 & 1.45 & -0.01 & 0.01 & -0.14 & 7.81 & -3.32 \\ -171 & -196 & -0.59 & 0.46 & 52.39 & -0.30 & 0.37 & -7.77 & 287.0 & -119 \\ -439 & -503 & -1.46 & 1.40 & 129.11 & -0.77 & 0.95 & -19.85 & 708.7 & -294 \\ -0.01 & -0.01 & 0.00 & 0.00 & 0.00 & 0.00 & 0.00 & 0.00 & 0.00 & 0.00 \\ 1.31 & 1.50 & 0.01 & 0.00 & -0.48 & 0.00 & 0.00 & 0.06 & -2.61 & 1.10 \\ 2.25 & 2.58 & 0.01 & -0.01 & -0.68 & 0.00 & 0.00 & 0.10 & -3.71 & 1.55 \end{bmatrix}$$

$$B_K = 10^6 \times \begin{bmatrix} 2.26 & 0.12 & 0.00 & 0.00 & 0.00 & 0.00 & 0.00 \\ -2.60 & -0.14 & 0.00 & 0.00 & 0.00 & 0.00 & 0.00 \\ -181.04 & -9.81 & -0.21 & 0.04 & -0.05 & 0.21 & 0.07 \\ -2.27 & -0.12 & 0.00 & 0.00 & 0.00 & 0.00 & 0.00 \\ -4.39 & -0.23 & -0.01 & 0.00 & 0.00 & 0.01 & 0.00 \\ -239.80 & -13.17 & -0.28 & 0.05 & -0.05 & 0.27 & 0.09 \\ -612.19 & -33.59 & -0.72 & 0.13 & -0.13 & 0.69 & 0.24 \\ -0.01 & 0.00 & 0.00 & 0.00 & 0.00 & 0.00 & 0.00 \\ 1.85 & 0.10 & 0.00 & 0.00 & 0.00 & 0.00 & 0.00 \\ 3.14 & 0.17 & 0.00 & 0.00 & 0.00 & 0.00 & 0.00 \end{bmatrix}$$

$$C_K = 10^2 \times \begin{bmatrix} -0.10 & -0.11 & 0.00 & 0.00 & 0.00 & 0.00 & 0.00 & 0.00 & 0.00 & 0.00 \\ 0.00 & 0.00 & 0.00 & 0.00 & 0.00 & 0.00 & 0.00 & 0.00 & 0.00 & 0.00 \\ 10.59 & 10.00 & 0.00 & 0.07 & -0.06 & -0.01 & 0.00 & -0.11 & 0.02 & 0.13 \\ 13.18 & 12.66 & -0.06 & -0.24 & 5.08 & 0.00 & 0.00 & -0.04 & 26.28 & -11.85 \\ 20.63 & 20.70 & -1.11 & -5.14 & 102.81 & 0.04 & -0.02 & 0.17 & 532.55 & -235.4 \\ -0.50 & -0.50 & 0.01 & 0.06 & -1.11 & 0.00 & 0.00 & 0.00 & -5.74 & 2.58 \\ 0.31 & 0.31 & 0.00 & 0.00 & -0.04 & -0.02 & 0.00 & 0.03 & -0.39 & -0.92 \end{bmatrix}$$

$$D_K = \begin{bmatrix} -1.00 & 0.00 & 0.00 & 0.00 & 0.00 & 0.00 & 0.00 \\ 0.00 & -1.00 & 0.00 & 0.00 & 0.00 & 0.00 & 0.00 \\ -57.30 & -57.30 & -1.00 & 0.00 & 0.00 & 0.00 & 0.00 \\ -57.30 & -57.30 & -1.00 & -1.00 & 0.00 & 0.00 & 0.00 \\ 0.00 & 0.00 & 0.00 & 0.00 & -1.00 & 0.00 & 0.00 \\ 4 \times 10^4 & 0.00 & 0.00 & 0.00 & 0.00 & -1.00 & 0.00 \\ 0.00 & 0.00 & 0.00 & 0.00 & 0.00 & 0.00 & -1.00 \end{bmatrix} \tag{6.18}$$

#### 6.3.3.2 Case 2:

The moderate turbulence model is used as a disturbance in this case. The values of $W_a$, $W_r$, and $W_d$ are 2, 2 and 2 respectively. The generalized plant P matrix is obtained as follows:

$$
A_P = \begin{bmatrix}
-0.025 & 0 & 0 & 0 & 0 & 0 & 0 & 0 & 0 & 0 \\
0 & 0 & 0 & 0 & 0 & 0 & 250 & 0 & 0 & 0 \\
0 & 0 & -0.1569 & 0.1265 & 0.2262 & -0.9666 & 0 & 0 & 0.0029 & 0.0079 \\
0 & 0 & 0 & 0 & 1 & 0.1846 & 0 & 0 & 0 & 0 \\
0 & 0 & -15.23 & 0 & -1.567 & 0.888 & 0 & 0 & -3.353 & 0.6183 \\
0 & 0 & 1.949 & 0 & -0.0365 & -0.2468 & 0 & 0 & -0.1235 & -0.3016 \\
0 & 0 & 0 & 0 & 0 & 1.017 & 0 & 0 & 0 & 0 \\
0 & 0 & 0 & 0 & 0 & 57.3 & 0 & -1 & 0 & 0 \\
0 & 0 & 0 & 0 & 0 & 0 & 0 & 0 & -20.2 & 0 \\
0 & 0 & 0 & 0 & 0 & 0 & 0 & 0 & 0 & -20.2
\end{bmatrix}
$$

$$
B_P = \begin{bmatrix}
1 & 0 & 0 & 0 & 0 & 0 & 0 & 0 & 0 & 0 \\
0 & 0 & 0 & 0 & 0 & 0 & 0 & 0 & 0 & 0 \\
0 & 0 & 0.0006 & 0 & 0 & 0 & 0 & 0 & 0 & 0 \\
0 & 0 & 0 & 0 & 0 & 0 & 0 & 0 & 0 & 0 \\
0 & 0 & 0.0609 & 0 & 0 & 0 & 0 & 0 & 0 & 0 \\
0 & 0 & -0.0077 & 0 & 0 & 0 & 0 & 0 & 0 & 0 \\
0 & 0 & 0 & 0 & 0 & 0 & 0 & 0 & 0 & 0 \\
0 & 0 & 0 & 0 & 0 & 0 & 0 & 0 & 0 & 0 \\
0 & 0 & 0 & 57.3 & 57.3 & 1 & 1 & -1 & 0 & 0 \\
0 & 0 & 0 & 0 & 0 & 0 & 0 & 0 & -1 & 1
\end{bmatrix}
$$

$$
C_P = \begin{bmatrix}
0 & 0 & 0 & 0 & 0 & 0 & 0 & 0 & 0 & 0 \\
0 & 0 & 0 & 0 & 0 & 0 & 0 & 0 & 0 & 0 \\
2 & -2 & 0 & 0 & 0 & 0 & 0 & 0 & 0 & 0 \\
0 & 0 & 0 & 0 & 0 & -57.3 & 0 & 1 & 0 & 0 \\
1 & -1 & 0 & 0 & 0 & 0 & 0 & 0 & 0 & 0 \\
0 & 0 & 0 & 0 & 0 & 0 & 0 & 0 & 0 & 0 \\
0 & 0 & 0 & 0 & 0 & 0 & -57.3 & 0 & 0 & 0 \\
0 & 0 & 0 & -57.3 & 0 & 0 & 0 & 0 & 0 & 0 \\
0 & 0 & 0 & 0 & 57.3 & 0 & 0 & 0 & 0 & 0 \\
0 & 0 & 57.3 & 0 & 0 & 0 & 0 & 0 & 0 & 0 \\
0 & 0 & 0 & 0 & 0 & -57.3 & 0 & 1 & 0 & 0
\end{bmatrix}
$$

$$
D_P = \begin{bmatrix}
0 & 0 & 0 & 0 & 0 & 0 & 0 & 0 & -2 & 2 \\
0 & 0 & 0 & 114.6 & 114.6 & 2 & 2 & -2 & 0 & 0 \\
0 & 0 & 0 & 0 & 0 & 0 & 0 & 0 & 0 & 0 \\
0 & 1 & 0 & 0 & 0 & 0 & 0 & 0 & 0 & 0 \\
0 & 0 & 0 & 0 & 0 & 0 & 0 & 0 & 0 & 0 \\
1 & 0 & 0 & 0 & 0 & 0 & 0 & 0 & 0 & 0 \\
0 & 0 & 0 & 57.3 & 57.3 & 0 & 0 & 0 & 0 & 0 \\
0 & 0 & 0 & 0 & 0 & 1 & 0 & 0 & 0 & 0 \\
0 & 0 & 0 & 0 & 0 & 0 & 0 & 0 & 0 & 0 \\
0 & 0 & 0 & 0 & 0 & 0 & 0 & 0 & 0 & 0 \\
0 & 1 & 0 & 0 & 0 & 0 & 0 & 0 & 0 & 0
\end{bmatrix}
$$

(6.19)

The constructed controller for the new generalized plant P is obtained as follows:

$$
A_K = 10^8 \times \begin{bmatrix}
-0.02 & 0.01 & 0.00 & 0.00 & -0.10 & 0.00 & -0.00 & 0.01 & -0.52 & 0.22 \\
0.02 & -0.01 & 0.00 & 0.00 & 0.10 & 0.00 & 0.00 & -0.01 & 0.53 & -0.22 \\
1.43 & -0.47 & -0.07 & -0.15 & 6.39 & -0.01 & 0.02 & -0.42 & 34.08 & -14.27 \\
0.01 & 0.00 & 0.00 & 0.00 & 0.05 & 0.00 & 0.00 & 0.00 & 0.28 & -0.12 \\
0.02 & -0.01 & 0.00 & 0.00 & 0.11 & 0.00 & 0.00 & -0.01 & 0.60 & -0.25 \\
2.00 & -0.65 & -0.10 & -0.21 & 8.91 & -0.01 & 0.02 & -0.58 & 47.56 & -19.91 \\
5.19 & -1.69 & -0.26 & -0.55 & 23.03 & -0.02 & 0.06 & -1.51 & 122.9 & -51.46 \\
0.00 & 0.00 & 0.00 & 0.00 & 0.00 & 0.00 & 0.00 & 0.00 & 0.01 & 0.00 \\
-0.01 & 0.00 & 0.00 & 0.00 & -0.06 & 0.00 & 0.00 & 0.00 & -0.32 & 0.14 \\
-0.03 & 0.01 & 0.00 & 0.00 & -0.12 & 0.00 & 0.00 & 0.01 & -0.63 & 0.26
\end{bmatrix}
$$

$$
B_K = 10^6 \times \begin{bmatrix}
1.61 & 0.13 & 0.00 & 0.00 & 0.00 & 0.00 & 0.00 \\
-1.65 & -0.14 & 0.00 & 0.00 & 0.00 & 0.00 & 0.00 \\
-104.73 & -8.65 & -0.17 & 0.05 & -0.09 & -0.03 & 0.03 \\
-0.83 & -0.07 & 0.00 & 0.00 & 0.00 & 0.00 & 0.00 \\
-1.82 & -0.15 & 0.00 & 0.00 & 0.00 & 0.00 & 0.00 \\
-146.49 & -12.13 & -0.24 & 0.07 & -0.12 & -0.05 & 0.05 \\
-379.19 & -31.37 & -0.61 & 0.18 & -0.31 & -0.12 & 0.12 \\
-0.02 & 0.00 & 0.00 & 0.00 & 0.00 & 0.00 & 0.00 \\
0.99 & 0.08 & 0.00 & 0.00 & 0.00 & 0.00 & 0.00 \\
1.94 & 0.16 & 0.00 & 0.00 & 0.00 & 0.00 & 0.00
\end{bmatrix}
$$

$$
C_K = 10^2 \times \begin{bmatrix}
0.01 & -0.01 & 0.00 & 0.00 & 0.00 & 0.00 & 0.00 & 0.00 & 0.00 & 0.01 \\
0.00 & 0.00 & 0.00 & 0.00 & 0.00 & 0.00 & 0.00 & 0.00 & 0.00 & 0.00 \\
5.24 & 4.21 & 0.00 & 0.09 & -0.08 & 0.00 & 0.01 & -0.23 & 0.10 & 0.46 \\
4.20 & 3.26 & -0.05 & -0.21 & 3.89 & 0.00 & 0.01 & -0.15 & 20.03 & -8.95 \\
0.06 & 0.14 & -0.85 & -3.97 & 78.31 & 0.00 & 0.00 & 0.06 & 405.01 & -180.93 \\
0.01 & 0.01 & 0.01 & 0.05 & -0.84 & 0.00 & 0.00 & 0.00 & -4.30 & 1.96 \\
0.00 & 0.00 & 0.00 & 0.00 & 0.00 & -0.01 & 0.00 & 0.01 & -0.10 & -0.42
\end{bmatrix}
$$

$$
D_K = \begin{bmatrix}
-1.00 & 0.00 & 0.00 & 0.00 & 0.00 & 0.00 & 0.00 \\
0.00 & -1.00 & 0.00 & 0.00 & 0.00 & 0.00 & 0.00 \\
-57.30 & -57.30 & -1.00 & 0.00 & 0.00 & 0.00 & 0.00 \\
-57.30 & -57.30 & -1.00 & -1.00 & 0.00 & 0.00 & 0.00 \\
0.00 & 0.00 & 0.00 & 0.00 & -1.00 & 0.00 & 0.00 \\
-0.37 & -0.38 & -0.01 & 0.00 & -0.02 & -1.00 & 0.00 \\
0.00 & 0.00 & 0.00 & 0.00 & 0.00 & 0.00 & -1.00
\end{bmatrix}
\tag{6.20}
$$

The $H_\infty$ norm comparisons of the open-loop versus closed-loop behaviours for both the Case 1 and Case 2 are shown in Table 6.3. $H_\infty$ norms of the open-loop systems are infinity, which means that the systems are unstable. However, the overall systems become stable with the synthesized $H_\infty$ controllers.

**Table 6.3** $H_\infty$ norm comparison

| | $H_\infty$ **Norm** | |
|---|---|---|
| **Type** | **Case1** | **Case 2** |
| Open-Loop | $\infty$ | $\infty$ |
| Closed-Loop | 3.57 | 1.87 |

## 6.4 Simulation Results

Before doing the simulations for the overall system, we will take a look at the open-loop behavior of the plant to understand the effect of the controller better. The eigenvalues of the open-loop plant are given as below:

$$\begin{aligned} -0.4053 \pm j2.2122 \quad & \textit{Dutch Roll Mode} \\ -1.1299 \quad & \textit{Roll Mode} \\ -0.0301 \quad & \textit{Spiral Mode} \end{aligned} \tag{6.21}$$

The dutch roll mode has complex roots having a damping ratio of 0.18. As the damping ratio is very closed to the imaginary axis, the oscillation is very lightly damped. Also, the period of the dutch roll mode is 2.84 $s$. According to these values, it can be said that the landing in the turbulence conditions might be challenging for the pilot to handle.

The roll and spiral modes have real roots, thus, exponential responses. The roll mode is the fastest. The spiral mode is the slowest and could be unstable for some aircraft. However, it is easy to handle it by the pilot as it has a lengthy response. Figure 6.8a and 6.8b belong to the open-loop response of the plant. The initial states are selected as

$$x(0) = \begin{bmatrix} \beta \\ \phi \\ p \\ r \end{bmatrix} = \begin{bmatrix} 1/57.296 \\ 0 \\ 0 \\ 0 \end{bmatrix} \tag{6.22}$$

The dutch roll mode has the prominent oscillations as expected. When $\beta$ is disturbed, the other modes also have some oscillations even if they have only real roots, because the rudder excites all the modes. The spiral state also has a steady-state error. That actually explains why it is called the spiral mode. A small steady-state bank angle error causes the aircraft to make spiral movement over time if it is not taken care of.

One approach to handle the effect of the dutch roll mode is to use a yaw damping feedback, as shown at the bottom of Figure 6.1. This feedback eliminates the yaw rate generated during the dutch roll mode by manipulating the rudder to generate yaw moment, as described more detailed in Section 6.3. How the yaw damper feedback improves the system behavior can be seen in Figure 6.8c and 6.8d. The oscillations look better with the help of this feedback. However, it is not good enough. To make a much better improvement to the response of the plant, we will use the entire structure described in Section 6.3.

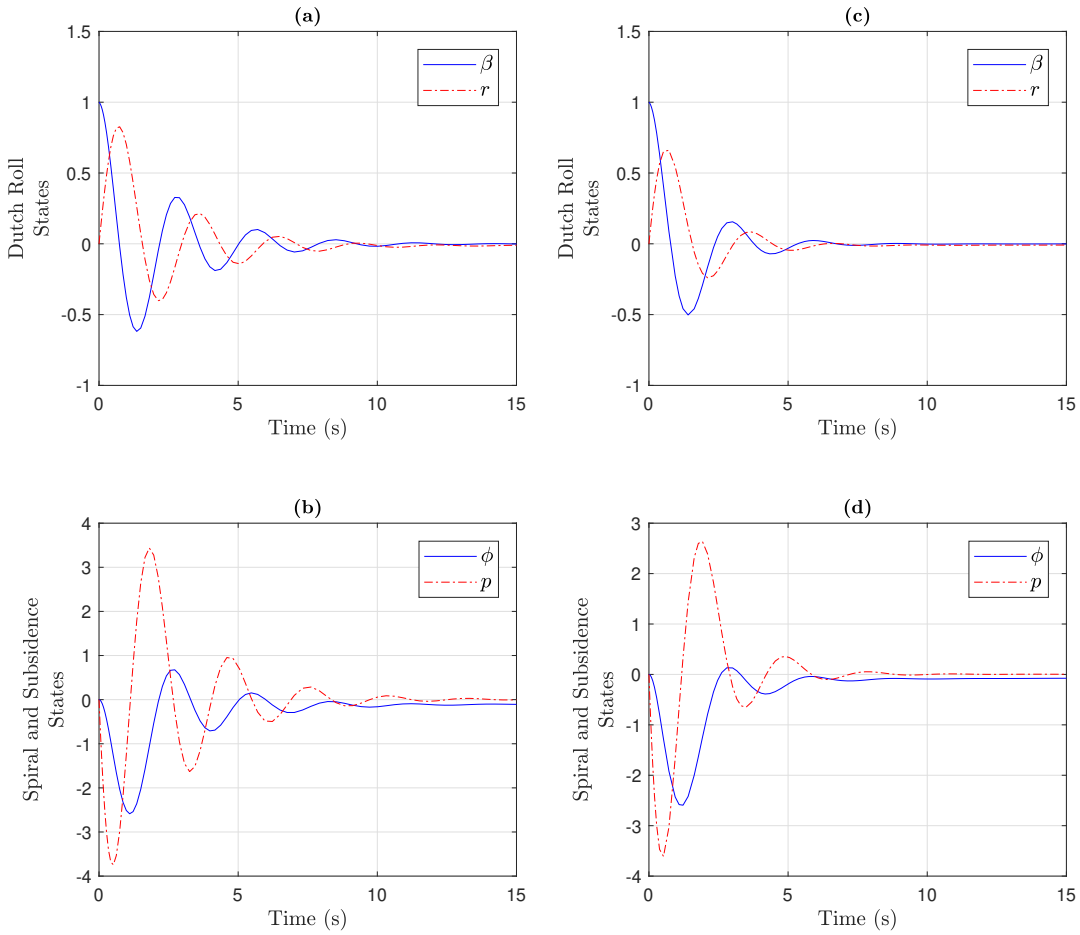


**Figure 6.8** Open loop states (a) Dutch roll states (b) Spiral and subsidence states; Only yaw damper feedback states (c) Dutch roll states (d) Spiral and subsidence states

### 6.4.1 Simulation Results for Aircraft Lateral Control

#### 6.4.1.1 Case 1:

Figure 6.3 shows the main block diagram for all the simulations. The general plant P and $H_\infty$ optimal feedback controller have been found in Equations (6.6) and (6.7),

so far. The disturbance input is assumed to be zero because there is no external disturbance for Case 1. Simulation results are given in Figure 6.9. When the dutch roll response is compared with the open-loop response, the undesirable oscillations are highly suppressed. On the other hand, similar suppression can be seen for the spiral and the subsidence states as well. When $\beta$ is disturbed by giving an initial value, the controller produces the necessary input voltage for the actuator of the rudder to generate the yawing moment to compensate for the yaw rate created by the initial value of $\beta$. The initial value of $\beta$ also excites the bank angle, and the controller produces the necessary input voltage for the actuator of the aileron to generate the rolling moment to compensate for the roll rate to settle the bank angle to zero again. Another thing to notice that there is no steady-state error on the bank angle. It means that the pilot does not need to handle the spiral mode. All the states are smoothly settled down to their steady-state values with very decent overshoots when compared with the open-loop response. On the other hand, the control inputs are far below the limits, as seen in Figure 6.9.

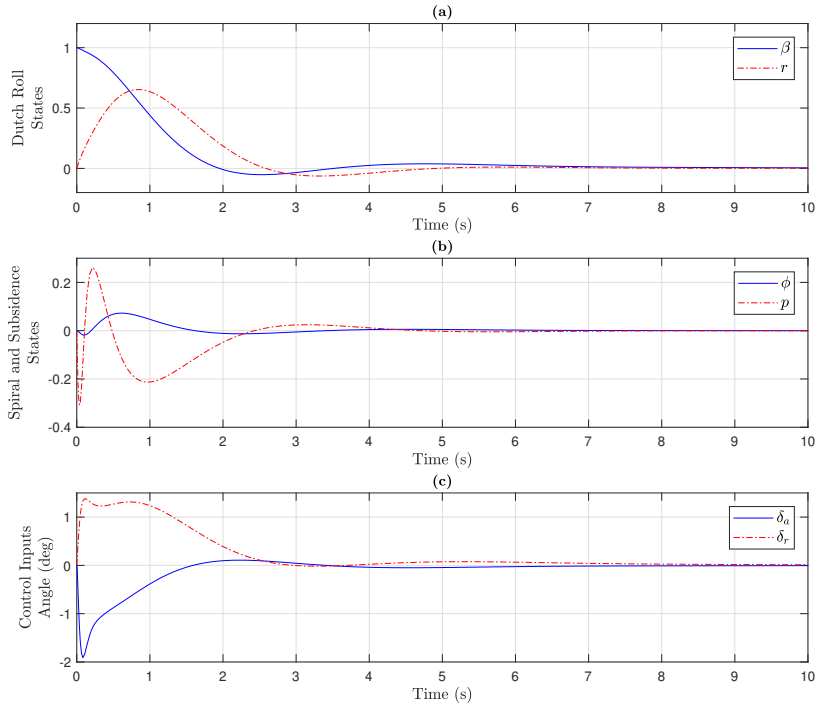


**Figure 6.9** Lateral simulation outcomes for no turbulence (a) Dutch roll states (b) Spiral and subsidence states (c) Control inputs

#### 6.4.1.2 Case 2:

In this case, the turbulence model is added to the system, as shown in Figure 6.3. There are two turbulence models, which are the light turbulence and moderate turbulence,

used in the simulations as detailed in Section 4.5. Firstly, we will consider that the aircraft encounters the light turbulence. The general plant P and $H_\infty$ optimal feedback controller was found in Equations (6.9) and (6.10). Simulation results are given in Figure 6.10a, 6.10b, and 6.10c.

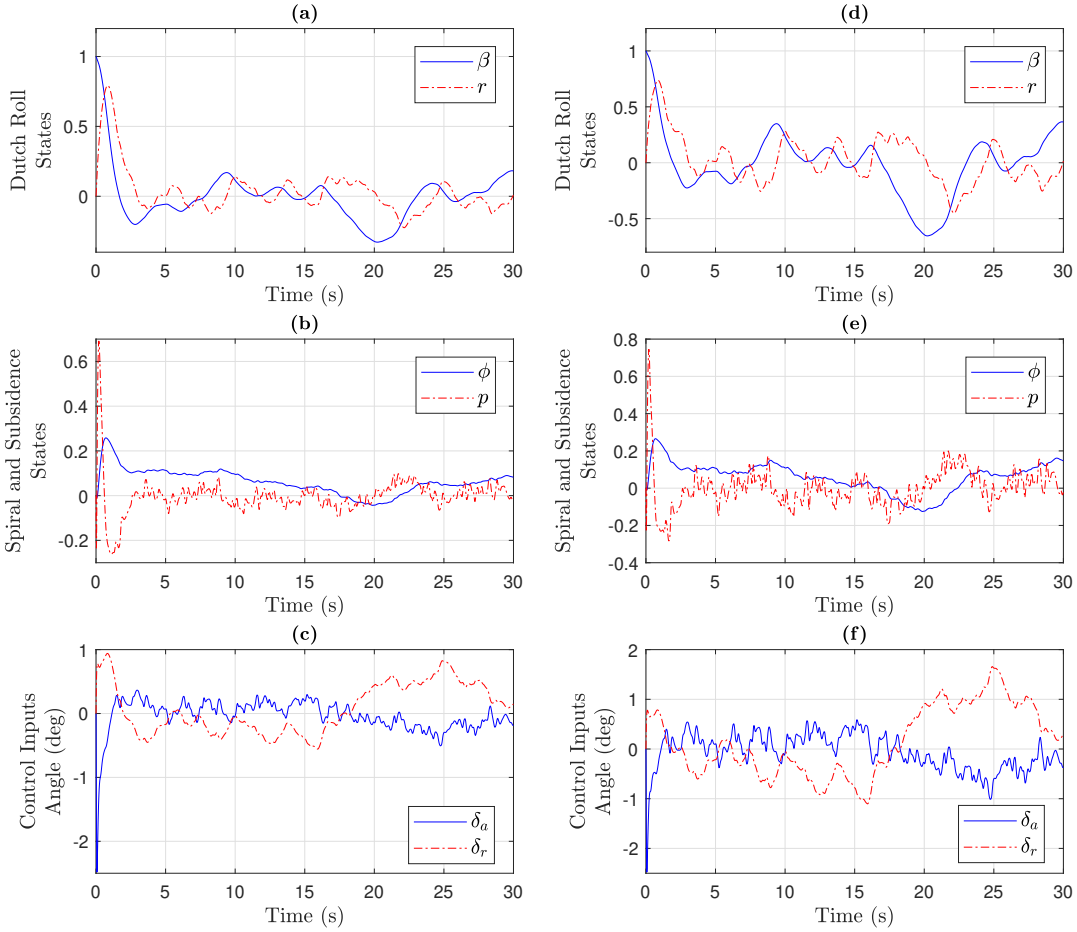


**Figure 6.10** Aircraft lateral states under light turbulence: (a) Dutch roll states (b) Spiral and subsidence states (c) Control inputs; Aircraft lateral states under moderate turbulence: (d) Dutch roll states (e) Spiral and subsidence states (f) Control inputs

At first glance, the controller keeps the aircraft stable and very close to zero after the initial value of $\beta$ is handled. The control procedure is the same as described in Case 1. However, in this case, the sideslip angle always changes when the aircraft is in a gusty wind condition. So, the yawing rate ($r$) changes with the change of the sideslip angle. The controller is working to generate the yawing moment to compensate for this unwanted yaw rate by manipulating the rudder. The variations in the sideslip angle in the gusty wind also excite the bank angle ($\phi$), and thus, the roll rate ($p$). The controller also works to generate a rolling moment to compensate for this unwanted roll rate by manipulating the ailerons throughout the turbulence. Consequently, the

controller achieves to keep both the amplitudes of these variations in a minimal range and the control inputs far below the limits, as seen in Figure 6.10(c).

Secondly, we will consider that the aircraft encounters moderate turbulence conditions. Simulation results are given in Figure 6.10d, 6.10e, and 6.10f. As seen from the figures, the controller keeps the aircraft stable and the amplitudes of the variations in a very decent range even under the moderate turbulence condition. The control inputs are far below the limits as well.

### 6.4.2 Simulation Results for Aircraft Lateral Beam Tracking Control

#### 6.4.2.1 Case 1:

In this case, it is assumed that the external input $d_w$ in Figure 6.3 is zero. Remember that Figure 6.3 can illustrate the overall P-K configuration. However, the name of the upper reference input is different, which is called "Desired Lambda Angle" at this time. Matrix form of the generalized plant $P$ and $H_\infty$ optimal controller, which was constructed before, have been given in Equations (6.11) and (6.12). Simulations are conducted to test the proposed method for the lateral beam tracking system. The simulation results are shown in Figure 6.11. It is assumed that the aircraft offset angle ($\lambda$) is 1° and desired to be 0° before the aircraft starts the glideslope phase. For simplicity, it is also assumed that the station stays in the North direction; thus, $\psi_c$ becomes zero. The initial value of $\psi$ is also taken as zero. $\psi_c$ dynamically changes during the simulation until the constructed controller achieves to set $\lambda_e$ to zero. The yaw angle ($\psi$) follows this change, and it settles down to zero when $\lambda_e = 0$. As it is seen from Equation (6.1), the yaw angle only depends on the yaw rate. If the yaw angle is excited, the controller needs to produce the necessary input voltage for the actuator of the rudder to generate the yawing moment to compensate for the yaw rate. On the other hand, the deviation on $\psi_e$ also excites the bank angle $\phi$, and the controller produces necessary input voltage for the actuator of the aileron to generate the rolling moment to compensate the roll rate for setting the bank angle to zero. During this process, the control inputs are far below the limits. As a result, the aircraft settles down to the desired angle very smoothly and without steady-state error.

#### 6.4.2.2 Case 2:

The moderate turbulence model is added to the system as a disturbance, as shown in Figure 6.3. Matrix form of the generalized plant $P$ and $H_\infty$ optimal controller, which was constructed before, has been given in Equations (6.14) and (6.15). It is clearly seen from Figure 6.12 that the controller achieves to bring the aircraft 0° offset angle ($\lambda$) and keeps it around zero despite the moderate turbulence through the simulation.

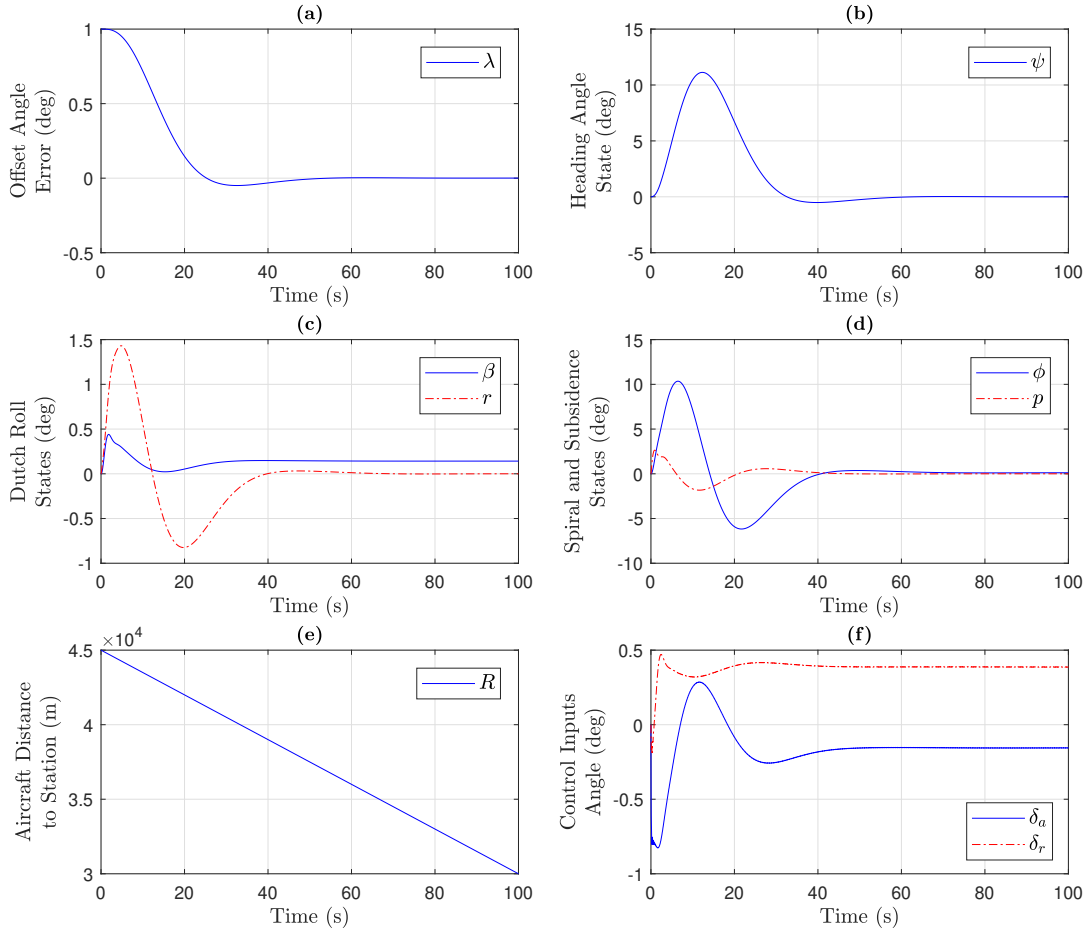


**Figure 6.11** Lateral beam guidance without disturbance (a) Offset angle error (b) Heading angle state (c) Dutch roll states (d) Spiral and subsidence states (e) Aircraft distance to the station (f) Control inputs

Although the turbulence directly affects the sideslip, the roll rate, and the yaw rate, and indirectly affects the yaw angle and aircraft offset angle, as seen in Equation (6.13), the controller generates the yawing and rolling moment by manipulating both the rudder and ailerons. The peak values of the states stay in very reasonable ranges.

### 6.4.3 Simulation Results for Aircraft Lateral Model Following Beam Control

#### 6.4.3.1 Case 1:

In this case, it is assumed that the external input $d_w$ in Figure 6.3 and 6.7 are zero. Our reference input $r_a$ in Figure 6.6 is the lateral deviation $d$ for this case. Matrix form of the generalized plant $P$ and $H_\infty$ optimal controller which was constructed and given in Equations (6.17) and (6.18) before. Simulations are conducted to test the $H_\infty$-based model following method for the lateral beam tracking system. The simulation results

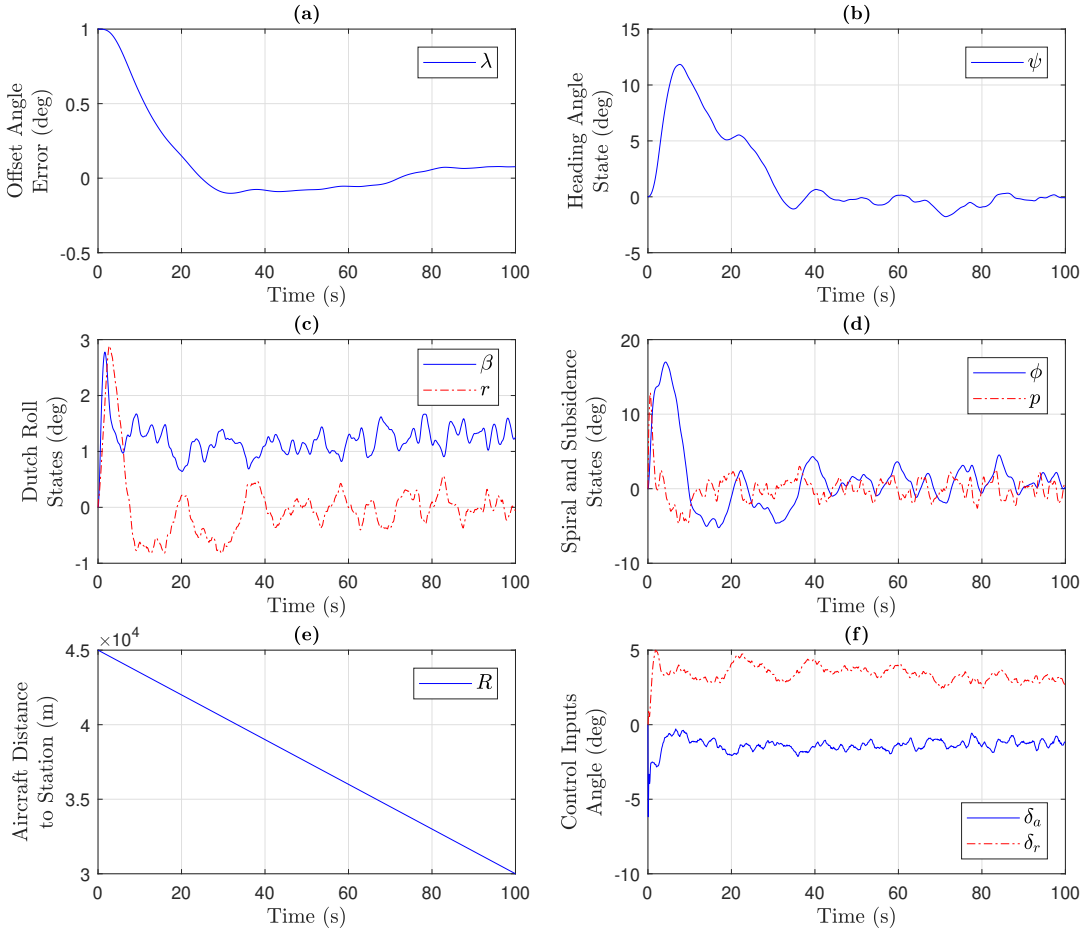


**Figure 6.12** Lateral beam guidance with moderate turbulence (a) Offset angle error (b) Heading angle state (c) Dutch roll states (d) Spiral and subsidence states (e) Aircraft distance to the station (f) Control inputs

are shown in Figure 6.13. It is assumed that the initial lateral distance of the aircraft off course $d$ is $500ft$. For simplicity, it is also assumed that the station stays in the North direction.

The purpose of this section is to generate a reference model for the lateral beam alignment phase and also make sure that the actual state follows the reference model well enough. As seen in Figure 6.13a, the actual path follows the reference path very closely. In order to do that, it is formed $\psi_c$ by using the lateral distance error $d_e$ in Figure 6.13b. Thus, once the yaw angle is excited, the controller produces the necessary input voltage for the actuator of the rudder to generate the yawing moment to compensate the yaw rate because the yaw angle only depends on the yaw rate. On the other hand, the deviation on $\psi_e$ also excites the bank angle $\phi$, and the controller produces necessary input voltage for the actuator of the aileron to generate the rolling

moment to compensate the roll rate for setting the bank angle to zero. During this process, the control inputs are far below the limits. As a result, the reference model is followed by the actual model very smoothly and without steady-state error.

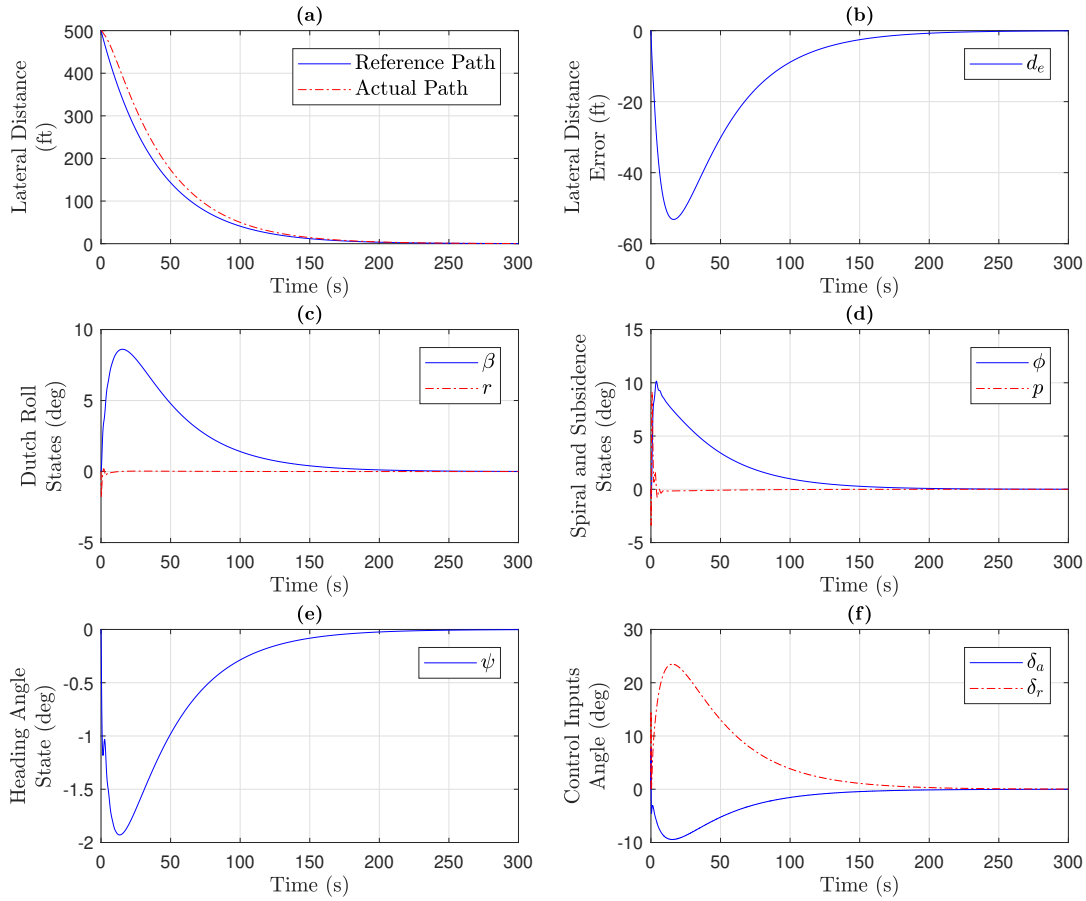


**Figure 6.13** Lateral model following beam guidance without disturbance (a) Reference path and actual path (b) Reference path - actual path (c) Dutch roll states (d) Spiral and subsidence states (e) Heading angle state (f) Control inputs

#### 6.4.3.2 Case 2:

Unlike Case 1 in this section, the moderate turbulence model is added to the system as an external disturbance input $d_w$. Matrix form of the generalized plant $P$ and $H_\infty$ optimal controller constructed before are given in Equations (6.19) and (6.20). The simulation results are given in Figure 6.14. The assumptions described in Case 1 are valid for this case. The initial lateral distance of the aircraft off course $d$ is $500ft$, and the station stays in the North direction.

Even under the moderate turbulence condition, according to Figure 6.14a, the actual model seems to be unaffected by the disturbance. That is because $\psi$ is integrated to

form the lateral deviation of $d$. The turbulence effect can be seen in $\psi$ in Figure 6.14e, but removed in 6.14a by the effect of the integral. On the other hand, the turbulence effect can be seen from the rest of the states, but they are handled successfully by the controller.

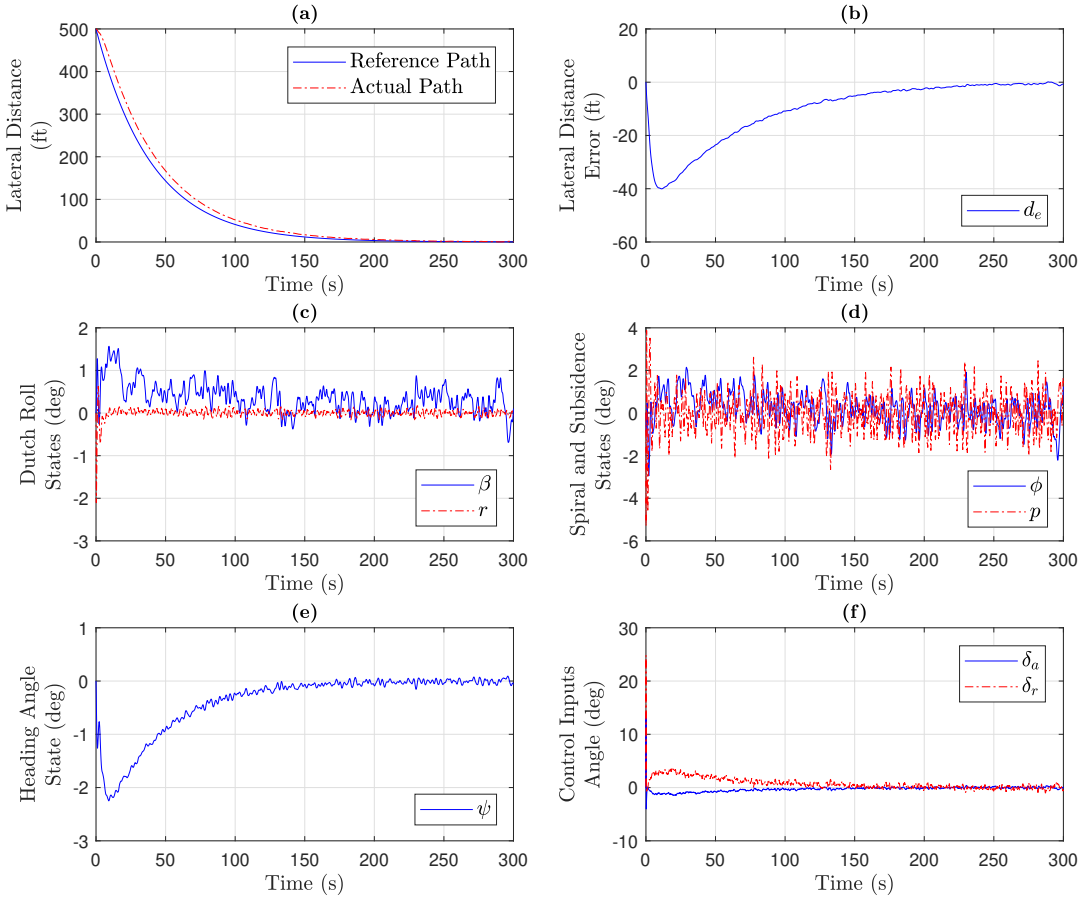


**Figure 6.14** Lateral model following beam guidance with moderate turbulence (a) Reference path and actual path (b) Reference path - actual path (c) Dutch roll states (d) Spiral and subsidence states (e) Heading angle state (f) Control inputs

## 6.5 Comparison with a Different Method

The proposed method in this paper will be compared with the two different studies in [61] and [96] to demonstrate the effectiveness of the proposed method. In the first comparison, the discussion goes over the general lateral control structure in Figure 6.1. There are two cases for the first comparison. The external disturbance is ignored in the first case. However, in the second case, it is assumed that the aircraft will encounter the moderate turbulence condition during the final approach phase. The method used in [61] is the LQR (Linear Quadratic Regulator) method.

In this section, the aircraft model will be different. The aircraft model given in [61] will be valid to make a comparison. Trim conditions are $V_T = 502\ ft/s$, $h = 0\ ft$, $\alpha = 0.03691\ rad$, $\theta = 0.03691\ rad$ and $X_{cg} = 0.35\bar{c}$. Then the linearized lateral motion of the system is expressed as follows:

$$A = \begin{bmatrix} -0.322 & 0.064 & 0.0364 & -0.9917 \\ 0 & 0 & 1 & 0.0037 \\ -30.6492 & 0 & -3.6784 & 0.6646 \\ 8.5396 & 0 & -0.0254 & -0.4764 \end{bmatrix} B = \begin{bmatrix} 0.0003 & 0.0008 \\ 0 & 0 \\ -0.7333 & 0.1315 \\ -0.0319 & -0.062 \end{bmatrix} \tag{6.23}$$

The same procedure in Section 6.3 is applied for this linearized aircraft model to find the general plant P and $H_\infty$ optimal feedback controller. The simulations are conducted to have the dutch roll states, spiral and subsidence states, and control inputs. Then the simulation results are given in Figure 6.15d, 6.15e, and 6.15f. The LQR method results are also generated to make the comparison more effectively and given in Figure 6.15a, 6.15b, and 6.15c. At first glance, it is clearly seen that all the states are well damped in the proposed method, and the peak values of all the states are less than the LQR method. The side sleep angle settles down to zero smoother, and the bank angle is almost not affected by the initial value of the $\beta$ in the proposed method. The control inputs also stay within their limits.

In the second case, it is assumed that the aircraft encounters the moderate turbulence condition described more detailed in Section 4.5. Then the linearized lateral motion of the system with exogenous input $d_w$ is expressed as follows:

$$A = \begin{bmatrix} -0.322 & 0.064 & 0.0364 & -0.9917 \\ 0 & 0 & 1 & 0.0037 \\ -30.6492 & 0 & -3.6784 & 0.6646 \\ 8.5396 & 0 & -0.0254 & -0.4764 \end{bmatrix} B = \begin{bmatrix} 0.0003 & 0.0008 & -0.322/502 \\ 0 & 0 & 0 \\ -0.7333 & 0.1315 & -30.6492/502 \\ -0.0319 & -0.062 & 8.5396/502 \end{bmatrix} \tag{6.24}$$

Then, the simulation results are given for both the LQR and $H_\infty$ methods in Figure 6.16. The responses are obtained similar to the one without disturbance. The peak values of all the states in the proposed method are less than the LQR method. The variations due to the turbulence also look smaller for all the states. As a result, the proposed method apparently provides well-damped and smoother responses.

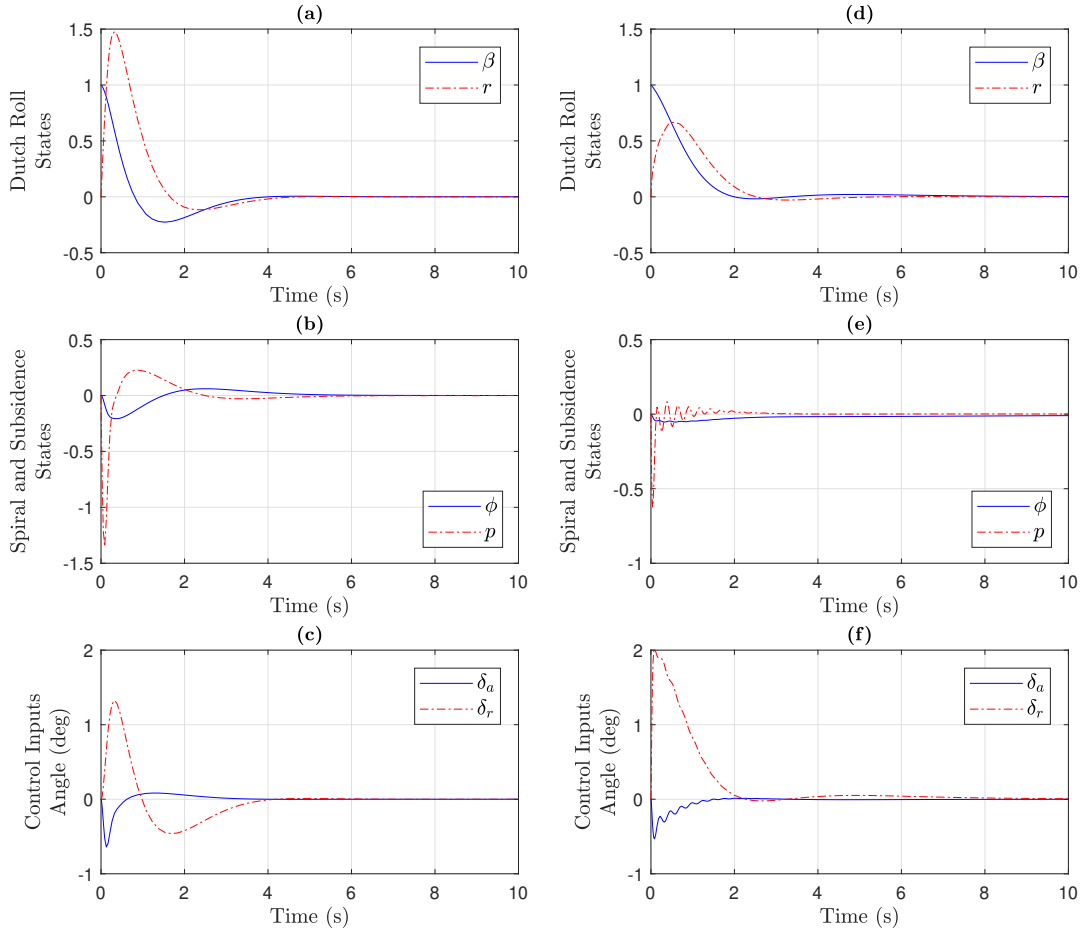


**Figure 6.15** Comparison of Lqr and $H_\infty$ methods without disturbance. For LQR method (a) Dutch roll states (b) Spiral and subsidence states (c) Control inputs; for $H_\infty$ method (d) Dutch roll states (e) Spiral and subsidence states (f) Control inputs

In the second comparison, the proposed method is compared with the study in [96], which the final approach phase is investigated. The LQR method is used to design a controller in this study. It is clearly seen that the lateral distance exhibits an overshoot at the beginning, then one more overshoot occurs when the crosswind starts. The bank angle and lateral deviation are also affected by these overshoots. On the other hand, as seen from the simulation results in Figure 6.13, there is no sign of overshoot. According to Figure 6.14, the proposed method in this paper eliminates any overshoot even under moderate turbulence conditions. The aircraft acts as the reference trajectory.

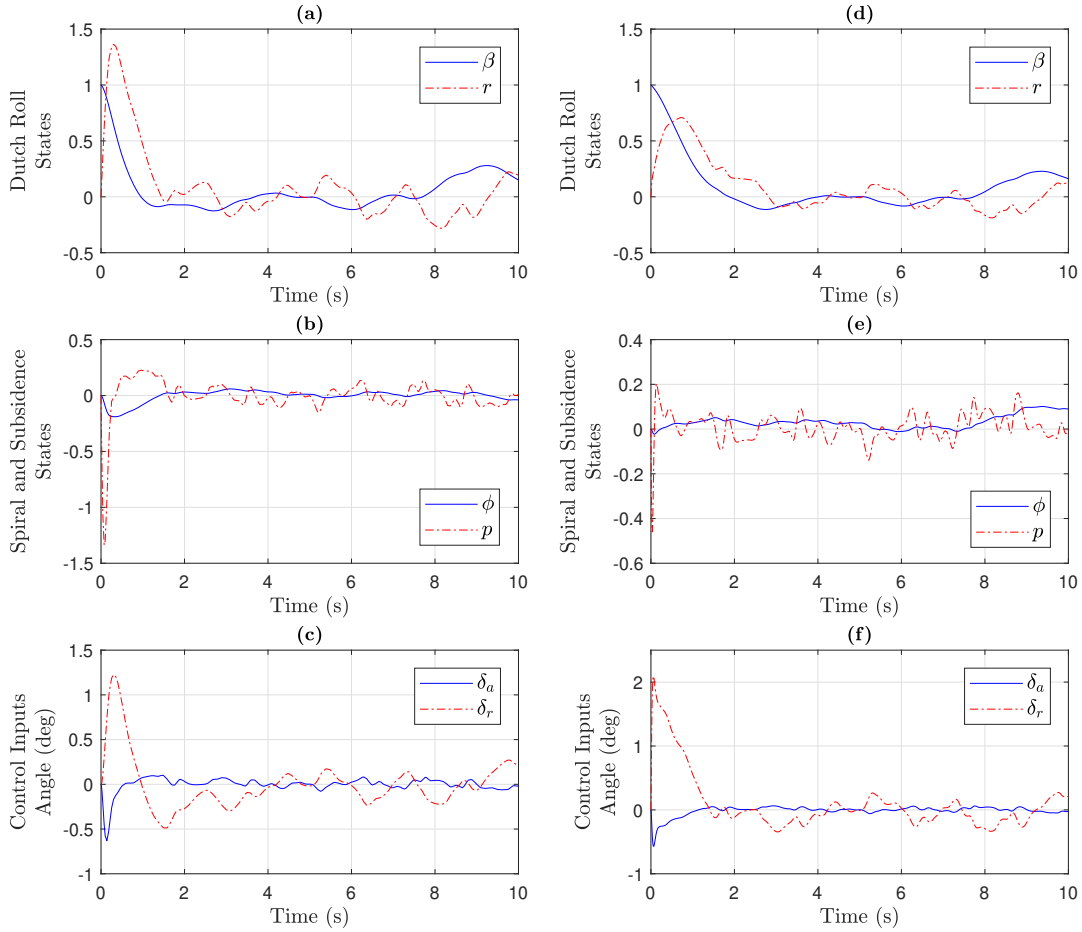


**Figure 6.16** Comparison of Lqr and $H_\infty$ methods with disturbance. For LQR method (a) Dutch roll states (b) Spiral and subsidence states (c) Control inputs; for $H_\infty$ method (d) Dutch roll states (e) Spiral and subsidence states (f) Control inputs

# 7
# RESULTS AND DISCUSSION

The reason why the automatic landing system came to the agenda was the understanding of the importance of safe landing after the fatal accidents that caused the death of many people. The conventional control methods are widely used in the automatic landing systems because of their simplicity and reliability. Researchers have started looking for new methods to overcome the optimization and performance issues of these conventional methods. Lots of different methods and topologies have been studied by researchers to find the best solution to have safer aircraft landings. These methods must deal with extreme conditions such as severe weather, low speed, and low altitude.

In this thesis, we propose a different approach to the aircraft landing control systems. Unlike the existing control methods on the flight systems, this approach exploits the combination of the model following method, P-K configuration, $H_\infty$ synthesis, and LMI solution techniques.

The model following method is very suitable for landing of the flight system because the landing maneuver of an aircraft is generally the same and can be represented mathematically. However, this mathematical model must be applicable in reality. In this thesis, an exponential decay function is used to represent the flare and final approach phases mathematically. The values of this function are selected as it has to be in real flight. The structure of the overall system is created such that the real state of the system follows the state of the reference model. One advantage of the proposed method is that the system without a controller component is represented as a single matrix P, and the overall system is formed as a P-K configuration. Therefore, this problem could be transformed into an $H_\infty$ optimal control problem. Briefly, the contributions of this study can be listed as follows:

- One of the most important advantages of the $H_\infty$ method over the conventional controllers is that it can be used in the multivariable system problems, which brings the weighting function to the game. Weighting functions have several

advantages for the proposed method. We can distinguish more important signals than less important signals by properly adjusting these functions. On the other hand, signals can be scaled easily by playing with them. The functions can also be formed in the frequency domain; thus, the scaling process can be done for certain frequencies. However, finding the right weighting function can sometimes be a time-consuming job.

- $H_\infty$ synthesis is a very advanced technique. It is also a disturbance attenuation problem that is mainly based on worst-case performance analysis. Thus, this method is one of the best solutions to deal with worst-case scenarios such as windshear, turbulence, etc. However, designers must solve very complex mathematical formulas. In order to do that, the mathematical model of the system must be known well enough because the synthesized controller will be optimal in the sense of formulation.

- $H_\infty$ and P-K configuration together provide the most compact control system structure where every kind of disturbances and uncertainties can be included in the system explicitly. Thus, any explicit changes do not bother the overall system, and they are implemented quickly.

- Synthesised controllers in this thesis are optimal controllers because the cost function is a performance criterion that is desired to be minimized and defined as an $H_\infty$ norm of the closed-loop transfer function. This cost function is solved by representing it as the $H_\infty$ norm constraints. Thus the synthesized controller is found by the iteration principle. Minimum gamma gives us the optimal solution.

- The model following method continuously tends to correct the error between the state of the reference model and the state of the real system. Thus, the model following method is preferred when there is uncertainty, such as windshear or disturbance, in the system. $H_\infty$ synthesis method also has a disturbance attenuation property, as described above. Our simulation results clearly show that the combination of the two methods provides very decent results as expected.

The simulations in this thesis are conducted for two cases. In the first case, no exogenous disturbance is considered. However, in the second case, light and severe weather conditions are taken into consideration. Simulation results are discussed in detail at the end of each chapter.

The flare phase is one of the most critical phases during landing. Most of the accidents occur in this phase, as discussed before. The simulation results without any

disturbance for the flare phase clearly indicate that the aircraft path and reference path are almost identical. In the second case, both moderate and severe windshear are separately taken into account as exogenous input. The aircraft resists very well to even the moderate windshear condition. The aircraft follows the reference model very closely, and a smooth touchdown is achieved. However, another method compared with the proposed method under the same conditions looks failed. In addition to the soft touchdown and very close follow-up of the reference path, the aircraft firmly lands to the calculated touchdown point. During this highly remarkable landing, all the states and actuator deflection angles are kept within the boundaries owing to the weighting functions.

Another subject in the scope of this thesis is the final approach phase, which is the first maneuver of the entire landing. The aircraft must align itself to the center of the runway before the glide-slope phase. A reference model that is very similar to the flare phase is also defined for this phase. The effect of the proposed method is discussed step by step throughout the chapter. The proposed method is firstly applied to the general lateral motion of the aircraft. Nevertheless, it is clearly seen that only the yaw damper feedback is not sufficient. Then, the problem is extended to cover the lateral beam guidance system, which is one of the vitally critical control problems of the automatic landing systems. Lastly, the model following method is embedded in the lateral beam structure. Various scenarios are studied and simulated. In the first scenario, it is studied on a simple linearized aircraft model. Then, the light and moderate turbulence are added separately to this system as exogenous disturbance inputs. The same procedure is applied for both the lateral beam guidance with and without model following method. According to the simulation results, the steady-state bank angle error for the spiral mode is corrected. On the other hand, the aircraft offset angle is controlled in the lateral beam guidance system. Then the lateral distance is controlled when the model following method is integrated into the system. Highly satisfying and exciting results are obtained from both different structures, as discussed in detail at the end of the Chapter 6. For example, the lateral distance of the aircraft off course $d$ almost becomes identical with the reference path even under moderate turbulence. At the same time, all the actuator deflections and the other aircraft states stay within the limits. In the end, the proposed method is compared with the different studies, and it is shown that the proposed method apparently provides well-damped, smoother, and safer responses.

In future work, it will be concentrated on the flare phase again. In this case, the robustness will be taken into account in terms of uncertainties. On the other hand, the lateral part of the windshear effect can also be taken into account for more realistic simulations.

# References


[1] P. Serra, R. Cunha, T. Hamel, C. Silvestre, and F. Le Bras, "Nonlinear image-based visual servo controller for the flare maneuver of fixed-wing aircraft using optical flow," *IEEE Transactions on Control Systems Technology*, vol. 23, no. 2, pp. 570–583, 2015.

[2] D. Seto, E. Ferreira, and T. F. Marz, "Case study: Development of a baseline controller for automatic landing of an f-16 aircraft using linear matrix inequalities (lmis)," CARNEGIE-MELLON UNIV PITTSBURGH PA SOFTWARE ENGINEERING INST, Tech. Rep., 2000.

[3] E. H. J. Pallett, "Automatic flight control," 1987.

[4] D. McLean, "Automatic flight control systems(book)," *Englewood Cliffs, NJ, Prentice Hall, 1990, 606*, 1990.

[5] D. Siegel and R. J. Hansman, "Development of an autoland system for general aviation aircraft," Tech. Rep., 2011.

[6] J. Che and D. Chen, "Automatic landing control using h/sub/spl infin//control and stable inversion," in *Proceedings of the 40th IEEE Conference on Decision and Control (Cat. No. 01CH37228)*, IEEE, vol. 1, 2001, pp. 241–246.

[7] F. A. Administration, *Airplane Flying Handbook (FAA-H-8083-3B)*. United States Department of Transportation, Federal Aviation Administration, Airman Testing Standards Branch, Oklahoma City, OK, 2016.

[8] D. Foyle, A. Goodman, and B. Hooey, "Nasa aviation safety program conference on human performance modeling of approach and landing with augmented displays," in *National Aeronautics and Space Administration*, 2003.

[9] Y. Ochi and K. Kanai, "Automatic approach and landing for propulsion controlled aircraft by h/sub/spl infin//control," in *Proceedings of the 1999 IEEE International Conference on Control Applications (Cat. No. 99CH36328)*, IEEE, vol. 2, 1999, pp. 997–1002.

[10] Y. Li, N. Sundararajan, P. Saratchandran, and Z. Wang, "Robust neuro-h/sub/spl infin//controller design for aircraft auto-landing," *IEEE Transactions on Aerospace and Electronic Systems*, vol. 40, no. 1, pp. 158–167, 2004.

[11] R. Lungu, M. Lungu, and L. T. Grigorie, "Automatic control of aircraft in longitudinal plane during landing," *IEEE Transactions on Aerospace and Electronic Systems*, vol. 49, no. 2, pp. 1338–1350, 2013.

[12] W. T. Miller, P. J. Werbos, and R. S. Sutton, *Neural networks for control*. MIT press, 1995.

[13] F. Le Bras, T. Hamel, R. Mahony, C. Barat, and J. Thadasack, "Approach maneuvers for autonomous landing using visual servo control," *IEEE Transactions on Aerospace and Electronic Systems*, vol. 50, no. 2, pp. 1051–1065, 2014.

[14] V. P. Galotti, *The Future Air Navigation System (FANS)*. 1997.

[15] Z. Zhen, S. Jiang, and K. Ma, "Automatic carrier landing control for unmanned aerial vehicles based on preview control and particle filtering," *Aerospace Science and Technology*, vol. 81, pp. 99–107, 2018.

[16] J. H. Blakelock, *Automatic control of aircraft and missiles*. John Wiley & Sons, 1991.

[17] K. Tamkaya, L. Ucun, and I. Ustoglu, "$H_\infty$-based model following method in autolanding systems," *Aerospace Science and Technology*, vol. 94, p. 105 379, 2019.

[18] M. B. Subrahmanyam, "H-infinity design of f/a-18a automatic carrier landing system," *Journal of guidance, control, and dynamics*, vol. 17, no. 1, pp. 187–191, 1994.

[19] L. Zhao, X. Yang, H. Gao, and P. Shi, "Automatic landing system design using multiobjective robust control," *Journal of Aerospace Engineering*, vol. 26, no. 3, pp. 603–617, 2013.

[20] S.-P. Shue and R. K. Agarwal, "Design of automatic landing systems using mixed h/h control," *Journal of Guidance, Control, and Dynamics*, vol. 22, no. 1, pp. 103–114, 1999.

[21] R. Lungu and M. Lungu, "Application of $h_2/h_\infty$ and dynamic inversion techniques to aircraft landing control," *Aerospace Science and Technology*, vol. 46, pp. 146–158, 2015.

[22] R. Niewoehner and I. I. Kaminer, "Design of an autoland controller for an f-14 aircraft using h-infinity synthesis," *Journal of guidance, control, and dynamics*, vol. 19, no. 3, pp. 656–663, 1996.

[23] F. Liao, J. L. Wang, E. K. Poh, and D. Li, "Fault-tolerant robust automatic landing control design," *Journal of guidance, control, and dynamics*, vol. 28, no. 5, pp. 854–871, 2005.

[24] K. Nho and R. K. Agarwal, "Automatic landing system design using fuzzy logic," *Journal of Guidance, Control, and Dynamics*, vol. 23, no. 2, pp. 298–304, 2000.

[25] J.-G. Juang and J.-Z. Chio, "Fuzzy modelling control for aircraft automatic landing system," *International Journal of Systems Science*, vol. 36, no. 2, pp. 77–87, 2005.

[26] A. Kato and Y. Inagaki, "Control law for automatic landing using fuzzy-logic control," *Transactions of the Japan Society for Aeronautical and Space Sciences*, vol. 50, no. 170, pp. 274–283, 2008.

[27] C. Ha, "Gain-scheduled directional guidance controller design using a genetic algorithm for automatic precision landing," *International Journal of Control, Automation and Systems*, vol. 8, no. 1, pp. 107–117, 2010.

[28] R. Lungu, M. Lungu, and L. T. Grigorie, "Alss with conventional and fuzzy controllers considering wind shear and gyro errors," *Journal of Aerospace Engineering*, vol. 26, no. 4, pp. 794–813, 2013.

[29] S. Tong and Y. Li, "Adaptive fuzzy output feedback control of mimo nonlinear systems with unknown dead-zone inputs," *IEEE Transactions on Fuzzy Systems*, vol. 21, no. 1, pp. 134–146, 2012.

[30] V. Kumar, K. Rana, and V. Gupta, "Real-time performance evaluation of a fuzzy pi+ fuzzy pd controller for liquid-level process," *International journal of intelligent control and systems*, vol. 13, no. 2, pp. 89–96, 2008.

[31] H.-J. Rong, N. Sundararajan, P. Saratchandran, and G.-B. Huang, "Adaptive fuzzy fault-tolerant controller for aircraft autolanding under failures," *IEEE Transactions on Aerospace and Electronic Systems*, vol. 43, no. 4, pp. 1586–1603, 2007.

[32] C. E. Lan and R. C. Chang, "Unsteady aerodynamic effects in landing operation of transport aircraft and controllability with fuzzy-logic dynamic inversion," *Aerospace Science and Technology*, vol. 78, pp. 354–363, 2018.

[33] J.-G. Juang and K.-C. Cheng, "Application of neural networks to disturbances encountered landing control," *IEEE Transactions on Intelligent Transportation Systems*, vol. 7, no. 4, pp. 582–588, 2006.

[34] J.-G. Juang, L.-H. Chien, and F. Lin, "Automatic landing control system design using adaptive neural network and its hardware realization," *IEEE Systems Journal*, vol. 5, no. 2, pp. 266–277, 2011.

[35] R. Mori and S. Suzuki, "Neural network modeling of lateral pilot landing control," *Journal of Aircraft*, vol. 46, no. 5, pp. 1721–1726, 2009.

[36] M. Niculescu, "Lateral track control law for aerosonde uav," in *39th Aerospace Sciences Meeting and Exhibit*, 2001, p. 16.

[37] A. Pashilkar, N. Sundararajan, and P. Saratchandran, "A fault-tolerant neural aided controller for aircraft auto-landing," *Aerospace Science and Technology*, vol. 10, no. 1, pp. 49–61, 2006.

[38] H. Izadi, M. Pakmehr, and N. Sadati, "Optimal neuro-controller in longitudinal auto-landing of a commercial jet transport," in *Proceedings of 2003 IEEE Conference on Control Applications, 2003. CCA 2003.*, IEEE, vol. 1, 2003, pp. 492–497.

[39] C. C. Jorgensen and C. Schley, "A neural network baseline problem for control of aircraft flare and touchdown," in *Neural networks for control*, 1990, pp. 403–425.

[40] B. M. Kim, J. T. Kim, B. S. Kim, and C. Ha, "Adaptive integrated guidance and control design for automatic landing of a fixed wing unmanned aerial vehicle," *Journal of Aerospace Engineering*, vol. 25, no. 4, pp. 490–500, 2012.

[41] H.-S. Ju and C.-C. Tsai, "Glidepath command generation and tracking for longitudinal autolanding," *IFAC Proceedings Volumes*, vol. 41, no. 2, pp. 1093–1098, 2008.

[42] Q. Xin and Z. Shi, "Robust adaptive backstepping controller design for aircraft autonomous short landing in the presence of uncertain aerodynamics," *Journal of Aerospace Engineering*, vol. 31, no. 2, p. 04 018 005, 2018.

[43] S. Singh and R. Padhi, "Automatic path planning and control design for autonomous landing of uavs using dynamic inversion," in *American Control Conference, 2009. ACC'09.*, IEEE, 2009, pp. 2409–2414.

[44] R. Lungu and M. Lungu, "Automatic landing control using h-inf control and dynamic inversion," *Proceedings of the Institution of Mechanical Engineers, Part G: Journal of Aerospace Engineering*, vol. 228, no. 14, pp. 2612–2626, 2014.

[45] H. Vo and S. Seshagiri, "Robust control of f-16 lateral dynamics," in *2008 34th Annual Conference of IEEE Industrial Electronics*, IEEE, 2008, pp. 343–348.

[46] D. V. Rao and T. H. Go, "Automatic landing system design using sliding mode control," *Aerospace Science and Technology*, vol. 32, no. 1, pp. 180–187, 2014.

[47] J.-G. Juang and S.-T. Yu, "Disturbance encountered landing system design based on sliding mode control with evolutionary computation and cerebellar model articulation controller," *Applied Mathematical Modelling*, vol. 39, no. 19, pp. 5862–5881, 2015.

[48] D. V. Rao and N. K. Sinha, "A sliding mode controller for aircraft simulated entry into spin," *Aerospace Science and Technology*, vol. 28, no. 1, pp. 154–163, 2013.

[49] J. Fei and H. Ding, "Adaptive sliding mode control of dynamic system using rbf neural network," *Nonlinear Dynamics*, vol. 70, no. 2, pp. 1563–1573, 2012.

[50] R. Akmeliawati and I. M. Mareels, "Nonlinear energy-based control method for aircraft automatic landing systems," *IEEE Transactions on Control Systems Technology*, vol. 18, no. 4, pp. 871–884, 2009.

[51] S.-F. Wu and S.-F. Guo, "Optimum flight trajectory guidance based on total energy control of aircraft," *Journal of guidance, control, and dynamics*, vol. 17, no. 2, pp. 291–296, 1994.

[52] T. Wagner and J. Valasek, "Digital autoland control laws using quantitative feedback theory and direct digital design," *Journal of Guidance, Control, and Dynamics*, vol. 30, no. 5, pp. 1399–1413, 2007.

[53] B. prasad B and S. Pradeep, "Automatic landing system design using feedback linearization method," in *AIAA infotech@ Aerospace 2007 conference and exhibit*, 2007, p. 2733.

[54] M. G. Cooper, "Genetic design of rule-based fuzzy controllers," 1994.

[55] J.-G. Juang, H.-K. Chiou, and L.-H. Chien, "Analysis and comparison of aircraft landing control using recurrent neural networks and genetic algorithms approaches," *Neurocomputing*, vol. 71, no. 16-18, pp. 3224–3238, 2008.

[56] M. Kaiser, N. Gans, and W. Dixon, "Vision-based estimation for guidance, navigation, and control of an aerial vehicle," *IEEE Transactions on aerospace and electronic systems*, vol. 46, no. 3, pp. 1064–1077, 2010.

[57] R. Mahony and T. Hamel, "Image-based visual servo control of aerial robotic systems using linear image features," *IEEE Transactions on Robotics*, vol. 21, no. 2, pp. 227–239, 2005.

[58] F. Le Bras, T. Hamel, C. Barat, and R. Mahony, "Nonlinear image-based visual servo controller for automatic landing guidance of a fixed-wing aircraft," in *2009 European Control Conference (ECC)*, IEEE, 2009, pp. 1836–1841.

[59] P. Serra, F. Le Bras, T. Hamel, C. Silvestre, and R. Cunha, "Nonlinear ibvs controller for the flare maneuver of fixed-wing aircraft using optical flow," in *49th IEEE Conference on Decision and Control (CDC)*, IEEE, 2010, pp. 1656–1661.

[60] Y. Meng, W. Wang, H. Han, and J. Ban, "A visual/inertial integrated landing guidance method for uav landing on the ship," *Aerospace Science and Technology*, vol. 85, pp. 474–480, 2019.

[61] B. L. Stevens, F. L. Lewis, and E. N. Johnson, *Aircraft control and simulation: dynamics, controls design, and autonomous systems*. John Wiley & Sons, 2015.

[62] X. Wang, E.-J. Van Kampen, Q. Chu, and P. Lu, "Stability analysis for incremental nonlinear dynamic inversion control," *Journal of Guidance, Control, and Dynamics*, vol. 42, no. 5, pp. 1116–1129, 2019.

[63] B. Etkin, *Dynamics of atmospheric flight*. Courier Corporation, 2012.

[64] H. R. Harrison, "Atmospheric and space flight dynamics: Modeling and simulation with matlab and simulink a. tewari birkhauser verlag, viaduktstrasse 42, ch-4051 basel, switzerland. 2007. 556pp.£ 60. isbn 978-0-8176-4437-6.," *The Aeronautical Journal*, vol. 112, no. 1136, pp. 621–621, 2008.

[65] Wikipedia contributors, *H-infinity methods in control theory — Wikipedia, the free encyclopedia*, `https://en.wikipedia.org/w/index.php?title=H-infinity_methods_in_control_theory&oldid=887521892`, [Online; accessed 10-April-2020], 2019.

[66] G. Zames, "Feedback and optimal sensitivity: Model reference transformations, multiplicative seminorms, and approximate inverses," *IEEE Transactions on automatic control*, vol. 26, no. 2, pp. 301–320, 1981.

[67] ——, "On the input-output stability of time-varying nonlinear feedback systems part one: Conditions derived using concepts of loop gain, conicity, and positivity," *IEEE transactions on automatic control*, vol. 11, no. 2, pp. 228–238, 1966.

[68] ——, "On the input-output stability of time-varying nonlinear feedback systems–part ii: Conditions involving circles in the frequency plane and sector nonlinearities," *IEEE Transactions on Automatic Control*, vol. 11, no. 3, pp. 465–476, 1966.

[69] J. C. Doyle, K. Glover, P. P. Khargonekar, and B. A. Francis, "State-space solutions to standard $h_2$ and $h_\infty$ control problems," *IEEE Transactions on Automatic control*, vol. 34, no. 8, pp. 831–847, 1989.

[70] P. Gahinet and P. Apkarian, "A linear matrix inequality approach to $h_\infty$ control," *International journal of robust and nonlinear control*, vol. 4, no. 4, pp. 421–448, 1994.

[71] P. Apkarian and D. Noll, "Nonsmooth $h_\infty$ synthesis," *IEEE Transactions on Automatic Control*, vol. 51, no. 1, pp. 71–86, 2006.

[72] H. Toivonen, "Lecture notes on robust control by state-space methods," *Available at: users. abo. fi/htoivone/courses/robust/hsem. pdf*, 1995.

[73] H. Werner, "Optimal and robust control," *Lecture Notes*, 2003.

[74] S. Skogestad and I. Postlethwaite, *Multivariable feedback control: analysis and design*. Wiley New York, 2007, vol. 2.

[75] Wikibooks, *Lmis in control/pages/hinf outputoptimalcontrol — wikibooks, the free textbook project*, [Online; accessed 7-April-2020], 2019. [Online]. Available: %5Curl%7Bhttps://en.wikibooks.org/w/index.php?title=LMIs_in_Control/pages/Hinf_OutputOptimalControl&oldid=3623217%7D.

[76] G. E. Dullerud and F. Paganini, *A course in robust control theory: a convex approach*. Springer Science & Business Media, 2013, vol. 36.

[77] K. Zhou, J. C. Doyle, K. Glover, *et al.*, *Robust and optimal control*. Prentice hall New Jersey, 1996, vol. 40.

[78] K. Zhou and J. C. Doyle, *Essentials of robust control*. Prentice hall Upper Saddle River, NJ, 1998, vol. 104.

[79] R. J. Caverly and J. R. Forbes, "Lmi properties and applications in systems, stability, and control theory," *arXiv preprint arXiv:1903.08599*, 2019.

[80] G. Alag, R. Kempel, J. Pahle, J. Bresina, and F. Bartoli, "Model-following control for an oblique-wing aircraft," in *Astrodynamics Conference*, 1986, p. 2244.

[81] G. NIELD and J. POWELL, "A model-following technique for insensitive aircraft control systems," in *7th Atmospheric Flight Mechanics Conference*, 1982, p. 1867.

[82] D. McLean, "Automatic flight control systems," *Measurement and Control*, vol. 36, no. 6, pp. 172–175, 2003.

[83] T. T. Fujita, "Spearhead echo and downburst near the approach end of a john f. kennedy airport runway, new york city," 1976.

[84] A. Miele, T. Wang, W. Melvin, and R. Bowles, "Gamma guidance schemes for flight in a windshear," *Journal of Guidance, Control, and Dynamics*, vol. 11, no. 4, pp. 320–327, 1988.

[85] A. Miele, T. Wang, and W. Melvin, "Optimization and acceleration guidance of flight trajectories in a windshear," *Journal of Guidance, Control, and Dynamics*, vol. 10, no. 4, pp. 368–377, 1987.

[86] A. Miele, T. Wang, W. Melvin, and R. Bowles, "Acceleration, gamma, and theta guidance for abort landing in a windshear," *Journal of Guidance, Control, and Dynamics*, vol. 12, no. 6, pp. 815–821, 1989.

[87] A. Miele, T. Wang, and W. Melvin, "Penetration landing guidance trajectories in the presence of windshear," *Journal of Guidance, Control, and Dynamics*, vol. 12, no. 6, pp. 806–814, 1989.

[88] A. Bryson JR, "Feedback control for penetrating a downburst," in *Guidance, Navigation and Control Conference*, 1987, p. 2343.

[89] Y. Zhao and A. Bryson, "Aircraft control in a downburst on takeoff and landing," in *Decision and Control, 1990., Proceedings of the 29th IEEE Conference on*, IEEE, 1990, pp. 753–757.

[90] ——, "Optimal paths through downbursts," *Journal of Guidance, Control, and Dynamics*, vol. 13, no. 5, pp. 813–818, 1990.

[91] ——, “Control of an aircraft in downbursts,” *Journal of Guidance, Control, and Dynamics*, vol. 13, no. 5, pp. 819–823, 1990.

[92] A. Woodfield and J. Woods, “Worldwide experience of wind shear during 1981-1982,” Royal Aircraft Establishment Bedford (England), Tech. Rep., 1983.

[93] Y. Zhao, “Optimal control of an aircraft flying through a downburst,” PhD thesis, Stanford University, 1989.

[94] C.-A. Brezoescu, “Small lightweight aircraft navigation in the presence of wind,” PhD thesis, Université de Technologie de Compiègne, 2013.

[95] P. Heidlauf, A. Collins, M. Bolender, and S. Bak, “Verification challenges in f-16 ground collision avoidance and other automated maneuvers.,” in *5th International Workshop on Applied Verification for Continuous and Hybrid Systems (ARCH 2018)*.

[96] H. Sadat-Hoseini, S. Fazelzadeh, A. Rasti, and P. Marzocca, “Final approach and flare control of a flexible aircraft in crosswind landings,” *Journal of Guidance, Control, and Dynamics*, vol. 36, no. 4, pp. 946–957, 2013.

# A
# $\mathscr{H}_\infty$ Optimal Controller Synthesis

The code below is written to be a generic code in Matlab. That is valid for all the simulations, that include the generalized plant P, throughout this thesis. Only, the initial value of gamma may be different for each simulation. "Plant_P" is a .slx file created in Simulink. The block representations of all these .slx files are given in the related sections. "Plant_P.slx" file and the file having the code below must be in the same location.

**Listing A.1** $H_\infty$ optimal controller synthesising code written in MATLAB

```
clear all;
[A,B,C,D]=linmod('Plant_P')
P=ss(A,B,C,D)
P=minreal(P)
%%-------------------------------------------------------------
% Generalized Plant P given as block diagrams in the thesis ...
    are called "Plant_P".
% "Plant_P" is matlab .slx file.
% "Plant_P" must be located at the same location as this code.
% Input "u" is cosidered as one input as multiplexer used. ...
    Rest of the
% inputs are considered separetely.
% Output "y" is cosidered as one output as multiplexer used.
% Output "z" is cosidered seperately.

% Total Input Number=
NumInp=size(Simulink.MDLInfo('Plant_P').Interface.Inports,1);
NumDistInp=NumInp-1;% One input is for "u". Rest of the ...
    inputs are for "w".

% Total Output Number =
NumOut=size(Simulink.MDLInfo('Plant_P').Interface.Outports,1);
NumPerfOut=NumOut-1;% One output is for "y". Rest of the ...
    outputs are for "z".

% Control Input Number=
NumContInp=1;
%%-------------------------------------------------------------
% Partitioning the Generalized Plant P Matrix
A=P.A
B1=P.B(:,NumContInp)
B2=P.B(:,NumContInp+1:NumDistInp+1)
C1=P.C(1:NumPerfOut,:)
```

```
C2=P.C(NumPerfOut+1:size(C,1),:)
D11=P.D(1:NumPerfOut,NumContInp)
D12=P.D(1:NumPerfOut,NumContInp+1:NumDistInp+1)
D21=P.D(NumPerfOut+1:size(D,1),NumContInp)
D22=P.D(NumPerfOut+1:size(D,1),2:NumDistInp+1)
%%-------------------------------------------------------------
nR_A=size(A,1)       % Row number of A
nC_A=size(A,2)       % Column number of A
nR_B1=size(B1,1)     % Row number of B1
nC_B1=size(B1,2)     % Column number of B1
nR_B2=size(B2,1)     % Row number of B2
nC_B2=size(B2,2)     % Column number of B2
nR_C1=size(C1,1)     % Row number of C1
nC_C1=size(C1,2)     % Column number of C1
nR_C2=size(C2,1)     % Row number of C2
nC_C2=size(C2,2)     % Column number of C2
nR_D12=size(D12,1)   % Row number of D12
nC_D12=size(D12,2)   % Column number of D12
nR_D21=size(D21,1)   % Row number of D21
nC_D21=size(D21,2)   % Column number of D21
%%-------------------------------------------------------------
yalmip('clear');
Y=sdpvar(nC_A,nR_A,'symmetric')
X=sdpvar(nR_A,nC_A,'symmetric')
An=sdpvar(nR_A,nC_A,'full')
Bn=sdpvar(nR_A,nR_C2,'full')
Cn=sdpvar(nC_B2,nC_A,'full')
Dn=sdpvar(nC_B2,nR_C2,'full')
%%-------------------------------------------------------------
gamma = 2.5;
stepval = 0.01;
while true
    lmi1=[A*Y+Y*A'+B2*Cn+Cn'*B2'     (A'+An+(B2*Dn*C2)')'      ...
       B1+B2*Dn*D21              (C1*Y+D12*Cn)';
          A'+An+(B2*Dn*C2)'           X*A+A'*X+Bn*C2+C2'*Bn'   ...
             X*B1+Bn*D21               (C1+D12*Dn*C2)';
          (B1+B2*Dn*D21)'             (X*B1+Bn*D21)'           ...
             -gamma*eye(size(D11,2)) (D11+D12*Dn*D21)';
          C1*Y+D12*Cn                 C1+D12*Dn*C2             ...
             D11+D12*Dn*D21           -gamma*eye(size(D11,1))]

    lmi2=[X eye(size(X,1),size(Y,2)); ...
       eye(size(Y,1),size(X,2)) Y]

    lmi=[lmi1<0,lmi2>0]

    options=sdpsettings('solver','sedumi')
    solvesdp(lmi, [], options)
    eigs=eig(double(lmi1))
    max_eig = max(eig(double(lmi1)))
    if max_eig < 0
        gamma = gamma - stepval;
    else
        gamma = gamma + stepval

        lmi1=[A*Y+Y*A'+B2*Cn+Cn'*B2'     (A'+An+(B2*Dn*C2)')' ...
              B1+B2*Dn*D21              (C1*Y+D12*Cn)';
```

```
81                A'+An+(B2*Dn*C2)'           ...
                     X*A+A'*X+Bn*C2+C2'*Bn'  X*B1+Bn*D21 ...
                                  (C1+D12*Dn*C2)';
82                (B1+B2*Dn*D21)'           (X*B1+Bn*D21)' ...
                              -gamma*eye(size(D11,2))  ...
                     (D11+D12*Dn*D21)';
83                C1*Y+D12*Cn                C1+D12*Dn*C2 ...
                               D11+D12*Dn*D21          ...
                     -gamma*eye(size(D11,1))]
84
85          lmi2=[X eye(size(X,1),size(Y,2)); ...
               eye(size(Y,1),size(X,2)) Y]
86
87          lmi=[lmi1<0,lmi2>0]
88
89          solvesdp(lmi, [], options)
90          break;
91      end
92  end
93  %%-----------------------------------------------------------
94  Xopt=double(X)
95  Yopt=double(Y)
96  An=double(An)
97  Bn=double(Bn)
98  Cn=double(Cn)
99  Dn=double(Dn)
100 eigs=eig(double(lmi1))
101 gamma= gamma
102 %%-----------------------------------------------------------
103 Y2=eye(size(Xopt,1),size(Yopt,2));
104 X2=eye(size(Xopt,1),size(Yopt,2))-Xopt*Yopt
105 PK_cl=inv([X2 Xopt*B2;zeros(size(Cn,1),size(X2,2)) ...
       eye(size(Dn,1),size(B2,2))])*...
106      [[An Bn;Cn Dn]-[Xopt*A*Yopt ...
            zeros(size(Xopt,1),size(Bn,2)); ...
            zeros(size(Cn,1),size(Yopt,2)) ...
            eye(size(Dn,1),size(Bn,2))]]...
107      *inv([Y2' zeros(size(Y2,2),size(Bn,2));C2*Yopt ...
            eye(size(C2,1),size(Dn,2))])
108 Ak2= PK_cl(1:size(An,1),1:size(An,2))
109 Bk2= PK_cl(1:size(Bn,1),size(An,2)+1:size(PK_cl,2))
110 Ck2= PK_cl(size(An,1)+1:size(PK_cl,1),1:size(Cn,2))
111 Dk2= PK_cl(size(Bn,1)+1:size(PK_cl,1),size(An,2)+1:size(PK_cl,2))
112 %%-----------------------------------------------------------
113 % Optimal Controller Synthesized
114 Dc=inv(eye(size(Dk2,1),size(D22,2))+Dk2*D22)*Dk2
115 Bc=Bk2*(eye(size(D22,1),size(Dc,2))-D22*Dc)
116 Cc=(eye(size(Dc,1),size(D22,2))-Dc*D22)*Ck2
117 Ac=Ak2-Bc*inv(eye(size(D22,1),size(Dc,2))-D22*Dc)*D22*Cc
```

# B
# Transport Aircraft

The code snippets below are used to linearize the dynamic equations of a transport aircraft. These code snippets are included in Stevens's book [61] and are taken from this book. On the other hand, some extra lines and features have been added due to the requirements of this thesis.

**Listing B.1** Trim values for transport aircraft

```
clear all
global x_s u_s gam
x_s(1)=input('Enter Vt : ');
x_s(5)= input('Enter h : ');
gam=input('Enter Gamma (deg.) : ')/57.29578;
name= input('Cost function file name? : ','s');
cg= 0.25; land=1;   % 0=clean 1=gear+flaps
u_s=[0.1 -10 cg land];
x_s(2)=.1;             % Alpha, initial guess
x_s(3)=x_s(2) +gam;    % Theta
x_s(4)=0;              % Pitch rate
x_s(6)=0;
s0=[u_s(1) u_s(2) x_s(2)];
% Initialization of other states and get initial cost
disp(['Initial cost = ',num2str( feval(name,s0) ) ])
[s,fval]=fminsearch(name,s0) ;
x_s(2)=s(3); x_s(3)=s(3)+gam;
u_s(1)=s(1); u_s(2)=s(2) ;
disp(['minimum cost = ',num2str(fval)])
disp(['minimizing vector= ',num2str(s)])
temp=[length(x_s),length(u_s),x_s,u_s];
name= input('Output file name? : ','s') ;
dlmwrite(name,temp);
```

**Listing B.2** Cost function

```
% Cost Function for 3-DOF Aircraft
function [f]=cost(s)
global x_s u_s gam
u_s(1)= s(1);
u_s(2)= s(2);
x_s(2)= s(3);
x_s(3)= x_s(2)+ gam; %theta
time= 0.0;
[xd]=transp(time,x_s,u_s);
f= xd(1)^2 + 100*xd(2)^2 + 10*xd(4)^2;
```

**Listing B.3** Longitudinal dynamics of transport aircraft

```
function [xd]= transp(time,x_s,u_s)
% Longitudinal dynamics of medium-sized transport aircraft
S=2170.0; CBAR=17.5; MASS=5.0E3; IYY= 4.1E6;
TSTAT=6.0E4; DTDV =-38.0; ZE = 2.0; CDCLS= .042;
CLA = .085; CMA =-.022; CMDE =-.016;     % per degree
CMQ =-16.0; CMADOT= -6.0; CLADOT= 0.0;   % per radian
RTOD = 57.29578; GD=32.17;
THTL =u_s(1);
ELEV =u_s(2);
XCG = u_s(3);
LAND = u_s(4);
VT = x_s(1);            % TAS in fps
ALPHA= RTOD*x_s(2);     % A.O.A.
THETA= x_s(3);          % PITCH ATTITUDE
Q = x_s(4);             % PITCH RATE
H = x_s(5);             % ALTITUDE
[MACH,QBAR]= ADC(VT,H);
QS = QBAR*S;
SALP= sin (x_s(2)); CALP= cos(x_s(2));
GAM = THETA - x_s(2); SGAM= sin (GAM); CGAM= cos(GAM);
if LAND == 0          % CLEAN
    CLO= .20; CDO= .016;
    CM0= .05; DCDG= 0.0; DCMG= 0.0;
elseif LAND == 1      % LANDING FLAPS & GEAR
    CLO= 1.0; CDO= .08;
    CMO= -.20; DCDG= .02; DCMG= -.05;
else
    disp('Landing Gear & Flaps ?')
end
P=31454;
THR= (TSTAT+VT*DTDV) * max(THTL,0);              % THRUST
CL=CLO+CLA*ALPHA;                                % NONDIM. LIFT
CM=DCMG+CMO+CMA*ALPHA+CMDE*ELEV+CL* (XCG-.25);   % MOMENT
CD=DCDG+CDO+CDCLS*CL*CL;                         % DRAG POLAR
%
% STATE EQUATIONS
xd(1) = (THR*CALP-QS*CD)/MASS - GD*SGAM;     % Vt_dot
xd(2)=(-THR*SALP-QS*CL+MASS*(VT*Q+GD*CGAM))...
        /(MASS*VT+QS*CLADOT);                % alpha_dot
xd(3) = Q;                                   %theta_dat
D = .5*CBAR*(CMQ*Q+CMADOT*xd(2))/VT;         % PITCH DAMPING
xd(4) = (QS*CBAR*(CM + D) + THR*ZE)/IYY;     % Q-DOT
xd(5) = VT*SGAM; % ALTITUTE RATE, VERTICAL VELOCITY, RATE OF ...
```

```
    CLIMB/DESCENT
xd(6) = VT*CGAM;
```

**Listing B.4** Air data computer function

```
function [AMACH,QBAR]=ADC(VT,ALT) %air data computer
R0 = 2.377E-3; % sea-level density
TFAC = 1.0 - 0.703E-5 * ALT;
T = 519.0 * TFAC; % temperature
if ALT ≥ 35000.0
    T= 390.0;
end
RHO = R0 * (TFAC^4.14); % density
AMACH= VT/sqrt(1.4*1716.3*T); % Mach number
QBAR = 0.5*RHO*VT*VT; % dynamic pressure
```

**Listing B.5** Linearization of transport aircraft using trim values

```
clear all
s_name = input('Enter Name of State Eq. File : ','s'); % ...
    enter "transp"
t_name= input('Enter Name of Trim File : ','s');
tmp= dlmread(t_name,',');
n=tmp(1); m=tmp(2); x_s=tmp(3:n+2);
u_s=tmp(n+3:m+n+2); tol=1e-6; time=0.;
n_c= input('Number of control inputs to be used ? : ');
%%-------------------------------------------------------------
% ----------------Matrix A---------------------
dx_s=0.1*x_s;
for i=1:n   % Set Perturbations
    if dx_s(i)==0.0;
        dx_s(i)=0.1;
    end
end
prev_a=zeros(n,1); a=zeros(n,n);
for j=1:n
     xt=x_s;
    for i=1:10
        xt(j)=x_s(j)+dx_s(j);
        xd1= feval (s_name,time,xt,u_s);
        xt(j)=x_s(j)-dx_s(j);
        xd2= feval (s_name,time,xt,u_s);
        a(:,j)= (xd1-xd2)'/(2*dx_s(j));
        if max( abs(a(:,j)-prev_a)./abs( a(:,j) + 1e-12 ) )<tol;
            break
        end
        dx_s(j)= 0.5*dx_s(j);
        prev_a = a(:,j);
    end
    iter_num=i;
    if iter_num==10
        disp('not converged on A, column',num2str(j))
    end
end
dlmwrite('A.dat',a);
% ----------------Matrix B---------------------
```

```
du_s=0.1*u_s;
for i=1:m-n_c    % Set Perturbations
    if du_s(i)==0.0;
        du_s(i)=0.1;
    end
end
prev_b=zeros(n,1); b=zeros(n,n_c);
for j=1:n_c
    ut=u_s;
    for i=1:10
        ut(j)=u_s(j)+du_s(j);
        xd1= feval (s_name,time,x_s,ut);
        ut(j)=u_s(j)-du_s(j);
        xd2= feval (s_name,time,x_s,ut);
        b(:,j)= (xd1-xd2)'/(2*du_s(j));
        if max( abs(b(:,j)-prev_b)./abs( b(:,j) + 1e-12 ) )<tol;
            break
        end
        du_s(j)= 0.5*du_s(j);
        prev_b = b(:,j);
    end
    iter_num=i;
    if iter_num==10
        disp('not converged on B, column',num2str(j))
    end
end
dlmwrite('B.dat',b);
%%-------------------------------------------------------------
% ----------------Matrix Bw---------------------
xw=[x(1:2) 0 0 0 0];
dxw=0.1*xw;
for i=1:2   % Set Perturbations
    if dxw(i)==0.0;
        dxw(i)=0.1;
    end
end
prev_bw=zeros(n,1); bw=zeros(n,2);
for j=1:2
    xwt=xw;
    for i=1:10
        xwt(j)=xw(j)+dxw(j);
        xd1= feval (s_name,time,xwt,u_s);
        xwt(j)=xw(j)-dxw(j);
        xd2= feval (s_name,time,xwt,u_s);
        bw(:,j)= (xd1-xd2)'/(2*dxw(j));
        if max( abs(bw(:,j)-prev_bw)./abs( bw(:,j) + 1e-12 ) ...
            )<tol;
            break
        end
        dxw(j)= 0.5*dxw(j);
        prev_bw = bw(:,j);
    end
    iter_num=i;
    if iter_num==10
        disp('not converged on Bw, column',num2str(j))
    end
end
dlmwrite('Bw.dat',bw);
```

# Publications From the Thesis

**Contact Information:** tamkaya@gmail.com

## Papers

1. K. Tamkaya, L. Ucun, and I. Ustoglu, "H-based model following method in autolanding systems," *Aerospace Science and Technology*, vol. 94, p. 105379, 2019.